GEOMATICS
ENGINEERING

UCGE Reports
Number 20383

Department of Geomatics Engineering

Ionospheric Imaging for Canadian Polar Regions

(URL: http://www.geomatics.ucalgary.ca/graduatetheses)

by

Ossama Jamil Saleh Al-Fanek

August, 2013

SCHULICH
School of Engineering
UNIVERSITY OF
CALGARY

UNIVERSITY OF CALGARY

Ionospheric Imaging for Canadian Polar Regions

by

Ossama Jamil Saleh Al-Fanek

A THESIS
SUBMITTED TO THE FACULTY OF GRADUATE STUDIES
IN PARTIAL FULFILMENT OF THE REQUIREMENTS FOR THE
DEGREE OF DOCTOR OF PHILOSOPHY

DEPARTMENT OF GEOMATICS ENGINEERING
CALGARY, ALBERTA
August, 2013

Abstract

Global Navigation Satellite Systems (GNSS) can be exploited as a cost-effective tool to remotely sense the Earth's ionosphere and investigate its characteristics. This is due to the global coverage and dual frequency data availability offered through worldwide networks of GNSS stations. Since the ionosphere is a dispersive medium, the dual frequency data can be utilized to derive highly accurate Slant Total Electron Content (STEC) measurements. STEC is defined as the integration of the free electron distribution in a 1-m^2 column along the signal path from the satellite to the receiver. Although STEC provides a valuable source of information about the ionosphere, these measurements do not contain any spatial information about the electron density distribution along the line-of-sight. Therefore, a tomographic technique is required to retrieve such three-dimensional information.

Measurement of the polar ionosphere is challenging due to its variable nature and typically limited availability of ground (or space) based infrastructure for remote sensing. An opportunity exists to exploit GNSS observations for ionospheric imaging in this region. Ten GNSS reference stations of the Canadian High Arctic Ionospheric Network (CHAIN), augmented with six International GNSS Service (IGS) polar reference stations, provides sufficient observations for GNSS-based tomographic estimation of key polar ionospheric parameters. Polar implementation of tomographic imaging for such a sparse network presents major challenges, however, and requires novel methods.

In this thesis, a novel Computerized Ionospheric Tomographic (CIT) reconstruction technique is developed to estimate electron density profiles over the Canadian polar region. This technique divides the ionosphere into voxels where the electron density is assumed to be homogeneous within a voxel. A functional based model is used to represent the electron density in space. The functional based model uses Empirical Orthogonal Functions (EOF) and Spherical Cap Harmonics (SCH) to describe the vertical and horizontal distribution of the electron density, respectively. Simulated and real data are used to demonstrate the feasibility and performance of the technique under different ionospheric conditions. The main aspects of the reconstruction results over the Canadian polar cap are highlighted and discussed and a clear understanding of the quality and limitations of the technique is achieved.

Preface

The Computerized Ionospheric Technique (CIT) described in Chapter 4 has been previously published in a conference paper:

- Al-Fanek, O. and Skone, S. (2011), “Ionospheric Imaging Using GNSS: A New Approach for Canadian Polar Regions”, Presented at the Proceedings of ION GNSS 2011, September 20–23, Portland, OR, pp. 643-653.

The author’s research work from the paper has been extended in this thesis.

Acknowledgements

First and Foremost, I wish to express my deepest gratitude to my advisor Dr. Susan Skone for the continuous support, for her patience, time and immense knowledge. I would never have been able to finish my dissertation without your excellent guidance and technical advice.

I would like to thank the UCAR/COSMIC program and the Canadian High Arctic Ionospheric Network (CHAIN) for providing the on-line access to COSMIC Radio Occultation (RO) and GPS data, respectively. Infrastructure funding for CHAIN is provided by the Canada Foundation for Innovation and the New Brunswick Innovation Foundation. CHAIN operation is conducted in collaboration with the Canadian Space Agency. I would also like to acknowledge the use of the IRI model which was kindly made available online.

Special thanks are extended to my friends, Oday Haddad, Mohannad Al-Durgham, Eunju Kwak, Qais Marji, Samer Chomery, Dima Oweis, Violin Narooz, Philip Nour, and Victor Halim for all your support. You are the best! A special appreciation is reserved to my friend Kaleel Al-Durgham. Your encouraging words and support will never be forgotten.

My sincere thanks and gratitude goes to my parents, brothers and sister for the love and support they have provided me over the years.

Finally, I would like to thank my wife, Ghena Azar. You have always had faith in me and stood by me through the good and bad times. You have been my inspiration and motivation for success. This thesis is dedicated to you.

Dedication

To my wife

Table of Contents

List of Tables

List of Figures

List of Abbreviations

Symbol	**Definition**
AFB	Air Force Base
ART	Algebraic Reconstruction Technique
C/A code	Coarse/Acquisition code
CADI	Canadian Advanced Digital Ionosondes
CDAAC	COSMIC Data Analysis and Archive Center
CHAIN	Canadian High Arctic Ionospheric Network
CIT	Computerized Ionospheric Tomography
CL code	Civilian Long length code
CM code	Civilian Moderate code
COSMIC	Constellation Observing System for the Meteorology, Ionosphere and Climate
COSPAR	Committee on Space Research
DGPS	Differential GPS
DoD	Department of Defense
DOP	Dilution of Precision
Dst	Disturbed Storm Time
EDOP	Easting Dilution of Precision
EGNOS	European Geostationary Navigation Overlay Service
EOF	Empirical Orthogonal Functions
ESA	European Space Agency
EUV	Extreme Ultra Violet
FAA	Federal Aviation Administration
GNSS	Global Navigation Satellite System
GPS	Global Positioning System
GSVD	Generalized Singular Value Decomposition
GTIM	Global Theoretical Ionospheric Model
HDOP	Horizontal Dilution of Precision
HF	High Frequency
IFB	Inter-Frequency Bias
IGS	International GNSS Service
IMF	Interplanetary Magnetic Field
IRI	International Reference Ionosphere
ISIS	International Satellites for Ionospheric Studies
JPL	Jet Propulsion Laboratory
LADGPS	Local-Area Differential GPS
LEO	Low-Earth Orbiting
LOS	Line-of-Sight
LT	Local Time
LUF	Lowest Usable Frequency
MAE	Mean Absolute Error

MART	Multiplicative Algebraic Reconstruction Technique
MCS	Master Control Station
MUF	Maximum Usable Frequency
NDOP	Northing Dilution of Precision
NNSS	Navy Navigation Satellite System
OCXO	Oven Controlled Crystal Oscillator
P-code	Precise code
PDOP	Position Dilution of Precision
PIM	Parameterized Ionospheric Model
ppm	Parts per million
PRN	Pseudo Random Noise
RMS	Root Mean Square
RO	Radio Occultation
SA	Selective Availability
SCH	Spherical Cap Harmonics
SCHA	Spherical Cap Harmonic Analysis
SED	Storm Enhanced Density
SHA	Spherical Harmonics Analysis
SIRT	Simultaneous Iterative Reconstruction Technique
SSN	Sunspot Number
STEC	Slant Total Electron Content
SVD	Singular Value Decomposition
TCXO	Temperature Compensated Crystal Oscillator
TDIM	Time Dependent Ionospheric Model
TDOP	Time Dilution of Precision
TEC	Total Electron Content
URSI	International Union of Radio Science
UT	Universal Time
VDOP	Vertical Dilution of Precision
WAAS	Wide Area Augmentation System
WADGPS	Wide-Area Differential GPS
WGS-84	World Geodetic System 1984

Chapter One: Introduction

This chapter presents the research background, research motivation and objectives.

1.1 Background and Motivation

The ionosphere is the ionized part of the upper region of the atmosphere extending from 60 km to 1500 km above the Earth's surface, where free electrons are produced during the interaction of Extreme Ultra Violet (EUV) and X-ray radiation with the upper neutral atmosphere. Knowledge of the ionospheric electron density distribution is important for scientific studies and practical applications. From the applications perspective, the electron density is the most important ionospheric parameter due to its effect on radio frequency electromagnetic wave propagation. For scientific studies, measuring ionospheric parameters, especially the electron density, helps to understand the solar-terrestrial interaction and provide more information about the spatial variations in ionospheric plasma and its evolution in time (Bust and Mitchell, 2008).

Global Navigation Satellite Systems (GNSS), such as the Global Positioning System (GPS), are regarded as important cost effective tools to remotely sense the Earth's ionosphere and investigate its characteristics. This is due to the global system coverage and multiple frequency data available via a world-wide network of GNSS stations. Since the ionosphere is a dispersive medium, this multiple frequency data can be used to derive the integrated measurements of electron density, known as Total Electron Content (TEC), along the line-of sight between a given satellite and receiver. By collecting TEC measurements from network of dual frequency GNSS receivers, useful information about the ionosphere can be derived and ionospheric models can be developed.

Ionospheric models usually represent average conditions and are mostly based on the bottom side of the ionosphere (i.e. the region below the maximum electron density which generally occurs in the range of 250-400 km altitude). A commonly used model is the grid model where the area being modeled is represented by fixed grid points in latitude and longitude. In this model, TEC values are mapped to a single ionospheric shell at fixed altitude where the maximum electron density is assumed to occur (normally a value in the range 250-400 km). Examples of such models are the polynomial function model (Komjathy, 1997) and spherical harmonics analysis (Schaer, 1999). A common hypothesis of these models is that they are constructed based on the assumption that the entire electron content in the ionosphere is concentrated in a single thin shell at a selected height above Earth. This assumption is not necessarily in agreement with real electron density distributions but is an approximation of reality as the ionosphere is a highly variable medium both temporally and spatially. Because of this limitation, all the ionospheric delays are mapped to that single spherical shell which means that all such models are two-dimensional (2-D). Thus the vertical distribution of electron density cannot be represented accurately at all times and locations by a thin shell which could result in modeling errors.

TEC provides a valuable source of information about the ionosphere. However, these measurements do not contain any spatial information about the electron density distribution along the line-of-sight. Therefore, a tomographic technique is required to retrieve such three-dimensional information. Ionospheric tomography is the problem of reconstructing the electron density distribution from a set of TEC measurements. This technique has the advantage of capturing and estimating the electron density profile rather than the total electron content. This is beneficial since it provides more fundamental information about the ionosphere and many ionospheric parameters can be derived from the electron density profile such as maximum peak height and value. This information can be used for a number of practical applications. For example the peak height of electron density is used in monitoring and predicting HF communication capabilities for aircraft polar routes.

The most commonly used model in ionospheric tomography is the voxel-based model. This model divides the ionosphere into voxels (pixels in three dimensions) where the electron density distribution within each voxel is considered to be constant (Colombo et al., 2000; Hernández-Pajares et al., 2000; Wen and Liu, 2010). The design matrix associated with this model is formed by computing lengths of the ray paths within the individual voxels (refer to Chapter 4 for more details). Inversion algorithms are then used to estimate the electron density values.

Three-dimensional voxel-based ionospheric modeling using tomographic techniques is an ill-posed (unstable with respect to measurement errors) and ill-conditioned (solution is highly sensitive to the values of the design matrix) inverse problem. The design matrix associated with the ionospheric tomography problem using only GNSS is nearly singular, due to the fact that the TEC measurements are biased in a vertical sense with no horizontal ray paths through the ionosphere, and the range of angles between the rays within a short period of time are not sufficient to extract the electron density without any a priori information. Additionally, the problem of ionospheric tomography is mixed-determined: that is there are regions where the data overdetermines parts of the solution but underdetermines other parts. In other words, not every voxel is intersected by one or more rays, which makes the electron density - the unknown - in these voxels unobservable and impossible to estimate without applying a constraint or using a priori information. These issues impose practical limitations to the ionospheric tomography solutions.

To overcome these limitations, many authors have used a functional representation of the electron density and transformed the problem to estimate the coefficients of orthogonal basis functions that describe the electron density distribution. Many functional representations of the electron density have been used by different authors. However, most of them share the utilization of Empirical Orthogonal Functions (EOF) to constrain the model vertically. Erturk et al. (2009) represented the electron density distribution globally as a summation of EOF, where the International Reference Ionospheric model IRI was used to derive EOFs. Mitchell and Spencer (2003) used the application of Spherical Harmonic Analysis (SHA) with Empirical Orthogonal Functions (EOF) to represent the data globally, using the solution to map the electron density over a restricted region. Spherical Harmonics Analysis (SHA) is well-suited for global representation but it is very demanding for high resolution models. To represent a field such as the electron density profile with a short wavelength, a high order of spherical harmonics is required. As the order and degree of the spherical harmonic expansion increases, the number of coefficients becomes too large. This imposes large memory requirements and leads to higher numerical computational cost. Also, higher order and degree generate numerical instabilities in estimating the coefficients. This makes the model unsuitable for modelling the ionosphere over a limited sector using a network of GNSS stations.

One region that has attracted a lot of attention in the past decade is the polar cap due to its importance and effect on radio propagation and communication especially during solar storms which might cause loss of communication and damage to electrical transmission equipment. The polar cap region has lacked spatial resolution of TEC measurements due to the orbit limitations of spaced-based measurements and sparse networks providing such measurements. To overcome these limitations, the Canadian High Arctic Ionospheric Network (CHAIN) was designed to develop a better understanding of the effect of solar-terrestrial activity on the Earth's environment. To make use of such a network and provide scientists with other cost effective sources of information to advance understanding of the ionosphere, a three-dimensional ionospheric tomographic model for a wide area GNSS network in the Canadian polar region is required.

1.2 Research Objectives and Contributions

The principle objective of this doctoral thesis is to develop an optimal tomographic model for determining ionospheric electron density distribution based on observations from a ground-based regional network of GPS stations in the Canadian polar region. The principle objective can be achieved by fulfilling the following sub-objectives:

- Implement a voxel-based ionospheric tomographic model.
- Develop a tool based on existing empirical ionospheric models, such as IRI-2007, to simulate the electron density distribution.
- Obtain a three-dimensional functional representation of the electron density distribution over a limited sector which reduces the number of unknowns to be estimated, hence reducing the computational load and memory requirement.
- Regularize the underdetermined ill-conditioned ionospheric tomography problem.
- Determine the most appropriate settings (K_{max} and Q values) of the three-dimensional functional representation of electron density distribution for the Canadian polar region.

The research contributions of this thesis include:

1) A novel Computerized Ionospheric Tomographic (CIT) technique using a voxel-based model to retrieve a three-dimensional description of the ionospheric electron density distribution.
2) An implementation of the proposed ionospheric tomographic technique in a MATLAB software package.
3) An assessment and validation of the performance of the developed tomographic technique using simulated and real GPS data under various ionospheric conditions. Limitations and potential of the technique are determined and quantified.
4) An introduction of a reference (pseudo TEC measurement) to estimate the receiver and satellite Inter-Frequency Biases (IFB)
5) A proposed approach (constraint) to overcome the limitation of bad geometry and undetected blunders of GPS real data.

1.3 Thesis Outline

This thesis consists of seven chapters:

- Chapter 1 states the research background and objectives.
- Chapter 2 introduces the fundamental concept of GPS, GPS observables, and error sources affecting GPS observables.
- Chapter 3 contains a review of the ionosphere characteristics and its effect on GPS signals.
- Chapter 4 describes the problem of ionospheric tomography and presents the development of a novel Computerized Ionospheric Tomographic (CIT) reconstruction technique for a voxel-based three-dimensional (3-D) tomographic model based on Empirical Orthogonal Functions (EOF) and Spherical Cap Harmonics (SCH). This

chapter also focuses on the extraction of the ionospheric delay observable (STEC) used to obtain a tomographic description of the electron density distribution using ground-based GPS data. Tikhonov regularization is also introduced to handle ill-posed problems such as ionospheric tomography.

- Chapter 5 provides an assessment of the implemented tomographic technique using simulated data. The optimal values of K_{max} and Q – order of SCH and number of EOF in the functional representation of the electron density in the proposed model – are also determined. These values are adopted for the processing of real data in Chapter 6. Simulations of different ionospheric conditions over the Canadian polar region are used to determine these values and investigate the capability of the technique to recover different ionospheric parameters such as electron density, TEC, electron density and maximum peak value. Nominal and storm conditions are simulated and the performance of the technique under these conditions is analyzed.
- Chapter 6 provides a performance analysis of the proposed technique with GPS real data. A pseudo TEC observation is introduced to estimate the satellite and receiver inter-frequency biases (IFB). One approach is proposed and used to overcome the limitation of bad data geometry and undetected errors associated with real data. The optimal values of K_{max} and Q determined in Chapter 5 are adopted in processing the data. Stability of the IFB and the radio occultation derived electron density profile are used to validate the results. A study of an ionospheric storm using the implemented CIT is conducted to demonstrate the applicability of the technique to monitor the ionosphere and provide a better understanding of the physical processes.

- Conclusions and recommendation for future work are presented in Chapter 7 based on development and assessment of the new CIT technique.

Chapter Two: The Global Positioning System (GPS)

2.1 Overview

The Global Positioning System (GPS) is a worldwide passive (one-way) satellite-based radio navigation positioning system that allows a GPS receiver to determine its position based on trilateration method. The system was approved and developed by the United States Department of Defense (DoD) starting in 1973 and has been fully operational since 1995. The principal objective of developing such a system was to enhance the effectiveness of U.S. and allied military forces by offering accurate estimates of position, velocity and time and, as a by-product, to serve the civilian community (Parkinson and Spilker, 1996). Due to the GPS near-global coverage and continuous services independent of the meteorological conditions, this military navigation system has become an important tool with many applications ranging from mapping and surveying to international air traffic management and global research. The GPS consists of three segments: space, control, and user segment. These are described in the next three sub-sections.

2.1.1 The Space Segment

The space segment utilizes at least 24 satellites (up to 32) with a minimum of four primary satellites orbiting in each of the six orbital planes that are inclined at 55 degrees with respect to the equatorial plane. The orbital altitudes are ~20,200 km, with periods of one-half sidereal day (~11.967h). The orbits are nearly circular, with slight perturbations due to non-sphericity of the Earth and solar radiation pressure (Hofman-Wellenhof et al., 2001). This orbital configuration is illustrated in Figure 2.1. This constellation ensures that almost all users with a clear sky view have a minimum of four satellites in view, providing 24-hour global use for navigation.

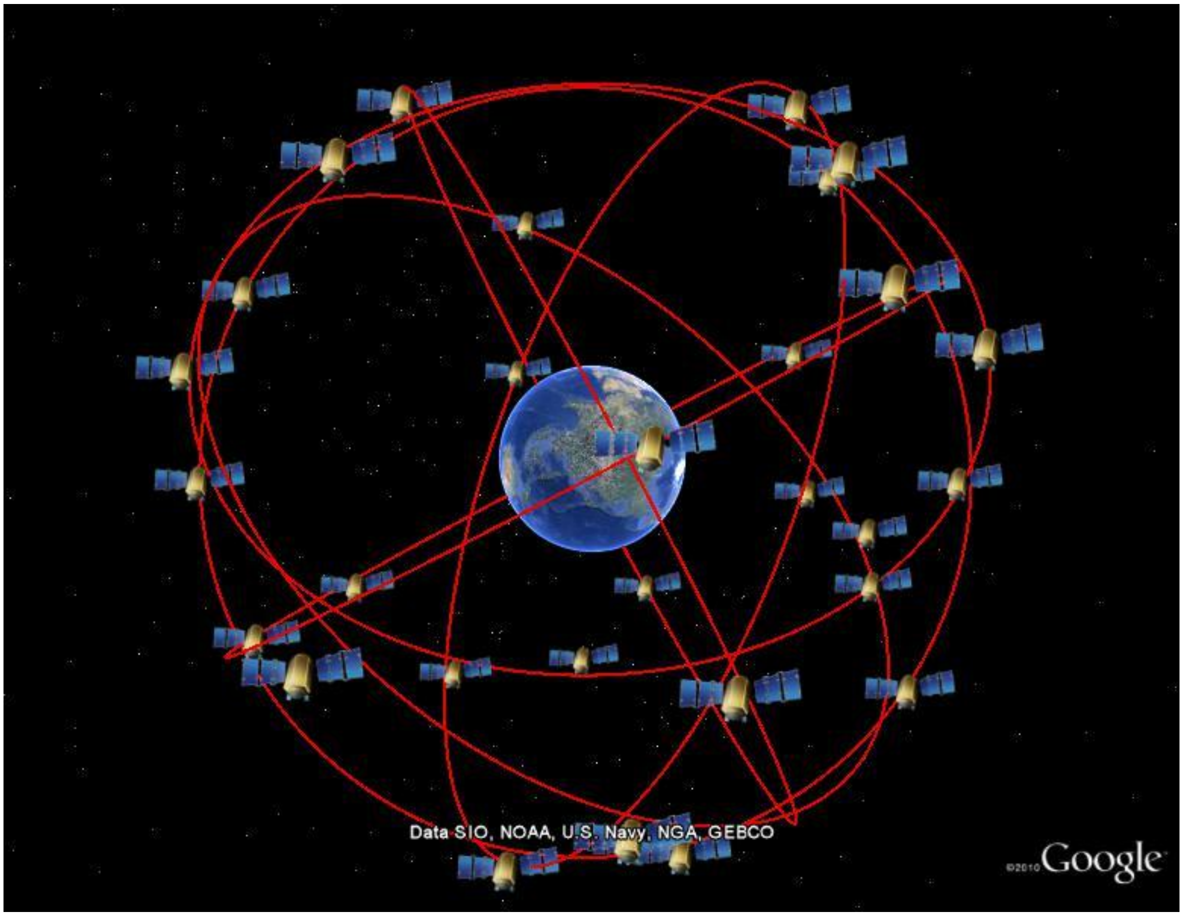

Figure 2.1: GPS orbital configuration

2.1.2 The Control Segment

The control segment of the GPS consists of 16 monitoring stations distributed globally, a Master Control Station (MCS), located at the Schriever Air Force Base (AFB) near Colorado Springs, Colorado, an alternate MCS located at the Vandenberg AFB, California, and 12 command and control ground antennas (“GPS Official Website”, 2013). The main responsibilities of the control segment are to monitor and maintain the satellites in their proper orbits through small commanded maneuvers, to determine and predict the satellite ephemerides and clock parameters, and to periodically upload satellites’ navigation messages (Hofmann-Wellenhof et al., 2007).

2.1.3 The User Segment

The user segment includes antennas and receivers of the military personnel and civilians which collect and process measurements from the GPS satellites that are in view to compute local position, velocity, and time. This process requires measurements from four satellites simultaneously to compute a unique position solution (in three dimensions), in addition to the receiver clock offset. With this capability, GPS has three main functions: navigation, precise positioning, and time and frequency dissemination. The reference frame used by the GPS is the World Geodetic System 1984 (WGS-84) which is a geocentric Earth-fixed system (Hofmann-Wellenhof et al., 2007).

2.2 GPS Signal Structure

The legacy GPS signals are broadcast on two L-band frequencies: L1 = 1575.42 MHz and L2 = 1227.60 MHz. These signals are modulated by several codes with certain characteristics. However, due to the increased need for improved accuracy and higher reliability, especially for life safety applications, GPS is undergoing continuing modernization efforts with new signals and bands. Since the number of satellites transmitting the modernized signals is limited, only measurements from legacy GPS signals are used and described in this section.

The legacy L1 signal is modulated by two pseudorandom noise (PRN) codes: Coarse/Acquisition code (C/A code) and Precise code (P-code). These codes consist of a digital sequence of random bits (zeroes and ones) with special properties allowing satellites to transmit at the same frequency without interfering with each other. The legacy L2 signal is modulated by the P-code which is encrypted and intended for military users only. However, by using special signal processing techniques in the receiver such as squaring and cross-correlation, measurement from legacy L2 signal can be recovered for civilian use (Hofmann-Wellenhof et al., 2007).

C/A and P codes are repeated every 1 millisecond and 1 week, respectively, with chipping rates of 1.023 MHz and 10.23 MHz, respectively. The difference in the chipping rate, hence chip width (300 m for C/A code and 30 m for P-code), results in greater precision in the range measurements for P-code than that for C/A-code. In addition to the pseudorandom codes, both signals are modulated by a binary-coded message referred to as the navigation message which contains data on the satellite health status, orbit and clock, and ionospheric corrections (Misra and Enge, 2006). The navigation message is transmitted at a rate of 50 bits per second (bps) with 20 ms bit duration. Table 2.1 summarizes relevant components of the satellite signals.

Table 2.1: Components of the GPS satellite signal (after Hofmann-Wellenhof et al., 2007)

Component	Frequency (MHz)
Fundamental frequency	$\mathbf{f_0 = 10.23}$
Carrier L1	$\mathbf{154f_0 = 1575.42\ (\lambda_1 = 19.0\ cm)}$
Carrier L2	$\mathbf{120f_0 = 1227.60\ (\lambda_2 = 24.4\ cm)}$
P-code	$\mathbf{f_0 = 10.23}$
C/A code	$\mathbf{f_0/10 = 1.023}$
Navigation message	$\mathbf{f_0/204600 = 50 \times 10^{-6}}$

The L1 and L2 signals transmitted by the kth satellite can be expressed mathematically as:

$$\begin{aligned} S_{L1}^{(k)} &= \sqrt{2P_C}\,x^{(k)}(t)D^{(k)}(t)\cos(2\pi f_{L1}t + \theta_{L1}) \\ &\quad + \sqrt{2P_{Y1}}\,y^{(k)}(t)D^{(k)}(t)\sin(2\pi f_{L1}t + \theta_{L1}) \\ S_{L2}^{(k)} &= \sqrt{2P_{Y2}}\,y^{(k)}(t)D^{(k)}(t)\sin(2\pi f_{L2}t + \theta_{L2}) \end{aligned} \tag{2.1}$$

where:

P_C, P_{Y1}, and P_{Y2} are signal powers for C/A code on L1 and P(Y) codes on L1 and L2 respectively (m)

$x^{(k)}$ and $y^{(k)}$	are the C/A and P(Y) code sequences of the k^{th} satellite
$D^{(k)}$	is the navigation data message of the k^{th} satellite
f_{L1} and f_{L2}	are the carrier frequencies corresponding to L1 and L2 respectively (Hz)
θ_{L1} and θ_{L2}	are the carrier phase offsets on L1 and L2 respectively (cycles)

In late 1990's, GPS modernization was launched to expand the benefits of GPS for civil applications. The project includes two new civil signals: L2C and L5. L2C signal is transmitted on the L2 frequency, as L2 with two multiplexed PRN codes: Civilian Moderate length code (CM) and Civilian Long length code (CL). The CM code has a length of 10,230 chips repeating every 20 ms, and CL code has a length of 767,250 chips repeating every 1500 ms. Both codes are transmitted at 511.5 kbit/s. However, they are multiplexed together to form the new code L2C, which has the same 1.023 MHz chipping rate as the C/A codes. The L5 signal is transmitted on the L5 frequency (1176.45 MHz) offering two carrier frequency components: in-phase (I) and quadrature-phase (Q). The Q channel is a data-less channel, transmitting a pilot signal modulated with a spreading code. The I channel is modulated with the navigation data and a spreading code. Both codes are 10,230 chips in length and transmitted at 10.23 MHz, repeating every 1 ms. Currently, there are ten satellites transmitting L2C signals and three satellites transmitting L5 signals ("The United States Naval Observatory", 2013).

2.3 GPS Observables

Generally, the Global Positioning System provides three observables: pseudorange, carrier phase, and Doppler. A code tracking loop (delay lock loop) correlates the incoming signal with replicas generated in the receiver to provide the apparent transit time of a signal from a satellite to the receiver. Multiplication of the transit time by the speed of light in a vacuum results in derivation of a pseudorange. A carrier phase tracking loop (phase lock loop) provides the phase difference between the received signal and the sinusoidal signal generated by the receiver. The time derivative of the carrier phase observation is the Doppler measurement. Ideally, the receiver acquiring phase lock with the incoming signal would measure the initial fractional phase difference between the received and receiver-generated signal plus the total number of full carrier cycles between the satellite and the receiver. However, a GPS receiver cannot distinguish between cycles of the received carrier wave. In reality, the receiver measures the fractional phase and then keeps track of the changes in this measurement; the initial phase, which is an integer number of full cycles referred to as carrier phase ambiguity (N), is left undetermined. Estimation of N is referred to as integer ambiguity resolution.

2.4 GPS Error Sources

The carrier phase observable is more precise than the pseudorange but is ambiguous by the carrier phase ambiguity. However, both measurements are subject to errors from various sources which reduce the accuracy of GPS positioning. These errors can be grouped into satellite-based errors (such as orbital errors and satellite clock errors), receiver-based errors (such as receiver clock errors and noise), and signal propagation errors (such as ionospheric and tropospheric delays and multipath). These errors are illustrated in Figure 2.2 and are included in the following equations describing the pseudorange, carrier phase and Doppler observables:

$$P_i = \rho + d\rho + c(dt - dT) + d_{trop} + I_i + c\frac{f_1^2}{f_i^2}\left(T_{GD,r}^{P} - T_{GD,s}^{P}\right) + \varepsilon_{P,i} \qquad (2.2)$$

$$\Phi_i = \lambda_i \phi_i = \rho + d\rho + c(dt - dT) + d_{trop} - I_i + c\frac{f_1^2}{f_i^2}\left(T_{GD,r}^{\Phi} - T_{GD,s}^{\Phi}\right) + \lambda_i N_i + \varepsilon_{\Phi,i} \qquad (2.3)$$

$$\dot{\Phi}_i = \dot{\rho} + d\dot{\rho} + c\left(d\dot{t} - d\dot{T}\right) + \dot{d}_{trop} - \dot{I}_i + \varepsilon_{\dot{\Phi},i} \qquad (2.4)$$

where:

P , Φ , $\dot{\Phi}$	are the code pseudorange (m), the carrier phase (m), and the Doppler (m/s), respectively
ϕ	is the carrier phase observable in cycles
λ	is the carrier wavelength (m)
ρ	is the geometrical range between the receiver and the satellite (m)
$\dot{\rho}$	is the geometrical range rate between the receiver and the satellite (m/s)
$d\rho$	is the orbital error (m)
$d\dot{\rho}$	is the velocity error (m/s)
c	is the speed of light (m/s)
dt, $d\dot{t}$	are the satellite clock error (m) and clock drift error (m/s), respectively
dT, $d\dot{T}$	are the receiver clock error (m) and clock drift error (m/s), respectively
d_{trop}, $\dot{d}_{trop}$	are the tropospheric delay (m) and drift (m/s), respectively
I, $\dot{I}$	are the ionospheric delay (m) and drift (m/s), respectively
N	is the carrier phase ambiguity (cycles)
$T_{GD,s}$, $T_{GD,r}$	are the satellite and receiver modulation offsets, respectively, which are different for code versus carrier-phase (m)
ε	is the random error due to receiver noise and multipath
i	is a subscript denoting GPS carrier frequencies ($f_1 = 1575.42$ MHz and $f_2 = 1227.60$ MHz)

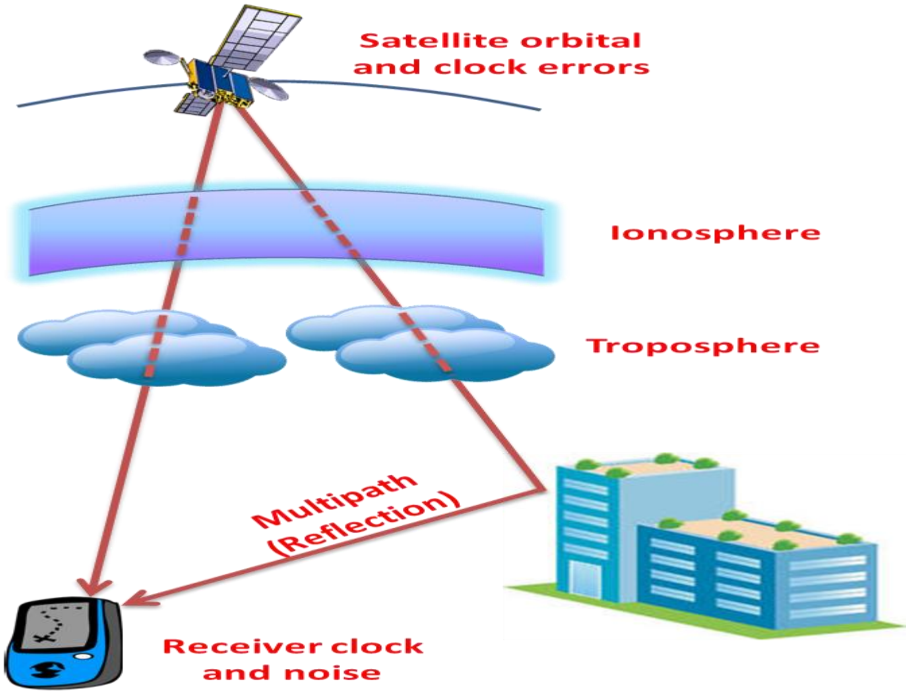

Figure 2.2: GPS Error Sources

2.4.1 Orbital Errors

The broadcast ephemerides are estimated and predicted by the MCS of the control segment using data collected at the GPS monitor stations. The predicted ephemerides are uploaded to the GPS satellites and broadcast back to the users in the form of a navigation message. These ephemerides are associated with small errors, which grow with the age of the ephemerides data. The error growth is slow and smooth, and only the radial component of the ephemerides error produces an error in the range. The range error due to orbital errors is on the order of 0.8 m(1σ) (Kaplan, 2005).

2.4.2 Satellite Clock Errors

GPS satellites are equipped with an atomic clock: a rubidium or cesium oscillator. Although these clocks are extremely accurate, they suffer from a drift with respect to GPS time that could be as large as 1 ms; multiplied by speed of light this represents 300-km pseudorange error.

Therefore, a correction of the clock is required. The MCS computes and uploads the clock correction parameters to the satellites and rebroadcasts them in the navigation message. Satellite clock corrections can be applied to the measurements using ("Interface Specification, IS-GPS-200F", 2011):

$$\delta t_{clk} = a_{f0} + a_{f1}(t - t_{oc}) + a_{f2}(t - t_{oc})^2 + \Delta t_r \qquad (2.5)$$

where:

a_{f0}	is the clock bias (s)
a_{f1}	is the clock drift (s/s)
a_{f2}	is the frequency drift (s/s^2)
t	is the current epoch (s)
t_{oc}	is the clock data reference time (s)
Δt_r	is the correction due to relativistic effects (s)

The correction due to relativistic effects Δt_r is caused by the eccentricity of the satellite's orbit. This time-dependent effect can be as large as 45 ns, corresponding to a ranging error of about 14 m, depending upon the position of the satellite. This correction is computed using ("Interface Specification, IS-GPS-200F", 2011):

$$\Delta t_r = F. e. \sqrt{a} \sin E_k \qquad (2.6)$$

where:

$F =$	$-4.442807633 \times 10^{-10}\,\mathrm{s/m^{1/2}}$
e	is the satellite orbital eccentricity (unitless)

a is the semi-major axis of the satellite orbit (m)

E_k is the eccentric anomaly of the satellite orbit (radians)

The satellite clock error can be computed using Equations (2.5) and (2.6); however, some residual error remains in the range 0.3-0.4 m of equivalent ranging error, depending on the age of broadcast data and clock type (Kaplan, 2005).

2.4.3 Receiver Clock Errors

The receiver clock error (bias) is the difference between the time observed by the receiver oscillator and the reference GPS time. This error varies with time and affects all range measurements by the same amount for a fixed epoch. The receiver clock errors are higher than the satellite clock errors since receivers use less expensive oscillators than those on satellites such as low-cost quartz clock, temperature compensated crystal oscillator (TCXO), oven controlled crystal oscillator (OCXO), or Rubidium oscillator. However, this time-varying error can be estimated as an unknown along with the receiver position or eliminated by differencing techniques.

2.4.4 Receiver Noise

The receiver noise error includes noise introduced by the antenna, amplifiers, cables, and the receiver. The receiver is capable of measuring the phase with a precision of 1/2 % – 1% of a cycle; corresponding to ~2 mm. However, the noise level on the code measurement is much higher, with typical errors of few decimeters (Misra and Enge, 2006).

2.4.5 Multipath

Multipath is the arrival of a signal at the receiver antenna via multiple paths. This phenomenon results from the reflection of the signal from surfaces and structures in the vicinity such as buildings, streets and vehicles, and from the ground. Multipath affects both pseudorange and carrier phase measurements. Typical multipath errors in pseudorange measurements are on the order of several metres, while the maximum multipath error on the carrier phase measurements does not exceed a quarter cycle (Kaplan, 2005).

2.4.6 Tropospheric Errors

The troposphere is the lower part of the atmosphere, extending from the Earth's surface to about 50 km altitude. The refractive index of the atmosphere is larger than unity, causing the speed of propagation to be lower than that in free space and the signal to be delayed. This delay, referred to as tropospheric delay, is a function of temperature, pressure and humidity and can be divided into two parts: hydrostatic (dry) delay and wet delay. The hydrostatic delay is responsible for 90% of the tropospheric delay and can be accurately estimated using empirical models or surface measurements. On the other hand, the wet delay, corresponding to 10% of the delay, is more difficult to model due to the variation of water vapour in the lower atmosphere. The troposphere is a non-dispersive medium at GPS frequencies; the tropospheric delay is frequency independent. Both pseudorange and carrier phase measurements at L1 and L2 frequencies experience a common tropospheric delay. Therefore, this delay cannot be derived using dual-frequency GPS measurements, and tropospheric models (such as Saastamoinen and Hopfield models) must be used to correct for this delay (Misra and Enge, 2006).

2.4.7 Ionospheric Errors

The ionosphere is the region of the atmosphere from about 60 km to more than 1500 km above the Earth surface. The ionospheric delay is the main error source for GPS. The delay can vary from a few meters to tens of meters depending on the solar cycle, hour of day, season, geographic location and satellite elevation angle. The effect on pseudorange and carrier phase is the same but opposite in sign; the carrier phase is advanced and the pseudorange is delayed. The ionospheric delay is proportional to the total number of electrons along the path of propagation, referred to as Total Electron Content (TEC). TEC is often expressed in units of TEC units (TECU), where 1 TECU is equal to 10^{16} electrons/m^2. TEC is defined as

$$\mathrm{TEC} = \int_{\mathrm{path}} \mathrm{N_e} . \mathrm{ds} \qquad (2.7)$$

where $\mathrm{N_e}$ is the electron density along the signal path. The ionosphere is a dispersive medium, i.e. the delay is frequency dependent. Therefore, a dual-frequency receiver can be used to estimate the ionospheric delay (Kaplan, 2005) and correct for the first-order ionospheric range error. Derivation of ionospheric delay from dual frequency GPS measurements is shown in Chapter 4.

2.5 Satellite Geometry

GPS positioning is based on a trilateration technique. Therefore, satellite geometry relative to the user plays a crucial role and influences the accuracy of GPS positioning. A common metric to quantify the effect of satellite geometry on GPS position accuracy is Dilution of Precision (DOP). A low numeric DOP value represents good satellite geometry, whereas a high value represents poor satellite geometry. In general, the larger volume over which the satellites are distributed the better the geometry. Figure 2.3 shows examples of good and poor satellite geometry.

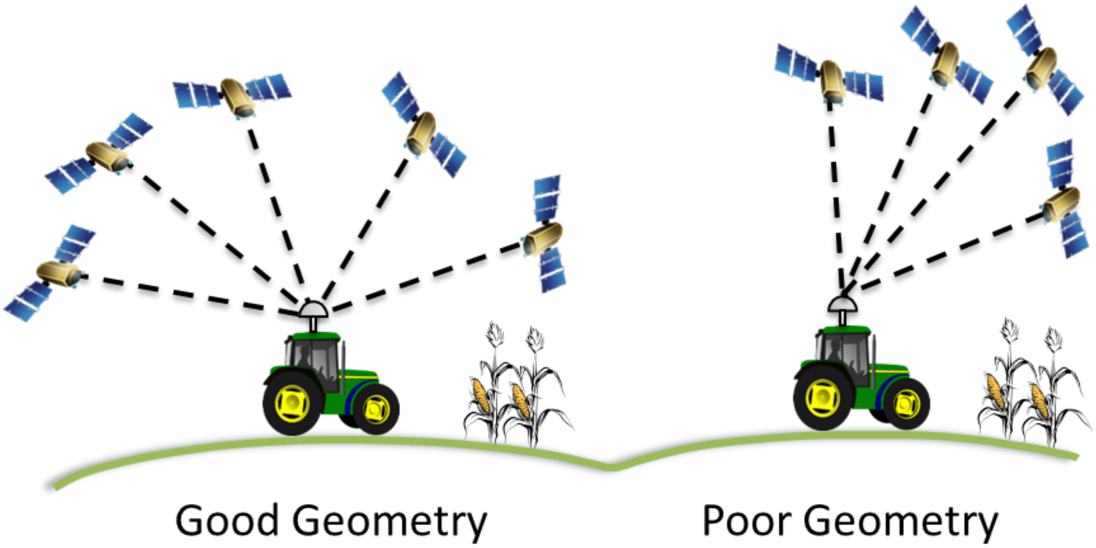

Figure 2.3: Good and poor satellite geometry

GPS positioning accuracy is a function of measurement accuracy as well as the satellite geometry. The various errors described in the previous sections affect the GPS range observation accuracy. This can be translated into position/time accuracy using the following rule-of-thumb:

$$\text{Position Accuracy} = \text{DOP} \times \text{Range Accuracy} \tag{2.8}$$

Several DOP forms are used to describe the accuracy of position and time. This includes Position Dilution of Precision (PDOP), Horizontal Dilution of Precision (HDOP), Vertical Dilution of Precision (VDOP), and Time Dilution of Precision (TDOP). Geometric Dilution of Precision (GDOP) is another useful form that characterizes the impact of the satellite geometry on the position and time solution. Using these many DOP forms, the effect of satellite geometry on estimating the position and time (GDOP), receiver 3D position (PDOP), horizontal position

(HDOP), vertical position (VDOP), easting position (EDOP), northing position (NDOP), and receiver clock bias (TDOP) can be quantified using the following:

$$
\begin{aligned}
&\text{3D Positionining Accuracy} \quad = \text{PDOP} \times \text{Range Accuracy}\\
&\text{Horizontal Positioning Accuracy} = \text{HDOP} \times \text{Range Accuracy}\\
&\text{Vertical Positioning Accuracy} = \text{VDOP} \times \text{Range Accuracy}\\
&\text{Northing Positioning Accuracy} = \text{NDOP} \times \text{Range Accuracy}\\
&\text{Easting Positioning Accuracy} = \text{EDOP} \times \text{Range Accuracy}\\
&\text{Timing Accuracy} = \text{TDOP} \times \text{Range Accuracy}
\end{aligned}
\qquad (2.9)
$$

2.6 Differential GPS

Differential GPS (DGPS) is a technique that enhances the accuracy of GPS-derived position solutions. This approach makes use of the fact that GPS measurements are spatially and temporally correlated. This technique involves the use of reference stations at accurately known locations. Collecting GPS measurements at the reference receivers, errors common to the remote and reference receivers are estimated at the reference site and transmitted in a form of corrections to the user. The user, in turn, applies these corrections to obtain a more accurate position solution. Most of the errors discussed earlier can be mitigated except for noise and multipath which are receiver and environment dependent and cannot be corrected using DGPS.

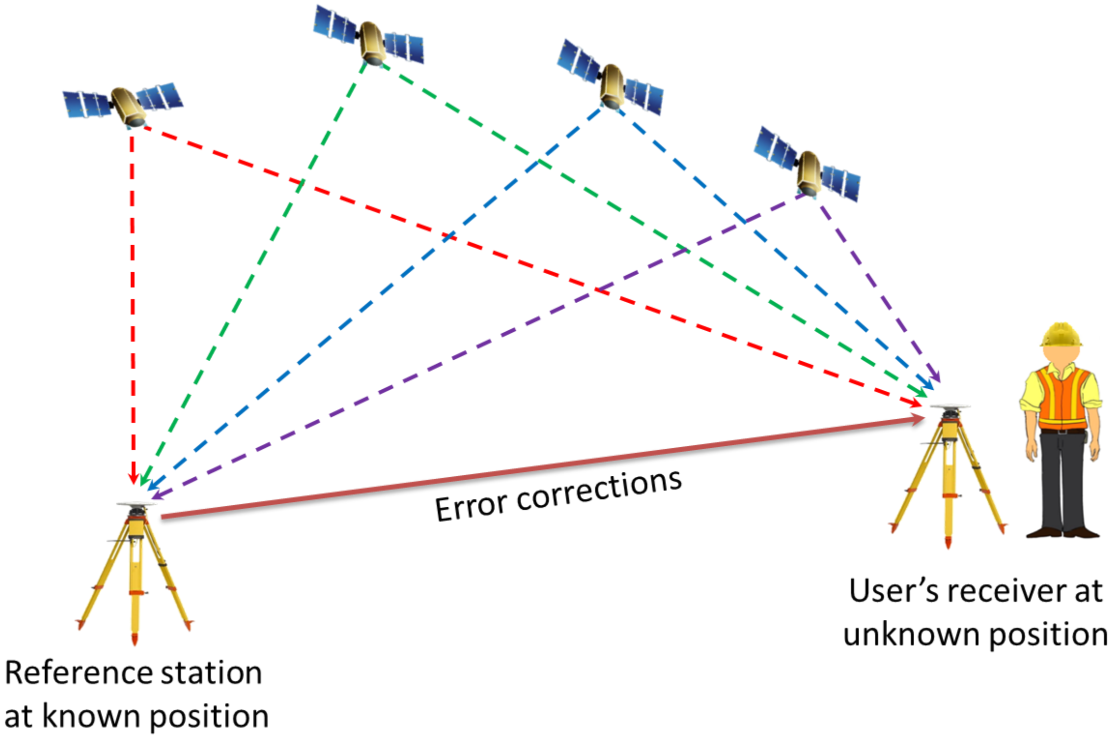

Figure 2.4: Differential GPS

Local-Area Differential GPS (LADGPS) and Wide-Area Differential GPS (WADGPS) are two common forms of DGPS (Rao, 2010). In LADGPS, the reference receiver is generally located within line-of-sight and the corrections sent to the user via a radio link account for ionospheric, satellite clock, and ephemeris errors at the reference station. In WADGPS, the corrections are determined using multiple reference stations distributed over a continent-wide geographic region (Figure 2.5). Corrections are transmitted to the user in real time via geostationary satellite downlinks or through a network of ground based transmitters. Wide Area Augmentation System (WAAS) (FAA, 2013) and European Geostationary Navigation Overlay Service (EGNOS) (ESA, 2013) are examples of WADGPS.

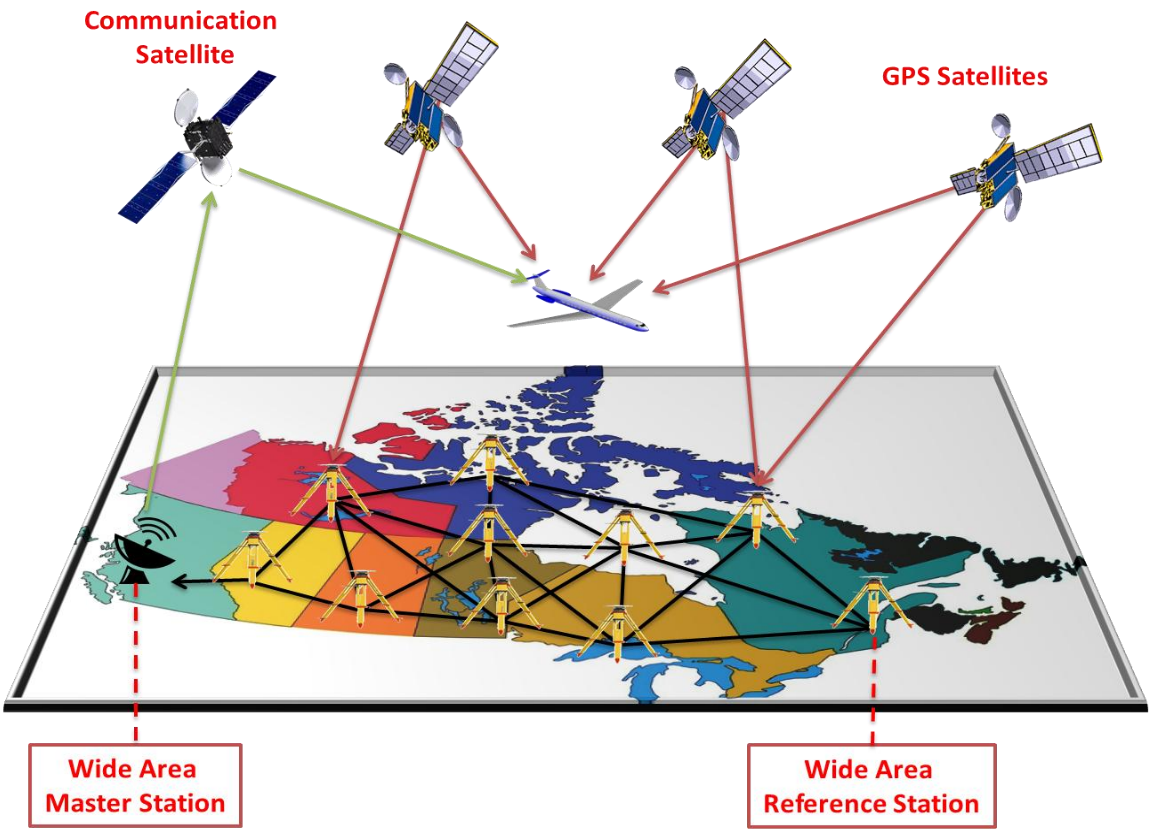

Figure 2.5: Wide Area Differential GPS System

Chapter Three: The Ionosphere

The ionosphere is the part of the Earth's atmosphere which extends from approximately 60 km to more than 1500 km altitude. It results from the interaction of solar emissions (solar x-ray and extreme ultraviolet radiation) with the Earth's neutral atmosphere. This interaction controls the ionization process, which in turn affects the electron production in the ionosphere. The evolution of the ionosphere and its electron content varies in space and time (with solar cycle, seasonal, and local time) and geographical location (low, mid, and high latitude, auroral and equatorial regions) (Araujo-Pradere et al., 2005).

3.1 Structure of the Ionosphere

Ionization occurs at a number of atmospheric levels. It is mainly controlled by solar radiation and solar activities. Having different compositions at different altitudes of the atmosphere, ionization generates layers that may be identified by their interaction with radio waves. These layers are shown in Figure 3.1 and described as follows:

- Layer D: extends from 60 km to 90 km. This layer is generated by the hard X-radiation of the sun, and the main effect of this layer is absorbing radiation. Due to the recombination of ions and electrons, this region is reduced greatly after sunset.
- Layer E: extends from 90 km to 140 km. Ionization (primarily of molecular oxygen) in this layer is due to soft X-radiation of the sun and far ultraviolet solar radiation. This layer is highly variable in space and time, where it is present during the day and reduced by night. Sometimes, disturbances might occur in the ionosphere causing large enhancements of electron density in some limited altitude range. When this feature appears, a "Sporadic E" layer is said to be present.

- Layer F: extends from 140 km to 1000 km. Ionization of atomic oxygen (O) by extreme ultraviolet solar radiation generates this layer. The F layer, also known as the Appleton layer, is the highest significant layer of the ionosphere in terms of radio wave communication. The central part of the F layer has the greatest electron density in the Earth's atmosphere. This layer is divided into two sub-layers:
    - F1 Layer: extends from 140 km to 220 km altitude and only exists during daytime. This is due to the nightside neutral wind which lifts the electrons, thus the layer, to higher altitude.
    - F2 Layer: extends from 220 km to 1000 km altitude. This layer contains the maximum value of the electron density profile at approximately 300 km altitude.

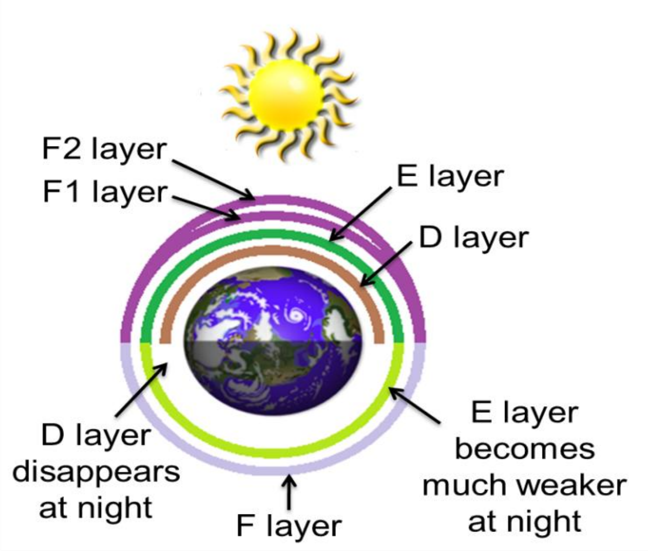

Figure 3.1: Ionospheric layers. at night, F1 and F2 layers combine into F layer and D layer disappears

3.2 Ionospheric Characteristics

The ionospheric electron density – an ionospheric characteristic of interest to GPS – varies spatially and temporally. Spatial variations are geographic position dependent while temporal variations are Sun dependent. The following major electron density variations are briefly discussed.

3.2.1 Diurnal Variation

The electron densities vary diurnally in an Earth-fixed reference frame. The rate of change of electron density depends on the production rate, loss rate by recombination and transport processes. The rate of ionization depends on solar radiation. Higher solar radiation intensity leads to higher electron density. Figure 3.1 shows typical day/night electron density profiles. During the day, the source of radiation, the Sun, stimulates the production of electron density. At night, the recombination reaction is still in place but the source of radiation is removed causing a decrease in the rate of ionization and hence decaying of the electron density. The electron density reaches its maximum value at 1400 Local Time (LT) and has a minimum value at sunrise; the dayside maximum is 4-6 times larger than the minimum values.

3.2.2 Latitudinal Variation

The ionosphere can be divided into three regions based on latitude: low-latitude (or equatorial) region, mid-latitude region and high latitude (auroral and polar) region. In the low latitude region, an equatorial anomaly develops near the geomagnetic equator. These anomalies are caused indirectly by the neutral wind motions and by the combined action of ionospheric electric and magnetic fields. The equatorial anomaly causes a minimum of electron density at the magnetic equator and produces two peaks of electron density approximately 20º north and south of the geomagnetic equator. In mid-latitudes the variations are more regular, but the high latitudes are more affected by unpredictable variations that are dominated by the geomagnetic field (Brunini, 1998).

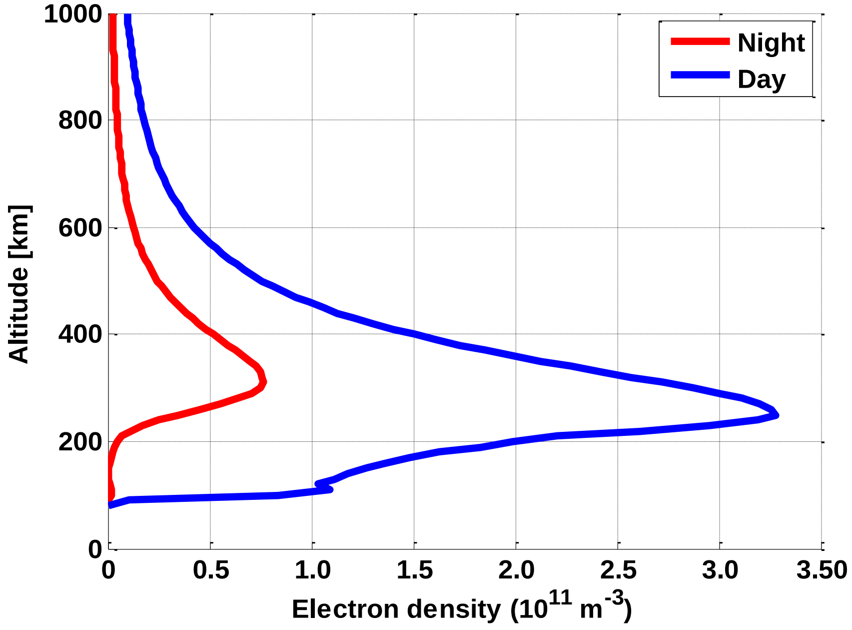

Figure 3.2: Typical day/night electron density profiles.

3.2.3 Seasonal Variation

The electron density production and recombination rate depends on number of atomic O and N_2, respectively. The recombination process of N_2 is affected by temperature. The colder the N_2, the less effective recombination with electrons leading to higher number of electrons. Therefore, higher electron density concentrations are observed near equinoxes in winter, while lower concentrations are observed in summer.

3.2.4 Solar Cycle Variation

The Sun is the source of many solar emissions that interact with the neutral atmosphere forming the ionosphere. Therefore, the ionosphere is highly correlated with solar activity. Solar activity is quantified by the sunspot number (SSN). Sunspots are dark regions (compared to the surrounding regions) on the photosphere of the sun, lying mainly between solar latitudes 5° and 30° caused by intense magnetic activity. The Sun exhibits an 11-year sunspot cycle, known as the solar cycle. Figure 3.3 shows the solar cycle between 1954 and 2012. The strongest solar cycle occurred in 1957 and the next peak is expected to occur in 2013-2014. During solar maximum, the solar energetic emissions increase significantly affecting the ionosphere. These emissions interact with the ionosphere releasing more electrons which in turn affect GPS measurements.

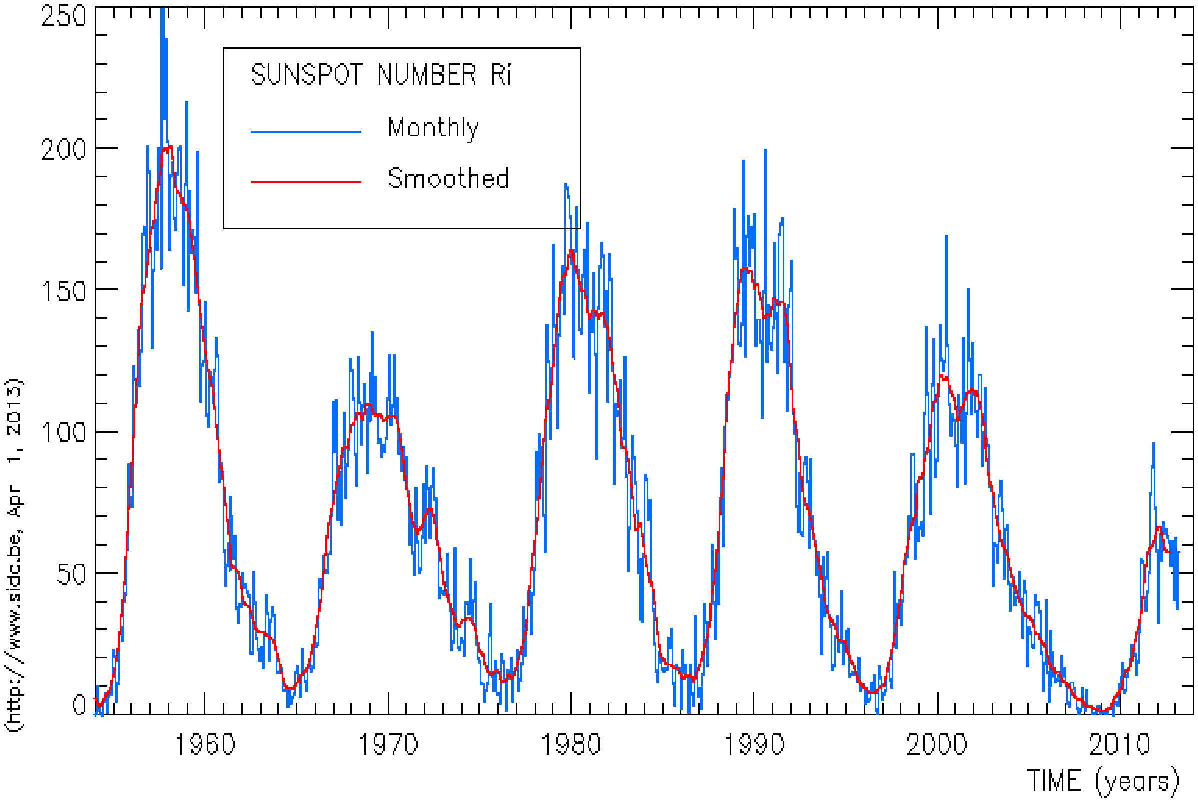

Figure 3.3: Monthly and monthly smoothed sunspot numbers since 1954. (http://sidc.oma.be/html/wolfmms.html, April 2013)

3.3 Ionospheric Models

3.3.1 Chapman Profile

The electron density profile in height can be described using a Chapman profile (Kelley, 2009). Assuming hydrostatic equilibrium of a mass element with respect to the Earth's surface and the atmosphere approximation as an ideal gas, an expression for the electron density can be derived. The final expression for a Chapman profile can be written as follows (Hargreaves, 1995):

$$N_e(h,\chi) = N_{e,0}e^{\frac{1}{2}\left(1-\frac{h-h_{m,0}}{H}-\sec(\chi)e^{-\frac{h-h_{m,0}}{H}}\right)} \tag{3.1}$$

where $N_{e,0} = (q_{m,0}/\alpha)^{\frac{1}{2}}$, $q_{m,0}$ is the peak ionization rate, α is the mean dissociative coefficient for the molecular ions, $h_{m,0}$ and H are the reference and scale heights respectively, and χ is the sun zenith angle. Assuming a reference height ($h_{m,0}$) of 300 km, a scale height (H) of 75 km and $N_{e,0} = 10^{12}$ el/m^3, different profiles for different sun zenith angles (χ) are shown in Figure 3.4.

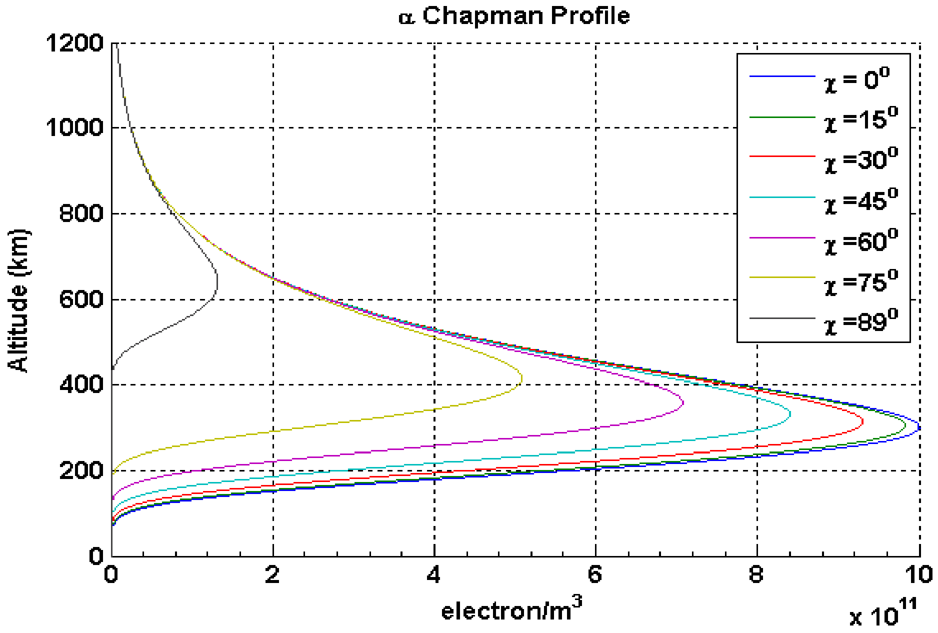

Figure 3.4: Different electron density profiles based on different sun zenith angles using Chapman profile. (scale height = 75 km, reference height = 300 km, and $N_{e,0}$= 10^{12} el/m^3).

3.3.2 International Reference Ionosphere (IRI)

The International Reference Ionosphere (IRI) is an international scientific project sponsored by the Committee on Space Research (COSPAR) and the International Union of Radio Science (URSI). For a given location, time, date and sunspot number, the IRI model describes the median values of electron density, the electron temperature, and ion composition in the altitude range 50 km to 2000 km. The major data sources for the IRI model are the worldwide network of ionosondes, the powerful incoherent scatter radars, the International Satellites for Ionospheric Studies (ISIS) and Alouette topside sounders, and in situ instruments on several satellites and rockets (Bilitza and Reinisch, 2008).

3.3.3 Parameterized Ionospheric Model (PIM)

The Parameterized Ionospheric Model (PIM) is a global ionospheric and plasmaspheric model based on combined output from the Global Theoretical Ionospheric Model (GTIM) model for low and middle latitude with output from the Time Dependent Ionospheric Model (TDIM) for high latitudes and from the empirical Gallagher plasmaspheric model (AIAA, 1999). PIM produces electron density profiles between 90 and 25000 km altitude, in addition to other profile parameters such as corresponding critical frequencies and heights for the ionospheric E and F2 regions, and Total Electron Content (TEC) (Daniell et al., 1995). Figure 3.5 is an example of a profile for the same geographical coordinates and epoch using IRI-2007 and PIM models.

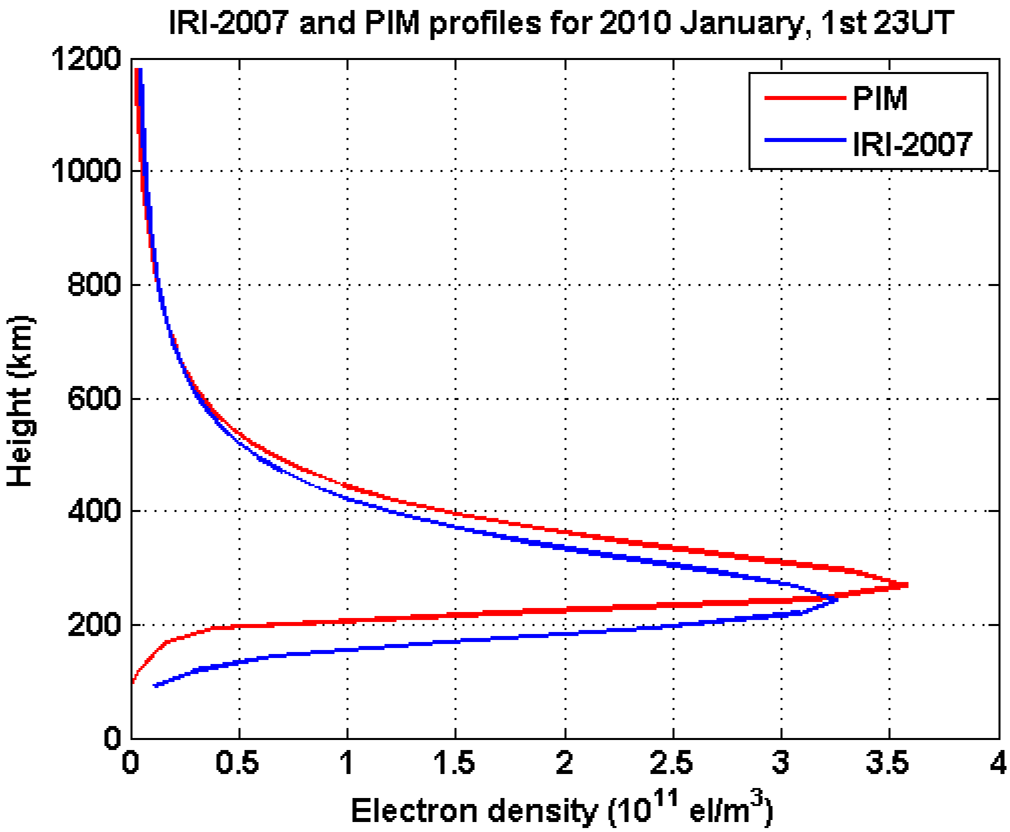

Figure 3.5: IRI-2007 and PIM profiles (Calgary, Canada 51.05° N, 114.07° W) .

3.4 Ionospheric Effects on GPS Signals

Electromagnetic signals propagating from a GPS satellite to a GPS receiver on the Earth's surface travel through the ionized layer of the atmosphere, i.e. the ionosphere. The ionosphere is a dispersive medium with respect to the GPS signal: the refractive index, and hence the ionospheric delay, is a function of the carrier frequency. In deriving the GPS observables it is assumed that the signal travels at speed of light in a vacuum (index of refraction is equal to one). Due to the ionospheric refractive index differing from a value of one, GPS signals are significantly affected by the ionosphere, in terms of modifying the traveling speed of the signal with respect to the speed of light. This induces two effects: 1) group delay of the signal modulation and 2) carrier phase advance. The following expression relates the phase (n_p) and the group (n_g) indices of refraction (Hofman-Wellenhof et al., 2001):

$$n_g = n_p + f\frac{dn_p}{df} \tag{3.2}$$

where f is the system operating frequency, in Hz. According to Seeber (2003), the phase refractive index (n_p) can be approximated by truncating the series expansion after the quadratic term:

$$n_p = 1 + \frac{c_2}{f^2} \tag{3.3}$$

Differentiating Equation (3.3)

$$dn_p = -2\frac{c_2}{f^3}df \tag{3.4}$$

And by substituting Equations (3.4) and (3.3) into Equation (3.2), an expression for the group index of refraction can be derived:

$$n_g = 1 - \frac{c_2}{f^2} \tag{3.5}$$

The value c_2 does not depend on frequency but on the quantity of the electron density N_e and is defined as (Seeber, 2003)

$$c_2 = k.N_e[Hz^2] \quad \text{where} \quad k = -40.3\ m^3/(s^2.el) \tag{3.6}$$

On the other hand, the measured range between a transmitter and a receiver can be defined using Fermat’s principle:

$$s = \int_{\mathrm{path}} n.\, ds \tag{3.7}$$

Assuming n =1, the geometric range s_0 is obtained:

$$s_0 = \int_{\mathrm{path}} ds \tag{3.8}$$

The difference (I) between measured range s and geometric range s_0 is called ionospheric delay:

$$I = s - s_0 = \int_{\mathrm{path}} (n - 1).\, ds \tag{3.9}$$

Since there are two refractive indices for the ionosphere, one for phase and the other for group, there will be an ionospheric range error associated with each index. Substituting Equations (3.3) and (3.5) into Equation (3.9) results in the following range errors:

$$I_g = \frac{40.3}{f^2} \int_{\mathrm{path}} N_e.\, ds \qquad I_p = -\frac{40.3}{f^2} \int_{\mathrm{path}} N_e.\, ds \tag{3.10}$$

Defining the Slant Total Electron Content (STEC) as the integration of the electron density N_e along the signal path:

$$\mathrm{STEC} = \int_{\mathrm{path}} N_e.\, ds \tag{3.11}$$

and substituting Equation (3.11) into Equation (3.10) yields:

$$I_g = \frac{40.3}{f^2} \mathrm{STEC} \qquad I_p = -\frac{40.3}{f^2} \mathrm{STEC} \tag{3.12}$$

Therefore, the ionospheric effect on a GPS signal is equal in magnitude but opposite in sign for group versus phase: that is, an advance in phase and delay in group. As can be seen from Equation (3.12), the ionospheric delay is proportional to STEC and is inversely proportional to the square of the signal frequency being transmitted. The STEC is expressed in units of TEC units (TECU), where 1 TECU is defined as 10^{16} electron contained in a 1-m^2 column along the path of the signal from the transmitter to the receiver. STEC can be easily converted to ionospheric delay for the L1 and L2 frequencies using Equation (3.12), where:

For L1, 1 TECU = 0.16 m of range delay

For L2, 1 TECU = 0.27 m of range delay

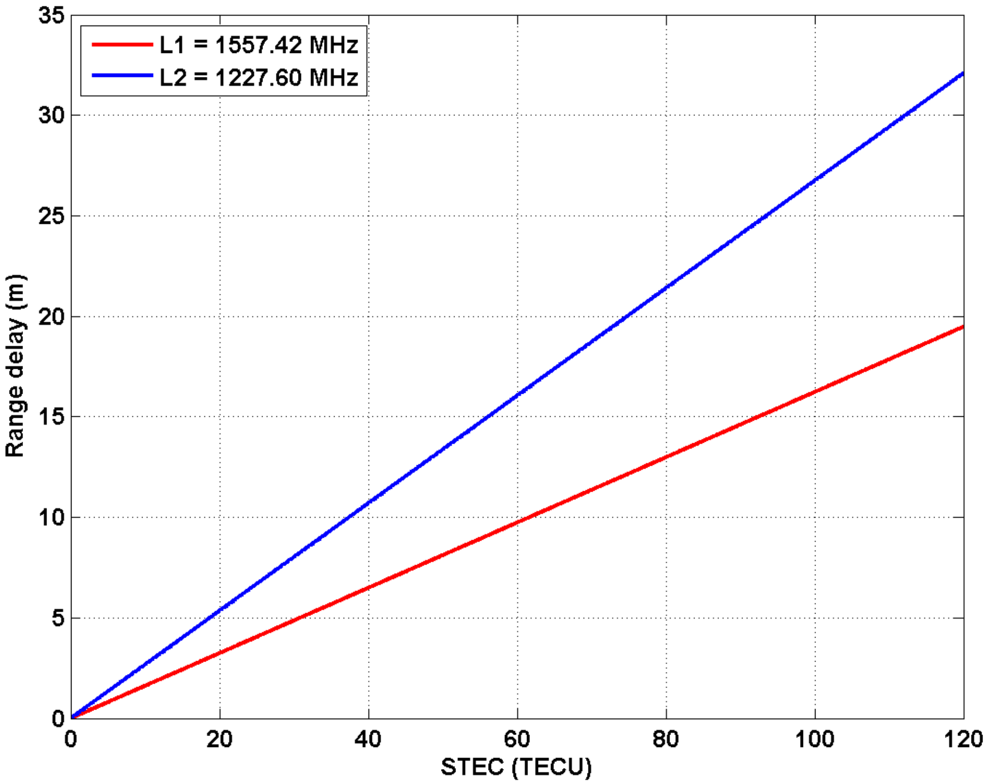

Figure 3.6: Ionospheric range delay using Equation (3.12)

3.5 TEC Variation

The TEC is the integration of the number of electrons in a vertical column with a cross-sectional area of 1 m^2. Therefore, the variation of TEC is similar to that of the electron density, i.e., temporally and spatially. The value of TEC varies diurnally, seasonally and in accordance with the 11-year solar cycle. The diurnal maximum TEC occurs at 14:00 LT with a possible secondary maximum at 22:00 LT and the minimum TEC occurs just before sunrise due to the recombination of electrons and ions. The TEC values also depend on season, with the highest and lowest values happening near equinoxes (February and October) and during summer, respectively. Figure 3.7 shows TEC variations with local time, season and sunspot number at middle latitudes (as derived using GPS data).

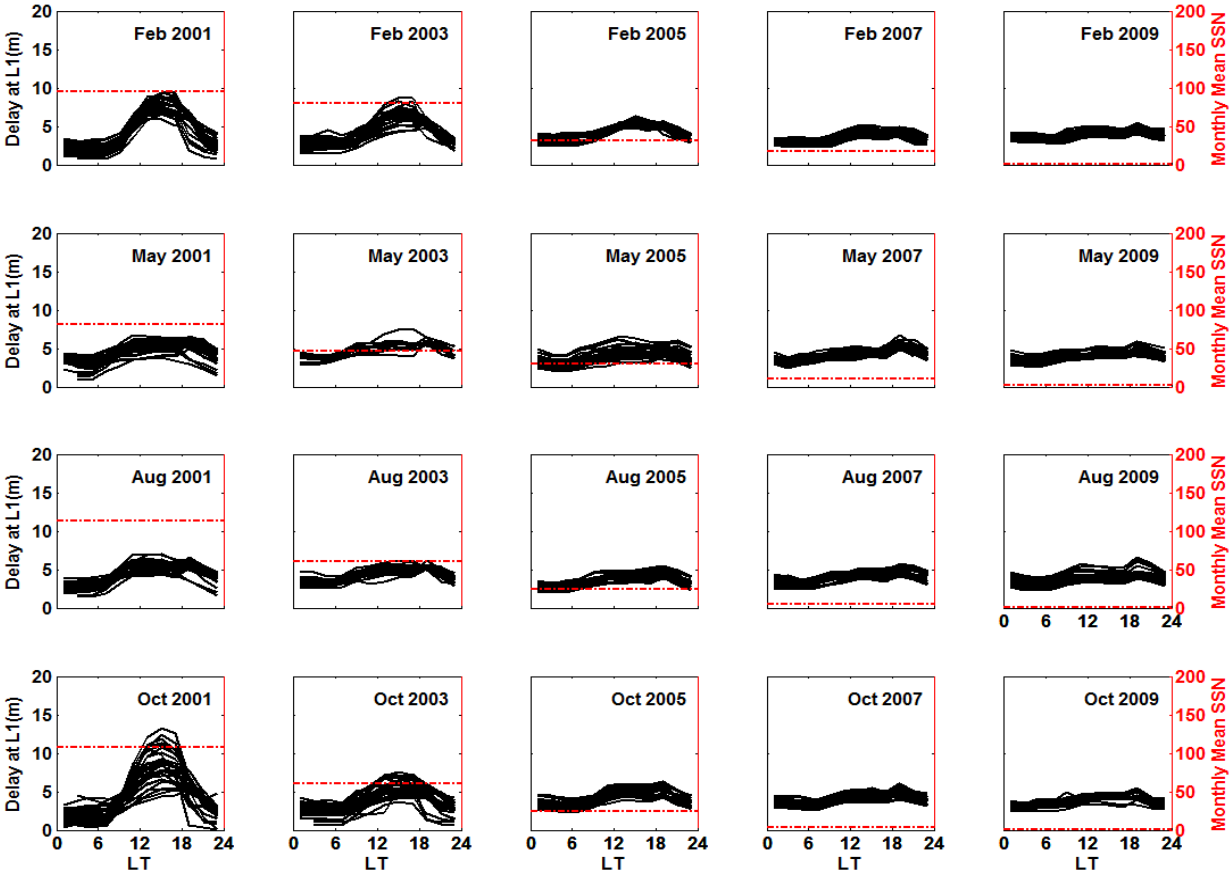

Figure 3.7: Variation in TEC with local time, season and sunspot number for middle latitudes

Figure 3.8 shows an example of how a network of GNSS receivers can be used to map the ionosphere. This map represents the global variation of TEC values. During nominal ionospheric conditions the TEC values are maximum near the equator – equatorial anomaly – and decrease with increasing latitude.

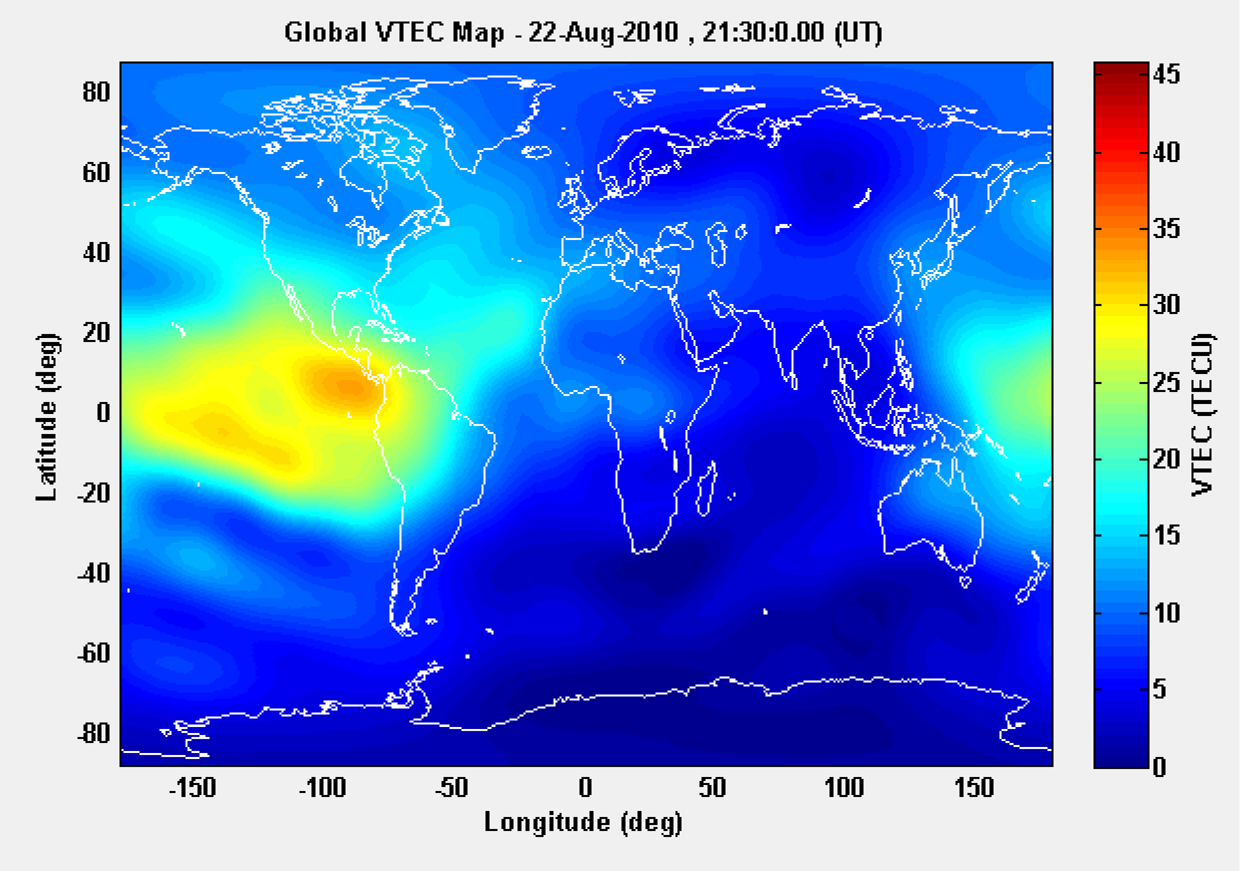

Figure 3.8: Global Ionospheric Map (GIM) (data courtesy of CODE)

During geomagnetically disturbed periods, the electrons in the ionosphere may increase especially near the mid-to-high latitudes and an enhancement of ionospheric TEC occurs. These electrons are carried from lower latitudes to high latitudes forming a plume of enhanced TEC. This phenomenon is referred to as Storm Enhanced Density (SED). SED was first identified in the early 1990's with the Millstone incoherent scatter radar (Foster, 1993) and has been observed and reported over North America (Coster and Skone, 2009) and Europe (Coster et al., 2007). An example of an SED event is shown in Figure 3.9. The SED develops in the afternoon local time and can persist over several hours. This feature is characterized with very large TEC gradients near the edges of the plume, where a sharp increase or drop in TEC values is observed within a short period of time. Gradients as large as 70 parts per million (ppm) have been observed at the edges of the narrow SED plume in North America (Foster, 2000). This is of significance especially to DGPS and WADGPS users. These large gradients translate into differential range errors which in turn propagate into differential positioning errors. DGPS positioning errors of 20 m or more have been observed and quantified in North America and Europe during SED events (Skone and Coster, 2009). This can result in degradation of performance for applications which require high precision: for example real-time positioning such as commercial aviation and marine navigation.

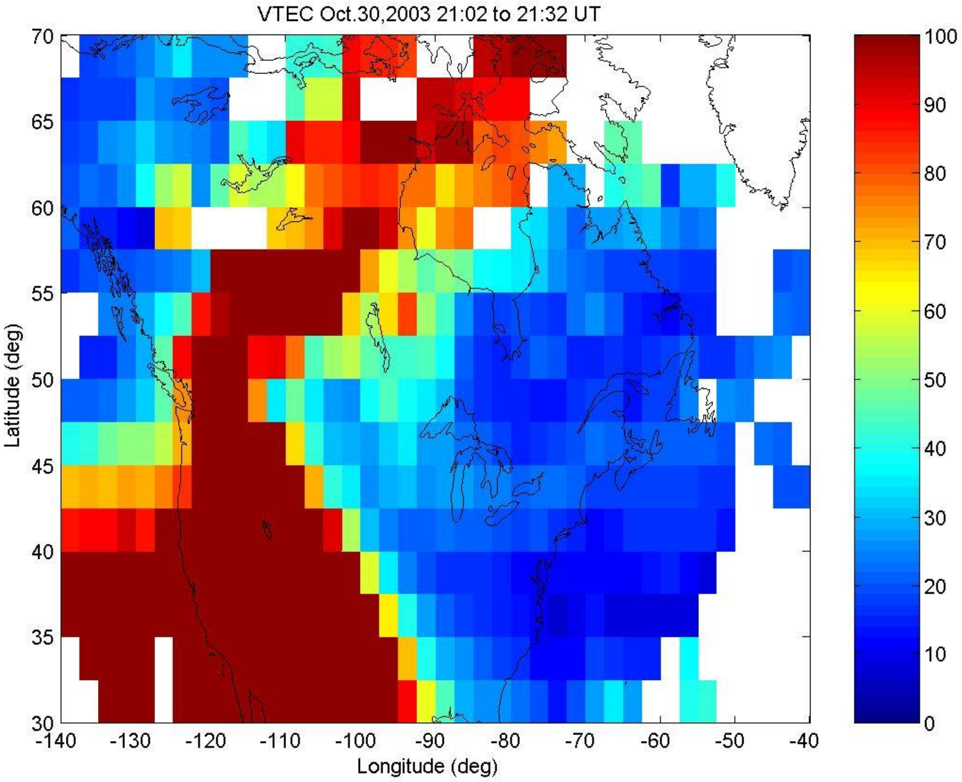

Figure 3.9: An example of SED over Canadian latitudes during a geomagnetic storm event on 30 October 2003 between 21:02 and 21:32 UT

Chapter Four: Ionospheric Tomography

4.1 Introduction

Tomography is defined as cross-sectional imaging of an object from either transmitted or reflected data collected by illuminating the object from many different directions and orientations. This method has been used in medicine, geophysics, biology and many other sciences. It consists of reconstruction of an image from the integrals of that image in multiple directions. Ionospheric tomography was first proposed by Austen et al. (1986), and it has received a lot of attention in the past two decades due to its capabilities of monitoring and detecting irregularities in the ionosphere. Further improvements were performed and different methodologies were implemented by many authors (Mitchell and Spencer, 2003; Raymund et al., 1993).

4.2 Tomography Problem

The following example illustrates the tomography problem. For simplicity, a two-dimensional projection is shown in Figure 4.1, where four homogeneous blocks with sides of unit length and assigned parameters are intersected by six ray paths. Each measurement is simply the integration of the assigned parameters along the measurement path from the transmitter to the receiver. Approximating integration with a summation, the measurement can be considered as the sum of the path lengths in each pixel multiplied by the unknown parameter in the pixel. The problem of tomography is to determine the unknown parameter (such as electron density) from the set of path-integrated measurements (such as STEC).

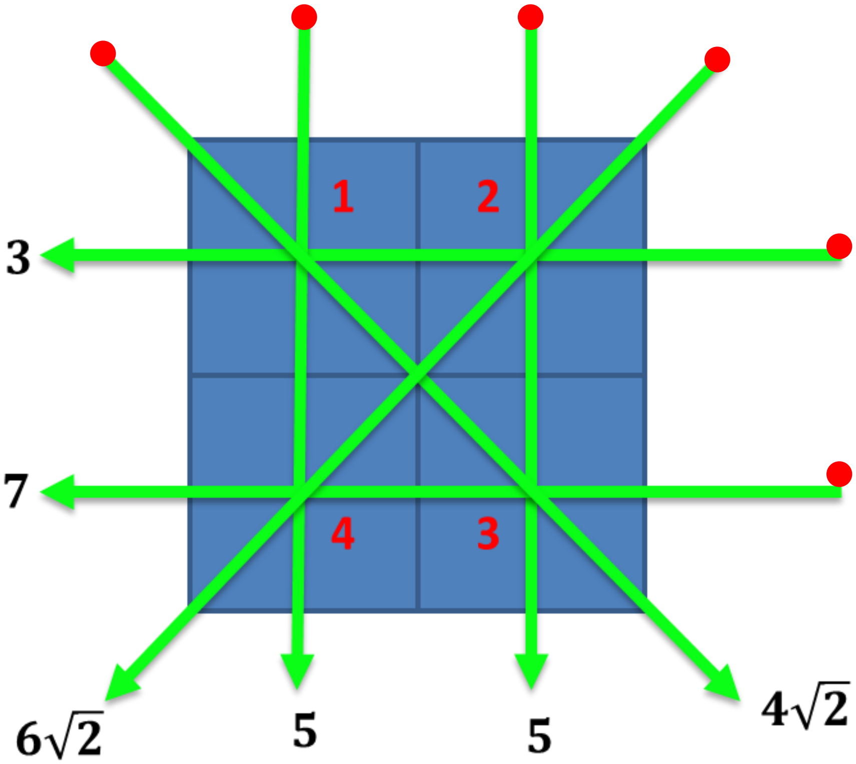

Figure 4.1: A simple tomography example

For this example the system of equations is formed as:

$$x_1 + x_2 = 3$$

$$x_3 + x_4 = 7$$

$$x_1 + x_4 = 5$$

$$x_2 + x_3 = 5$$

$$\sqrt{2}x_2 + \sqrt{2}x_4 = 6\sqrt{2}$$

$$\sqrt{2}x_1 + \sqrt{2}x_3 = 4\sqrt{2}$$

Expressing the system in a matrix form:

$$Ax = \begin{bmatrix} 1 & 1 & 0 & 0 \\ 0 & 0 & 1 & 1 \\ 1 & 0 & 0 & 1 \\ 0 & 1 & 1 & 0 \\ 0 & \sqrt{2} & 0 & \sqrt{2} \\ \sqrt{2} & 0 & \sqrt{2} & 0 \end{bmatrix} \begin{bmatrix} x_1 \\ x_2 \\ x_3 \\ x_4 \end{bmatrix} = \begin{bmatrix} 3 \\ 7 \\ 5 \\ 5 \\ 6\sqrt{2} \\ 4\sqrt{2} \end{bmatrix}$$

Using any inversion technique, such as least squares, a unique solution can be computed as:

$$x = \begin{bmatrix} x_1 \\ x_2 \\ x_3 \\ x_4 \end{bmatrix} = \begin{bmatrix} 1 \\ 2 \\ 3 \\ 4 \end{bmatrix}$$

4.3 Data Geometry Effect

The previous example represents an ideal geometry for the tomography problem. An ideal geometry is the one where all the voxels are illuminated by as many rays as possible over as many angles as possible. However, this is difficult to achieve especially when using GPS alone. Ionospheric tomography using only GPS suffers from bad geometry. GPS satellites are above the ionosphere and radio waves cannot penetrate the Earth, thus limiting the angles at which the receivers can scan the ionosphere, resulting in no rays paths running horizontally through the ionosphere. Figure 4.2 shows an example similar to the previous one but without any horizontal rays, which resembles the case of using only GPS in ionospheric tomography. The system of equations for this example is formed as:

$$x_1 + x_4 = 5$$

$$x_2 + x_3 = 5$$

$$\sqrt{2}x_2 + \sqrt{2}x_4 = 6\sqrt{2}$$

$$\sqrt{2}x_1 + \sqrt{2}x_3 = 4\sqrt{2}$$

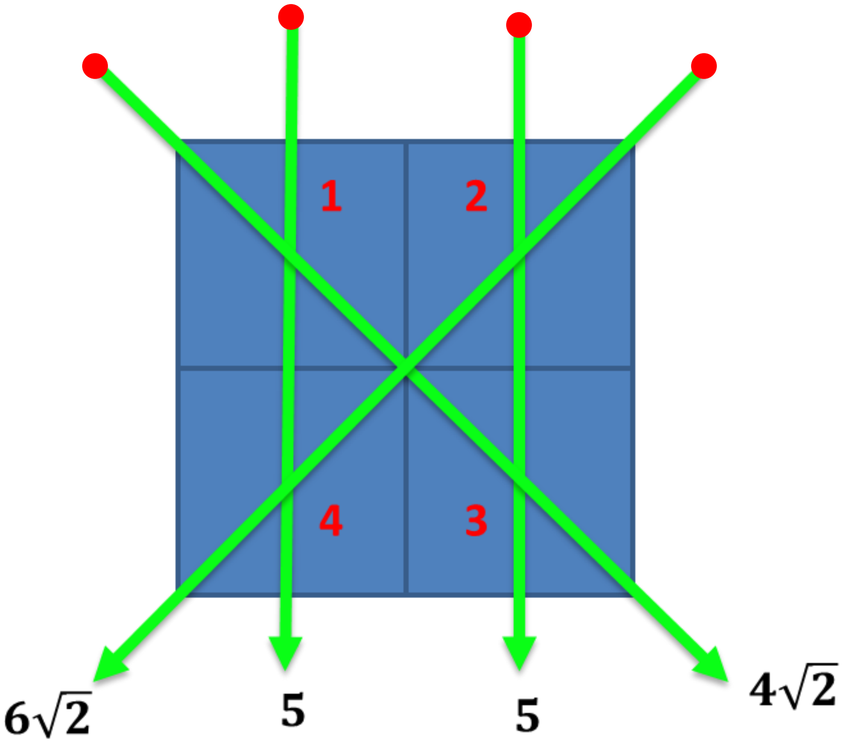

Figure 4.2: Effect of data geometry on tomography

Expressing the system in a matrix form:

$$Ax = \begin{bmatrix} 1 & 0 & 0 & 1 \\ 0 & 1 & 1 & 0 \\ 0 & \sqrt{2} & 0 & \sqrt{2} \\ \sqrt{2} & 0 & \sqrt{2} & 0 \end{bmatrix} \begin{bmatrix} x_1 \\ x_2 \\ x_3 \\ x_4 \end{bmatrix} = \begin{bmatrix} 5 \\ 5 \\ 6\sqrt{2} \\ 4\sqrt{2} \end{bmatrix}$$

Although all pixels (voxels in two dimensions) are illuminated by two ray paths, this problem has an infinite number of solutions (determinant of matrix A = 0). $x = [2, 3, 2, 3]^T$ and $x = [1.5, 2.5, 2.5, 3.5]^T$ are two possible solutions that satisfy the above system of equations. In addition to these solutions, there can be found an infinite number of possible solutions. This example shows the effect of non-ideal data geometry on the existence and uniqueness of the solution. This problem is intensified when the model is extended to three dimensions. Therefore, a different approach is required to minimize the effect of bad data geometry on the uniqueness and existence of the solution, especially in the case of using only GPS measurements. The following section summarizes the development of ionospheric tomography to overcome the effect of bad data geometry and solve the ionospheric problem and highlights some of the technique's limitations.

4.4 Overview of Ionospheric Tomography Development

Ionospheric imaging was first applied in two dimensions. Iterative techniques were the first choice to be used to solve the ionospheric tomography problem due to their simplicity and low memory requirement. Austen et al. (1986) presented the theory of Computerized Ionospheric Tomography (CIT) and the application of Algebraic Reconstruction Technique (ART) to the problem of ionospheric imaging. Afraimovich et al. (1992) and Pryse and Kersley (1992) reported results of ionospheric tomography using Simultaneous Iterative Reconstruction Technique (SIRT). Raymund et al. (1993) applied Multiplicative Algebraic Reconstruction Technique (MART) algorithm to a Scandinavian campaign in September 1991. All their results showed that iterative techniques could retrieve the electron distribution given a good initial guess. However, some concerns and limitations were identified: noise and initial guess.

Noise and initial guess affect the reconstruction significantly. A proper choice of relaxation parameter can reduce the effect of noise but affect the number of iterations required. Austen et al. (1986) showed that the number of iterations increased as the relaxation parameter was reduced. Also, choosing an initial guess is important in iterative technique. A good guess compensates for the incomplete information in the measurements. Therefore, a good initial guess (known as a background ionosphere) has been introduced and used in iterative techniques. Raymund et al. (1993) used a two-step procedure, where the background ionosphere was reconstructed first using IRI-90 then used as the initial guess to MART technique.

To overcome the limitations of iterative techniques, stochastic inversion techniques were used and applied by many authors (Fremouw et al., 1992). Because of the limited number of measurements and poor geometry of the ionospheric tomography problem, many approaches were developed to compensate for the missing information and singularity of the design matrix. Bhuyan et al. (2002) presented and discussed the development of a new algorithm based on Generalized Singular Value Decomposition (GSVD). Meggs et al. (2004) implemented the so-called full inversion method and compared it to a single shell grid model. Results showed that for mid- to high-latitudes the inversion method was better than the single shell or at least similar to it in some cases. Bhuyan et al (2004) extended the investigation of applying GSVD and regularizing (imposing additional information or constraints to solve ill-posed problems) the ionospheric tomography problem. The effect of geometry was investigated by increasing the number of sampling rays within the same latitude range. As a result, the solution gave a very good reconstructed image with poor reconstruction only near the edges of the image. Also, results showed that when irregularities are present the first order regularization is optimum and higher order methods had a much stronger smoothing effect which tends to hide important features of the image during highly disturbed ionospheric conditions. This is due to the fact that the first order regularization is a differencing (averaging) operator. The second order is the derivative of the differencing operator, which results in smoother values. Therefore, the higher the order is, the strongest the smoothing effect.

It should be mentioned that early results were based on real and/or simulated data of the Navy Navigation Satellite System (NNSS). Having these satellites in Low-Earth Orbits (LEOs), the ionosphere was often considered temporally static during a satellite pass and only two-dimensional images (altitude vs. latitude) of the ionosphere were produced since the ground receivers of NNSS were often installed along a fixed longitude chain cross section. With such LEO TEC data, only regional images could be produced with a low number of passes per day to a receiver array. Therefore, two-dimensional LEO tomography is limited both spatially and temporally. On the other hand, the development of GPS offered a new source of TEC data, especially after Selective Availability (SA) was turned off in May 2000. First experimental results using GPS data in ionospheric tomography were demonstrated in Rius et al. (1997) . This work was the first step to advance from the conventional 2-D imaging into 3-D ionospheric tomography using GPS.

Three dimensional imaging is based on the same observations as two dimensional imaging but is more complex in parameter estimation. The data are sparse and the data geometry is often not ideal. Therefore, iterative techniques are not the best choice since they do not incorporate any information from the surrounding voxels to the voxel with no measurement intersection. As a result a new method has been proposed to overcome such limitations. The method compensates for the missing ionospheric information in many voxels by adding physically reasonable constraints representing a realistic ionosphere. This can be achieved using orthonormal basis functions derived from empirical ionospheric models such as PIM and IRI. The idea of constraining the electron density profile using Empirical Orthogonal Functions (EOF) was taken from Fremouw et al. (1992) and adopted by many authors in their models with some modifications (Erturk et al., 2009; Liu and Gao, 2004; Mitchell and Spencer, 2003; Schmidt, 2007; and many others).

All of the above methods considered the ionosphere temporally static. This assumption is an approximation of reality as the ionosphere is a highly variable medium. Therefore, it is important to accommodate the temporal changes in the images. Several authors (Mitchell and Spencer, 2003; Rius et al., 1997; Schmidt, 2007) extended the model to accommodate temporal changes in the images. Mitchell and Spencer (2003) used simulated ground-GPS data from actual measurement geometry over Europe and inverted TEC data to evaluate the underlying distribution and time evolution of the electron concentration. Results showed an accurate representation (no worse than 1 TECU error) of the zonal and meridional gradients and slight underestimation of vertical TEC on the order of 1 percent.

The extension of ionospheric imaging from two dimensions into three and four dimensions (time being the fourth dimension) has been implemented. IDA3D (Bust et al., 2004) and MIDAS (Mitchell and Spencer, 2003) are examples of such implementation. MIDAS is a linear inversion tomographic technique that uses orthogonal functions to constrain the electron density profile and spherical harmonics to describe the electron density profile horizontally. However, a high order and degree of spherical harmonics are required to recover the spatial resolution of electron density over a wide area. This will lead to some difficulties inverting the problem, especially in areas with limited GPS stations as in the Canadian polar region.

As will be shown later, when the electron density field wavelength decreases, a higher order and degree of spherical harmonics are required to represent the field. Using higher order and degree leads to a larger number of unknowns which, in turn, makes the numerical cost expensive and the problem more susceptible to round-off errors (especially given that ionospheric tomography is nearly singular and ill-conditioned). Also, having a larger number of coefficients makes broadcasting them to single-frequency GPS users and using them in near real time difficult. The computational load associated with this number at the user end is significant. Therefore, a more suitable functional representation of the electron density over the Canadian polar region is required. This representation should be able to describe the minimum representable wavelength with a lower number of coefficients (unknowns) than those used in other techniques. Potentially, these coefficients can be broadcast to single-frequency GPS users to apply any necessary ionospheric corrections. The following sections describe the development of the model starting from the observation to the functional representation of the electron density profile in three dimensions.

4.5 Extracting Ionospheric Information from GPS Observables

In an ionospheric context, the electron density $\mathrm{N_e}$ corresponds to the cross-sectional image. To reconstruct that image, integrals of the image in different directions and orientations are needed. According to Equation (3.11), STEC is the integral of the electron density along the satellite-receiver Line-of-Sight (LOS). Once the transmitter and receiver coordinates are known, STEC is used to reconstruct $\mathrm{N_e}$ using tomography. In cases where GPS is used, STEC can be derived using dual frequency GPS observations.

4.5.1 STEC Observation

The “geometry-free” linear combination of GPS observations is used to derive the STEC observable. The geometric range, clock-offsets and tropospheric delay are frequency independent and can be eliminated using this combination. The “geometry-free” linear combinations for pseudorange and carrier phase observations are given as (Kleusberg and Teunissen, 1998):

$$\mathrm{P_4 = P_1 - P_2 = I_1 - I_2 + b_r^P + b_s^P + \varepsilon_{12}^P} \tag{4.1}$$

$$\Phi_4 = \Phi_1 - \Phi_2 = \mathrm{I_2 - I_1} + \lambda_1 \mathrm{N_1} - \lambda_2 \mathrm{N_2} + \mathrm{b_r^{\Phi}} + \mathrm{b_s^{\Phi}} + \varepsilon_{12}^{\Phi} \tag{4.2}$$

where

$\mathrm{I_1}$, $\mathrm{I_2}$	are ionospheric delays on L1 and L2 pseudoranges (m)
λ_1 , λ_2	are the carrier wavelengths ($\lambda_2 = 19$ cm , $\lambda_2 = 24.4$ cm)

N_1 , N_2	are the carrier phase ambiguities
$b_r^P = \left(1 - \frac{f_1^2}{f_2^2}\right) cT_{GD,r}^P$	is the receiver code-delay Inter-Frequency Bias (IFB) (m)
$b_s^P = -\left(1 - \frac{f_1^2}{f_2^2}\right) cT_{GD,s}^P$	is the satellite code-delay IFB (m)
$b_r^\Phi = -\left(1 - \frac{f_1^2}{f_2^2}\right) cT_{GD,r}^\Phi$	is the receiver IFB (m)
$b_s^\Phi = -\left(1 - \frac{f_1^2}{f_2^2}\right) cT_{GD,s}^\Phi$	is the satellite IFB (m)
$\varepsilon_{12}^P = \sqrt{(\varepsilon_1^P)^2 + (\varepsilon_2^P)^2}$	is the combination of multipath and measurement noise on P_1 and P_2 (m)
$\varepsilon_{12}^\Phi = \sqrt{(\varepsilon_1^\Phi)^2 + (\varepsilon_2^\Phi)^2}$	is the combination of multipath and measurement noise on Φ_1 and Φ_2(m)

Substituting Equation (3.12) in Equation (4.1),

$$P_4 = 40.3 \left(\frac{f_2^2 - f_1^2}{f_1^2 f_2^2}\right) STEC + b_r^P + b_s^P + \varepsilon_{12}^P \tag{4.3}$$

and rearranging Equation (4.3), the relative STEC can be derived as

$$STEC_P = \frac{P_4}{\beta} = STEC + B_r^P + B_s^P + \varepsilon_{P4} \tag{4.4}$$

where

$B_r^P = \frac{b_r^P}{\beta}$	is the receiver code-delay IFB in TECU
$B_s^P = \frac{b_s^P}{\beta}$	is the satellite code-delay IFB in TECU
$\varepsilon_{P4} = \frac{\varepsilon_{12}^P}{\beta}$	is the combination of multipath and measurement noise on P_1 and P_2 in TECU

$$\beta = 40.3\left(\frac{f_2^2 - f_1^2}{f_1^2 f_2^2}\right)$$

The relative STEC can be derived from the phase measurements using the same approach:

$$\mathrm{STEC}_\Phi = \frac{\Phi_4}{\beta} = -\mathrm{STEC} + N_{arc} + B_r^\Phi + B_s^\Phi + \varepsilon_{\Phi 4} \qquad (4.5)$$

where

$B_r^\Phi = \frac{b_r^\Phi}{\beta}$	is the receiver IFB in TECU
$B_s^\Phi = \frac{b_s^\Phi}{\beta}$	is the satellite IFB in TECU
$\varepsilon_{\Phi 4} = \frac{\varepsilon_{12}^\Phi}{\beta}$	is the combination of multipath and measurement noise on L_1 and L_2 in TECU
$N_{arc} = \frac{\lambda_1 N_1}{\beta} - \frac{\lambda_2 N_2}{\beta}$	is the bias in the ionospheric observable due to carrier phase ambiguities on L_1 and L_2

$$\beta = 40.3\left(\frac{f_2^2 - f_1^2}{f_1^2 f_2^2}\right)$$

4.5.2 STEC Smoothing

Pseudorange measurements are subject to high noise and multipath effects. As a result, the code-derived $\mathrm{STEC_P}$ observation is noisy. The multipath effect can be mitigated using an RF-absorbing ground plane or choke-ring at the antenna. The effect can also be reduced in the receiver where advanced receiver technologies have been developed and implemented (Misra and Enge, 2006). To reduce the multipath and noise level in the $\mathrm{STEC_P}$ observables, the carrier phase measurements are used to compute a more precise relative STEC observable. Although the carrier-phase derived STEC_Φ observables are more precise than the code-derived STEC_P, they are ambiguous due to the presence of integer phase ambiguities in the carrier phase measurements. To take advantage of the low-noise carrier phase derived STEC_Φ and unambiguous nature of the code-derived STEC_P, both measurements are combined and STEC is smoothed using the "levelling" process (Ciraolo et al., 2007). In this approach, the continuous arcs of STEC_Φ are adjusted to the mean value of the corresponding code STEC_P value. The mean value is computed for every continuous arc using:

$$\langle \mathrm{STEC}_\mathrm{P} + \mathrm{STEC}_\Phi \rangle = \frac{1}{\mathrm{N}} \sum_{\mathrm{i}=1}^{\mathrm{N}} (\mathrm{STEC}_\mathrm{P} + \mathrm{STEC}_\Phi) \tag{4.6}$$

where N is the number of continuous measurements contained in the arc and $\langle . \rangle$ denotes the mean value. Assuming constant IFBs and substituting Equations (4.4) and (4.5) in Equation (4.6):

$$\langle \mathrm{STEC}_\mathrm{P} + \mathrm{STEC}_\Phi \rangle = (\mathrm{B}_\mathrm{r}^\mathrm{P} + \mathrm{B}_\mathrm{s}^\mathrm{P} + \mathrm{B}_\mathrm{r}^\Phi + \mathrm{B}_\mathrm{s}^\Phi) + \frac{1}{\mathrm{N}} \sum_{\mathrm{i}=1}^{\mathrm{N}} (\mathrm{N}_\mathrm{arc} + \varepsilon_{\mathrm{P4}}) \tag{4.7}$$

The noise and multipath levels on the geometry-free combination derived from carrier phase measurements $(\varepsilon_{\Phi 4})$ are much smaller than those derived from pseudorange measurements $(\varepsilon_{\mathrm{P4}})$. Therefore, the noise and multipath term for the carrier phase $(\varepsilon_{\Phi 4})$ has been neglected in Equation (4.7). Subtracting Equation (4.5) from (4.7), the ambiguity terms can be eliminated and the smoothed STEC can be derived:

$$\begin{aligned} \mathrm{STEC}_\mathrm{smoothed} &= \langle \mathrm{STEC}_\mathrm{P} + \mathrm{STEC}_\Phi \rangle - \mathrm{STEC}_\Phi \\ &= \mathrm{STEC} + (\mathrm{B}_\mathrm{r}^\mathrm{P} + \mathrm{B}_\mathrm{s}^\mathrm{P}) + \varepsilon_{\mathrm{P4}} \end{aligned} \tag{4.8}$$

Figure 4.3 illustrates the STEC smoothing algorithm for PRN 7 using Equation (4.8). It can be seen that STEC_P contains larger noise than STEC_Φ.

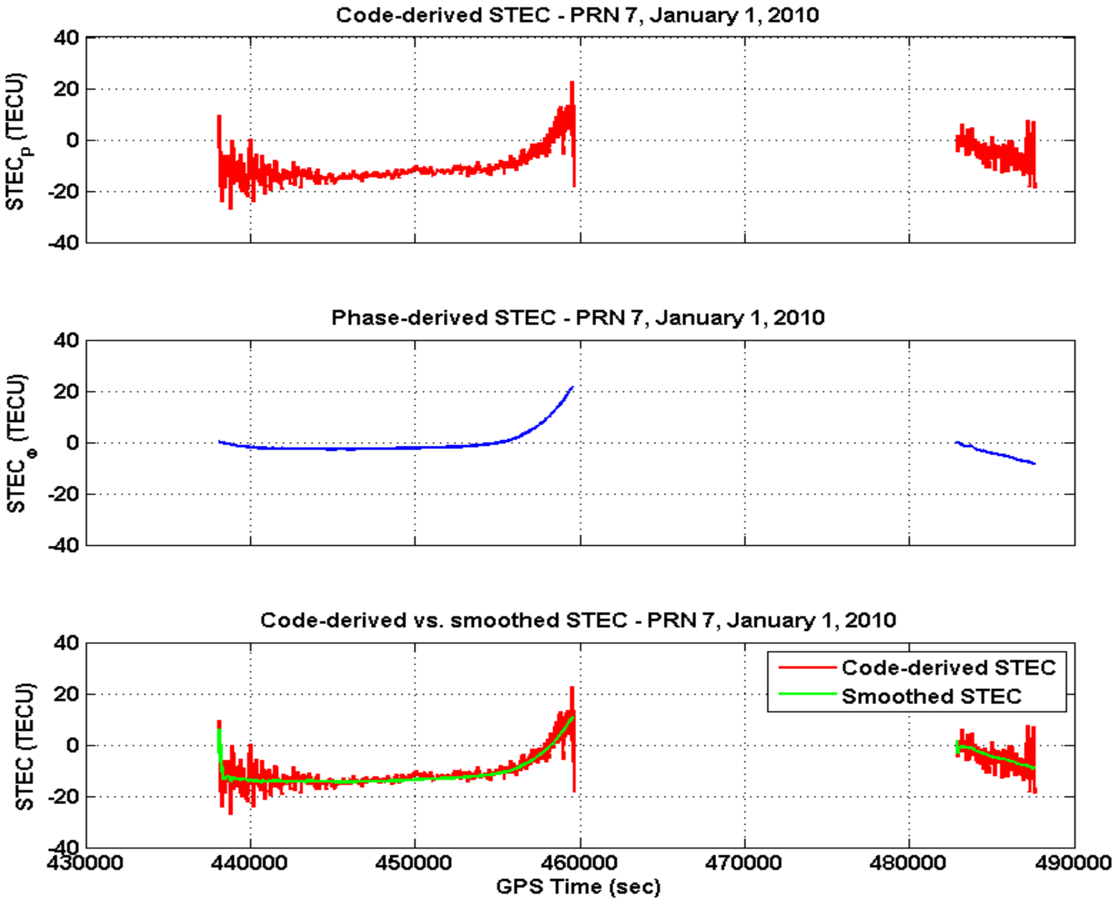

Figure 4.3: Comparison of code-derived ($STEC_P$), phase-derived ($STEC_\Phi$) and smoothed STEC ($STEC_{smoothed}$) calculated along the slant signal path of GPS satellite 7 observed from ALGO on January 1, 2010.

Equation (4.8) assumes that the carrier phase ambiguity terms N_1 and N_2 remain constant throughout the observation period. In other words, the carrier phase observations should not be affected by cycle slips, i.e., discontinuity of an integer number of cycles in the carrier phase observations. Therefore, cycle slip detection must be performed for every epoch and cycle slips corrected when possible. In case a detected cycle slip could not be corrected, the smoothing algorithm must be reinitialized.

4.5.3 Cycle Slip Detection

The receiver carrier phase tracking loop records two components: integer component and fractional component. When a GPS receiver is tracking a signal, the integer component is initialized to an arbitrary integer number of cycles (i.e. carrier phase ambiguity) and the receiver keeps track of the number of full cycles afterward. Adding the full number of cycles to the fractional component, a carrier phase measurement is formed and reported. If the receiver loses phase lock, the integer component is reinitialized causing a sudden jump in the carrier phase observable by an integer number of cycles, known as cycle slip. Occurrence of cycle slips does not affect the fractional component of the carrier phase. Cycle slips result from a temporary loss of lock in the carrier tracking loop of a GPS receiver, due to obstructions of the satellite signal caused by trees, buildings…etc., degraded signal to noise (SNR) due to low elevation observations and active ionospheric conditions, multipath and higher receiver dynamics. Cycle slips may occur between two epochs or may last several minutes or more, and their magnitude may range from few cycles to millions of cycles (Seeber, 2003).

In order to derive continuous series of smoothed STEC using Equation (4.8), cycle slips in the carrier phase measurement used to derive STEC_{Φ} must be detected and corrected, if possible. In this research, two methods are used to detect cycle slips: wide lane and geometry-free detection criteria (Sharma et al., 2011).

The wide lane phase combination is formed as follows:

$$\phi_{\mathrm{WL}} = \phi_1 - \phi_2 \text{ (cycles)} \tag{4.9}$$

where the wide lane wavelength is

$$\lambda_{WL} = \frac{c}{f_1 - f_2} = \frac{\lambda_1 \lambda_2}{\lambda_2 - \lambda_1} = 86.19 \text{ cm} \quad (4.10)$$

In order to eliminate the common non-dispersive delays and ionospheric terms, the narrow lane pseudorange combination is used:

$$P_{NL} = \frac{f_1 P_1 + f_2 P_2}{f_1 + f_2} \text{ (metres)} \quad (4.11)$$

and the widelane ambiguity terms is isolated as follows:

$$N_{WL} = \phi_{WL} - \frac{P_{NL}}{\lambda_{WL}} \text{ (cycles)} \quad (4.12)$$

Equation (4.12) is highly affected by the multipath and noise propagated through P_{NL} combination, which makes the cycle slip more difficult to detect especially under large multipath. A cycle slip is detected if the following condition is satisfied

$$|N_{WLi} - \langle N_{WL} \rangle_{i-1}| > F \times \sigma_{i-1} \quad (4.13)$$

where $\langle . \rangle$ denotes the mean value, and

$$\langle N_{WL} \rangle_i = \langle N_{WL} \rangle_{i-1} + \frac{1}{i}(N_{WLi} - \langle N_{WL} \rangle_{i-1}) \quad (4.14)$$

$$\sigma_i^2 \quad = \sigma_{i-1}^2 + \{(N_{WLi} - \langle N_{WL} \rangle_{i-1})^2 - \sigma_{i-1}^2\} \quad (4.15)$$

F is an arbitrary threshold factor that depends on assumed magnitudes of multipath and receiver noise. The lower the threshold is, the more sensitive the detection method is, and therefore this value must be chosen carefully. Optimal threshold factors F range from 4 to 6.

The wide lane cycle slip detection method is based on the assumption that there are no identical cycle slips occurring on L1 and L2 simultaneously. In such cases, an alternative criterion, the geometry-free detection criterion, is used, where Equations (4.1) and (4.2) are used and the geometry-free bias is formed:

$$\mathrm{B_{GF}} = \mathrm{P_4} + \Phi_4(\mathrm{metres}) \tag{4.16}$$

$\mathrm{B_{GF}}$ is expected to remain constant over time in the absence of a cycle slip. However, this bias is corrupted by multipath and noise, and the same algorithm used for the wide line combination is adopted:

$$|\mathrm{B_{GFi}} - \langle \mathrm{B_{GF}} \rangle_{\mathrm{i-1}}| > F \times \sigma_{\mathrm{i-1}} \tag{4.17}$$

where

$$\langle \mathrm{B_{GF}} \rangle_{\mathrm{i}} = \langle \mathrm{B_{GF}} \rangle_{\mathrm{i-1}} + \frac{1}{\mathrm{i}} (\mathrm{B_{GFi}} - \langle \mathrm{B_{GF}} \rangle_{\mathrm{i-1}}) \tag{4.18}$$

$$\sigma_{\mathrm{i}}^2 \qquad = \sigma_{\mathrm{i-1}}^2 + \{(\mathrm{B_{GFi}} - \langle \mathrm{B_{GF}} \rangle_{\mathrm{i-1}})^2 - \sigma_{\mathrm{i-1}}^2\} \tag{4.19}$$

4.6 Model Development

The following subsections describe the development of the CIT technique proposed to reconstruct the electron density over the Canadian polar region.

4.6.1 Voxel-Based Model

Figure 4.4 shows the geometry involved in ionospheric tomography. GPS satellites orbit at an altitude of ~20,200 km, which is above the ionosphere. As these satellites transmit high frequency electromagnetic radio waves, GPS receivers located on the Earth's surface collect observations that are affected by the ionosphere. Working with high frequency radio waves, bending due to the ionosphere is considered negligible and the signal path from the satellite to the receiver is assumed to be a straight line.

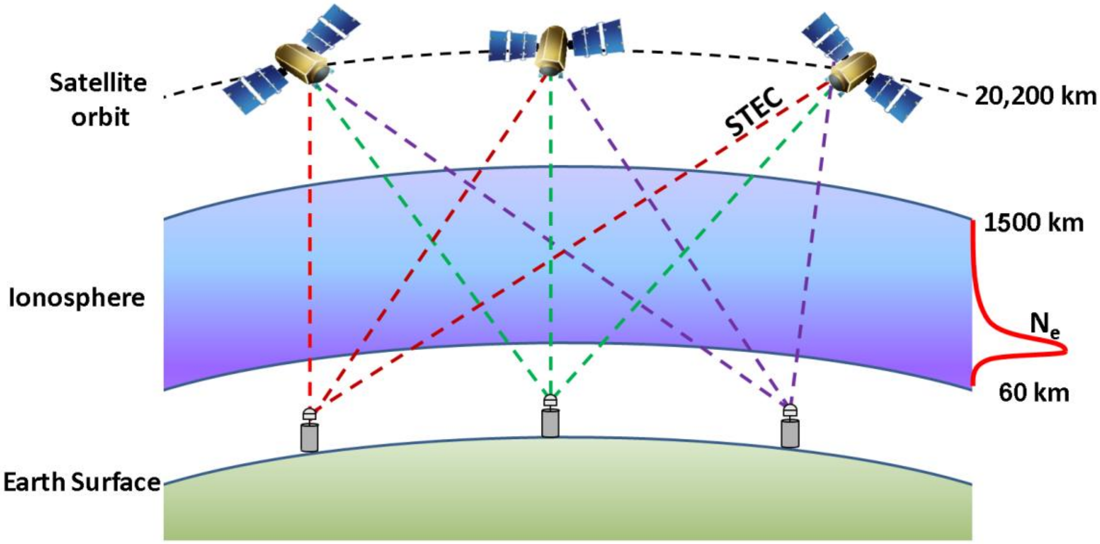

Figure 4.4: Geometry involved in ionospheric tomography

A common way of discretizing Equation (3.11) in a tomographic problem is as uniform voxels. In this approach, the atmosphere is divided into equally-sized voxels, with the electron density assumed to be homogeneous within each cell (see Figure 4.5). Assuming a three-dimensional grid, STEC can be expressed as follows:

$$\mathrm{STEC} = \sum_{i=1}^{N_\lambda} \sum_{j=1}^{N_\phi} \sum_{k=1}^{N_h} \mathrm{Ne}_{i,j,k} \,.\, \Delta h_{i,j,k} .\, \delta(i,j,k) \qquad (4.20)$$

and

$$\delta(i,j,k) = \begin{cases} 1 & \text{if voxel illuminated by a ray} \\ 0 & \text{otherwise} \end{cases} \qquad (4.21)$$

where $\Delta h_{i,j,k}$ is the ray path length illuminating voxel i, j, k and N_λ , N_ϕ ,and N_h are the number of voxels in the longitude, latitude and height directions respectively and $\mathrm{Ne}_{i,j,k}$ represents the electron density in voxel $\mathrm{i, j, k}$. A detailed description of this method is outlined in (Austen et al., 1988). Equation (4.20) can be expressed as:

$$\overrightarrow{\mathbf{STEC}} = \mathbf{H}.\ \overrightarrow{\mathbf{N_e}} + \vec{\boldsymbol{\varepsilon}} \tag{4.22}$$

where $\mathbf{H}$ is the design matrix, $\overrightarrow{\mathbf{N_e}}$ is the vector of the electron density to be estimated, and $\vec{\boldsymbol{\varepsilon}}$ is the measurement noise vector. The values of the design matrix $\mathbf{H}$ are the lengths of the ray paths within the individual voxels.

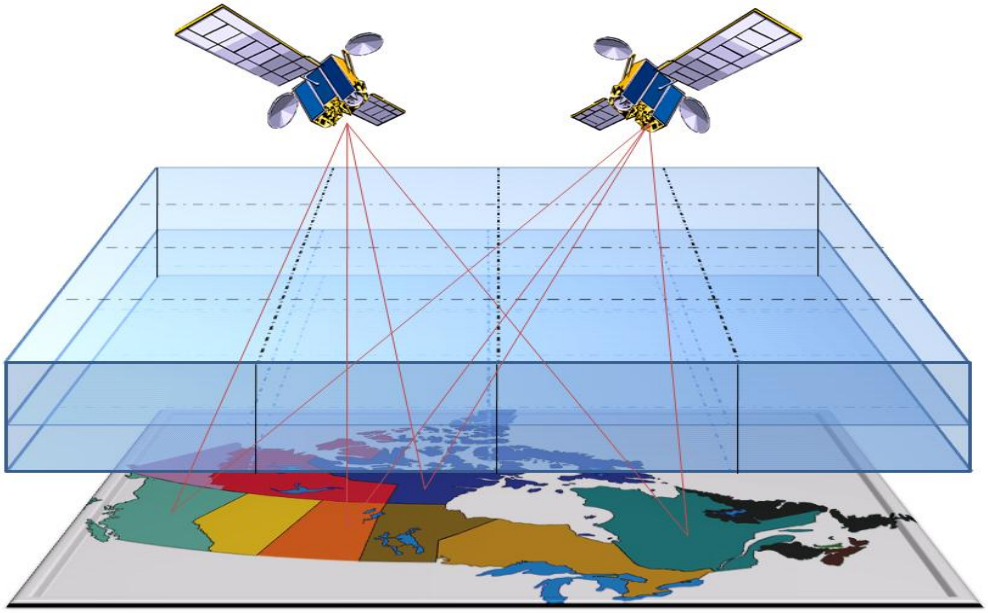

Figure 4.5: Schematic of voxel-modeled electron distribution over a GPS network

It is already shown that the smoothed ionosphere measurements are corrupted by the satellite $(\mathrm{B_s})$ and receiver $(\mathrm{B_r})$ inter-frequency biases and which need to be estimated along with the ionospheric delay parameters. Therefore, Equation (4.22) is rewritten as follows:

$$\overrightarrow{\mathbf{STEC}} = \mathbf{H}.\ \overrightarrow{\mathbf{N_e}} + \overrightarrow{\mathbf{B_s}} + \overrightarrow{\mathbf{B_r}} + \vec{\boldsymbol{\varepsilon}} \tag{4.23}$$

Equation (4.23) cannot be solved directly using ordinary stochastic techniques because the observation geometry is not ideal and the design matrix $\mathbf{H}$ is nearly singular and incorporates no prior information to the solution. To overcome this problem, a reduction of unknowns is required. This can be done by eliminating the biases using the relative changes of STEC along continuous satellite-receiver LOS. Thus, taking a certain reference measurement, usually the first, within an arc, the design matrix $\mathbf{H}$ and the measurement vector $\overrightarrow{\mathbf{STEC}}$ are differenced with respect to the reference measurement. As a result, the ionospheric tomography problem can be expressed as follows:

$$\overrightarrow{\boldsymbol{\Delta STEC}} = \Delta \mathrm{H} \cdot \overrightarrow{\mathbf{N_e}} + \vec{\boldsymbol{\varepsilon}} \tag{4.24}$$

However, the design matrix $\mathbf{\Delta H}$ in Equation (4.24) is underdetermined and ill-conditioned; therefore, a straight solution of this inversion problem must be done in a different way. Transformation of the problem to another space can be applied to overcome this problem, where the unknowns are coefficients of three-dimensional orthonormal basis functions (Mitchell and Spencer, 2003). The mapping matrix used in this transformation is generated using a spherical harmonic expansion and EOF to represent the horizontal and vertical variation in electron concentration, respectively, allowing a certain range of possible solutions. A priori information is needed to generate the mapping function. However, the choice of the vertical profile set to form the basis functions is a critical factor in the accuracy of the solution. Results presented in (Mitchell and Spencer, 2003) showed an underestimation of TEC due to the limited number of EOFs used in the inversion.

4.6.1.1 Design of 3-D Voxel-Based Model

The values of $\Delta h_{i,j,k}$ and $\delta(\mathrm{i,j,k})$ of Equation (4.20) are required to construct the design matrix **H** used in the voxel-based model. These values are computed using the following procedure:

- Form the equation of LOS from the satellite to the receiver.
- Find the equations of each side (6 sides) of each voxel.
- Find points of intersection of LOS with each side of each voxel:
  - If the LOS illuminates voxel $\mathrm{i,j,k}$, then $\delta(\mathrm{i,j,k})$ is set to 1 and two points of intersection exist, or 0 otherwise.
  - Once $\delta(\mathrm{i,j,k})$ is set to 1, $\Delta \mathrm{h}_{\mathrm{i,j,k}}$ is computed as the distance between the two points of intersection.

Starting with the first step, given the satellite coordinates P_1 and the station coordinates P_o, the LOS equation is formed as follows:

$$Line: \vec{P} = \overrightarrow{P_o} + t \times \left(\overrightarrow{P_1} - \overrightarrow{P_o}\right) \text{ where scalar t } \in [\,0\,,1\,] \tag{4.25}$$

Figure 4.6 shows the definition of the voxel sides and its representation with respect to the Earth's surface. The top and bottom sides are parallel to the Earth's surface, which is described by a sphere. The equation describing the spherical surface at each height is governed by:

$$\mathrm{x}^2 + \mathrm{y}^2 + \mathrm{z}^2 = (\mathrm{R_E} + \mathrm{height}\,)^2 \tag{4.26}$$

where $\mathrm{R_E}$ is the Earth's radius. The North and South sides are described by a conic surface, according to:

$$(\mathrm{x}^2 + \mathrm{y}^2)\tan^2 \phi = \mathrm{z}^2 \tag{4.27}$$

where ϕ is the latitude. Finally, the East and West sides are parallel to two great circles passing through the two longitudes that define the voxel boundaries along the longitudinal direction. The relationship between the x and y coordinates is described by:

$$\tan(\lambda) = \frac{x}{y} \tag{4.28}$$

Substituting Equation (4.25) in the equation of each side and solving for the value of (t), the point of intersection of the LOS with each side, if it exists, is computed by substituting (t) in Equation (4.25).

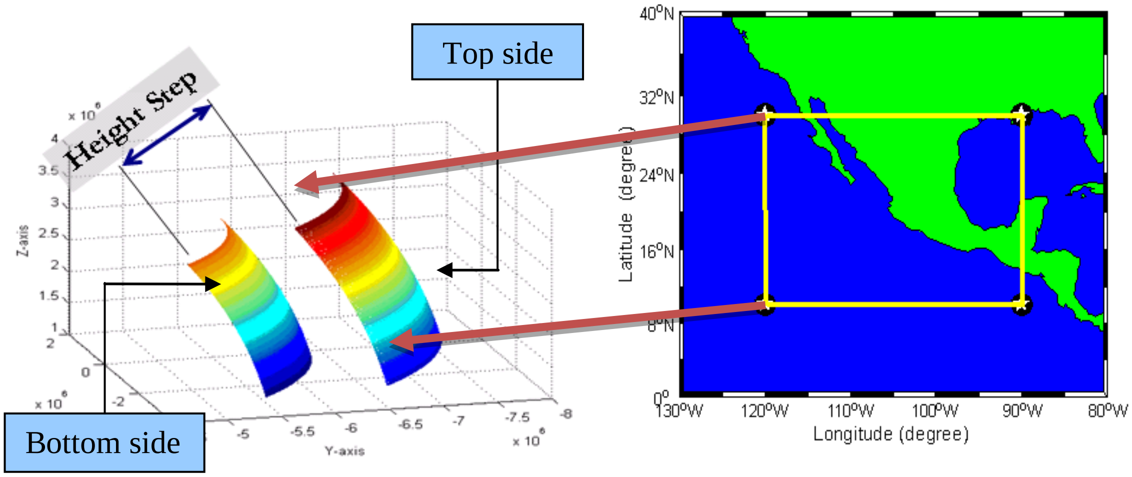

(a) voxel top and bottom sides

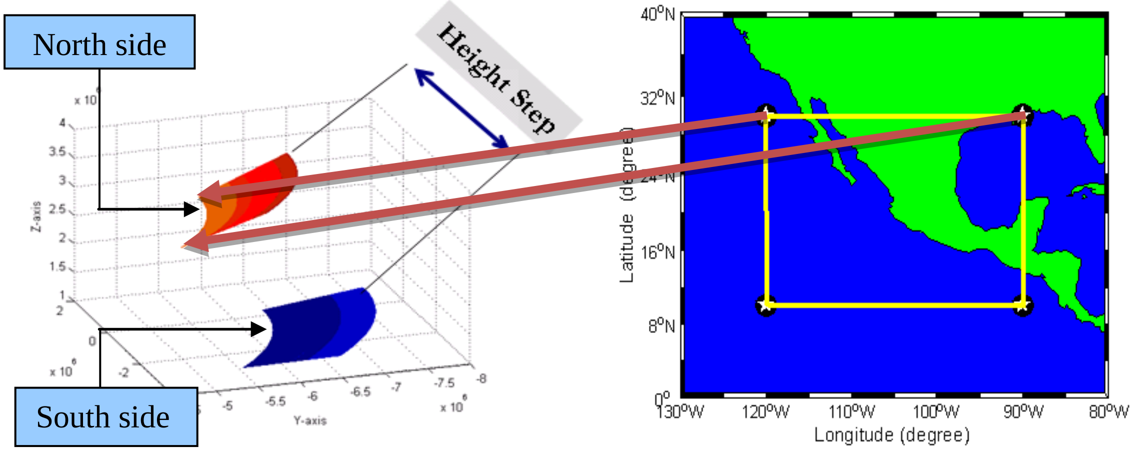

(b) voxel front and back sides

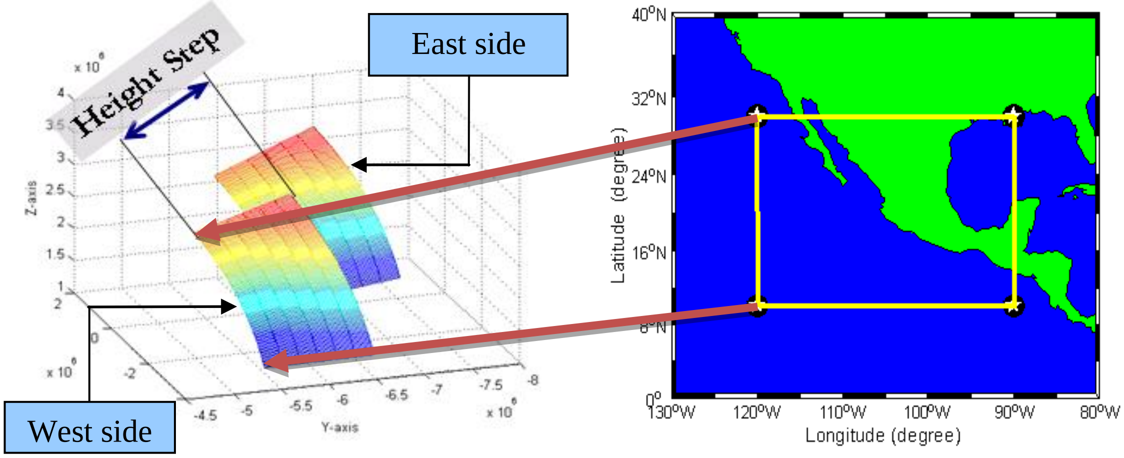

(c) voxel left and right sides

Figure 4.6: Voxel sides definition

All observations included in the voxel-based model must lie within the defined model space, where the LOS associated with each observation must enter the grid from the bottom of the lowest layer and exit through the top of the highest layer. Figure 4.7 shows the rejection criteria applied in this model. For example, the LOS of observation $STEC_5$ enters the space model through the lowest layer but exits from the right side of voxel 4. Also, the LOS associated with STEC 6 does not lie within the grid space model; therefore it is rejected and is not included in the inversion.

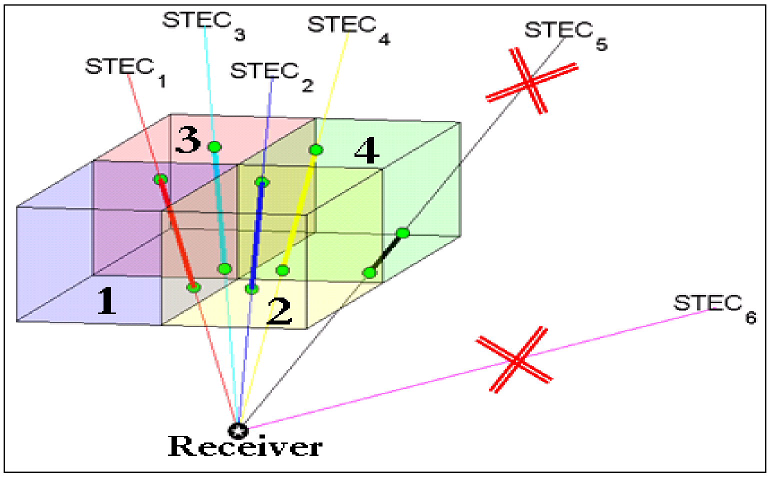

Figure 4.7: Observation rejection criteria

4.6.2 Spherical Cap Harmonics (SCH)

A general function $f(\lambda,\theta)$ of colatitude θ and longitude λ defined over a sphere can be represented as an expansion of spherical harmonics:

$$f(\lambda,\theta) = \sum_{n=0}^{K}\sum_{m=0}^{n}[a_n^m \cos(m\lambda) + b_n^m \sin(m\lambda)]P_n^m(\cos\theta) \qquad (4.29)$$

where $P_n^m(\cos\theta)$ is the Legendre polynomial of integer order m and degree n and a_n^m and b_n^m are the global coefficients that characterize the expansion. The terms $P_n^m(\cos\theta)\sin(m\lambda)$ and $P_n^m(\cos\theta)\cos(m\lambda)$ are called the ordinary surface spherical harmonics.

For applications with data limited to a region of the Earth, i.e. spherical cap, the Legendre polynomials and trigonometric functions are no longer the most appropriate basis functions for fitting a general function over the restricted area. Since the associated Legendre function $P_n^m(\cos\theta)$ (where n and m are integers) is orthogonal only over the entire sphere, another set of orthogonal functions must be used instead. Haines (1985) proposed a technique called Spherical Cap Harmonic Analysis (SCHA) to solve the problem. The technique can be used to model a general function on a cap-like region by new functions that are still Legendre functions of integer order m but non-integer degree n. The new non-integer Legendre functions and their derivatives have, alternatively, zero value at the edge of a cap with half-angle θ_o. Therefore, Legendre functions are chosen in order to satisfy the following boundary conditions (Haines, 1985):

$$\begin{aligned} &\frac{dP_{n_k}^m(\cos\theta_o)}{d\theta} = 0 && \text{for } k - m = \text{even} \\ &P_{n_k}^m(\cos\theta_o) = 0 && \text{for } k - m = \text{odd} \end{aligned} \tag{4.30}$$

where k is used to index (in ascending order) the roots of Equation (4.30) at a given value m. The value of n_k^m, once determined using the above equations, can be ordered by an index k which starts from value zero and the new expansion has the following form:

$$f(\lambda,\theta) = \sum_{k=0}^{K_{max}} \sum_{m=0}^{k} [a_k^m \cos(m\lambda) + b_k^m \sin(m\lambda)] P_{n_k}^m(\cos\theta) \tag{4.31}$$

which corresponds to a spherical expansion developed on a cap-like region in a new reference system with the North Pole at the centre of the spherical cap. K_{max} is the maximum degree at which the expansion is truncated. A great advantage of this technique is that the degree n_k has the same meaning as in Spherical Harmonics Analysis (SHA) which is the number of (minimum) representable wavelengths λ_{min} along the terrestrial circumference irrespective of whether n_k is integer or not:

$$\lambda_{min} = \frac{2\pi R_E}{n_k} \tag{4.32}$$

with R_E = 6371.2 km, the Earth's mean radius. With the number of expansion coefficients as $(K+1)^2$ for SCHA, it is easy to compute, for example, that in a spherical cap of 20° to model a field with λ_{min}= 1000 km, it would be necessary to use an expansion of 100 coefficients (with K up to 9). This can be computed using (Haines, 1985):

$$K = \left[\frac{2\pi R_E}{\lambda_{min}} + \frac{1}{2}\right]\frac{\theta_o}{90} - \frac{1}{2} \tag{4.33}$$

To obtain the same resolution in SHA (apart from possible numerical problems), a maximum degree n = 40000/1000 ≈ 40 is required and therefore $n(n+2)$ = 1680 coefficients; to represent the field by means of SCHA less than six percent of the coefficients for SHA are required. This is reasonable since there is no need for observations from outside the region itself to model the field (De Santis, 1991).

4.6.2.1 Coordinate Transformation

The first step in SCH analysis is to convert the geographic colatitudes (θ) and longitudes (λ) of the data from 'old' values in the normal geographic system to 'new' values relative to the new pole (spherical cap coordinate system). The spherical cap coordinate system is an Earth-centered coordinate system. The pole of the spherical cap is chosen to define the coordinate system. The meridian of zero longitude is defined as the great circle passing through the new North Pole and the Geographic South Pole (Antarctic pole). Figure 4.8 and Figure 4.9 illustrate the relationship between the geographic coordinate system and spherical cap coordinate system (Liu et al., 2009).

If the geographic coordinates of the new pole in the old system are θ_o and λ_o then the new coordinates (θ_c, λ_c) of any point Q (θ, λ) can be computed using the following:

$$\cos(\theta_c) = \cos(\theta_o)\cos(\theta) + \sin(\theta_o)\sin(\theta)\cos(\lambda - \lambda_o) \quad (4.34)$$

$$\tan(\pi - \lambda_c) = \frac{\sin(\theta)\sin(\lambda - \lambda_o)}{\sin(\lambda_o)\cos(\theta) - \cos(\theta_o)\sin(\theta)\cos(\lambda - \lambda_o)} \quad (4.35)$$

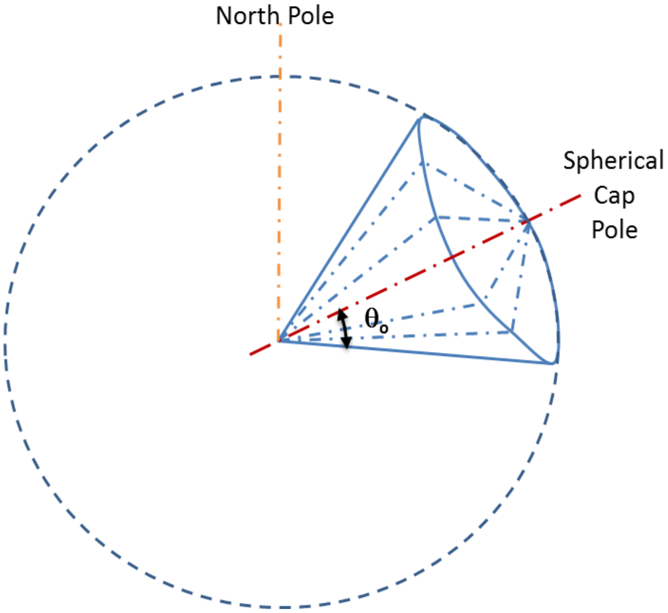

Figure 4.8: The pole of spherical cap coordinate system (after Liu et al., 2009).

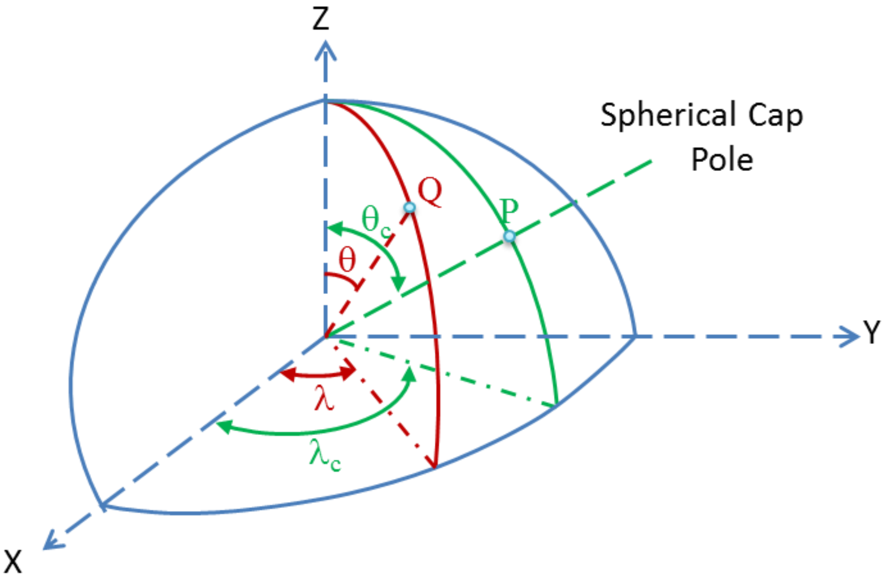

Figure 4.9: Coordinate transformation between geographic coordinate system and spherical cap coordinate system (after Liu et al., 2009).

4.6.2.2 Computation of the Associated Legendre Function $P_{n_k}^{m}(\cos\theta)$

The associated Legendre function $P_{n_k}^{m}(\cos\theta)$ can be expressed as follows:

$$P_n^m(\cos\theta) = \sum_{k=0}^{\infty} A_k(m,n)\left(\sin\frac{\theta}{2}\right)^{2k} \tag{4.36}$$

where

$$A_k(m,n) = \begin{cases} K_n^m \sin^m\theta & k = 0 \\ \dfrac{(k+m-1)(k+m)-n(n+1)}{k(k+m)} A_{k-1}(m,n) & k > 0 \end{cases} \tag{4.37}$$

and the normalizing factor K_n^m is approximated using Stirling’s formula (Haines, 1985) by:

$$K_n^m = \begin{cases} 1 & m = 0 \\ \dfrac{2^{-m}}{\sqrt{m\pi}} \left(\dfrac{n+m}{n-m}\right)^{\frac{1}{2}n+\frac{1}{4}} p^{\frac{1}{2}m} \exp(e_1 + e_2) & m > 0 \end{cases} \tag{4.38}$$

where

$$p = \left(\frac{n}{m}\right)^2 - 1$$

$$e_1 = -\frac{1}{12m}\left(1 + \frac{1}{p}\right)$$

$$e_2 = \frac{1}{360m^3}\left(1 + \frac{3}{p^2} + \frac{4}{p^3}\right)$$

From Equation (4.36) it is shown that

$$\frac{dP_n^m(\cos\theta)}{d\theta} = \frac{\sin\theta}{2}\sum_{k=1}^{\infty} kA_k(m,n)\left(\sin\frac{\theta}{2}\right)^{2(k-1)} + \cos\theta\left[\frac{m}{\sin\theta}P_n^m(\cos\theta)\right] \tag{4.39}$$

where the second term on the right hand side is set to zero when $m = 0$. In order to calculate the roots n_k^m, Equation (4.30) must hold. Using Equation (4.36) and Equation (4.39), the values of n_k^m can be solved numerically. The values of n_k^m up to $k = 5$ for $\theta_o = 24°$ are given in Table 4.1.

Table 4.1: Non-integer degrees n_k^m for half-angle θ_o = 24°

	m					
k	**0**	**1**	**2**	**3**	**4**	**5**
0	**0**					
1	**5.234**	**3.978**				
2	**8.661**	**8.661**	**6.918**			
3	12.675	12.252	11.812	9.711		
4	**16.256**	**16.256**	**15.561**	**14.829**	**12.435**	
5	**20.157**	**19.894**	**19.626**	**18.722**	**17.763**	**15.118**

Figure 4.10 illustrates the associated Legendre functions $P_n^m(\cos\theta)$ for a spherical cap of half-angle $\theta_o = 24°$, for $k = 5$, $m = 0,1,\ldots 5$. It is clear that the functions with $k - m =$ "odd" are zero at the boundary of the cap and the conditions in Equation (4.30) are satisfied.

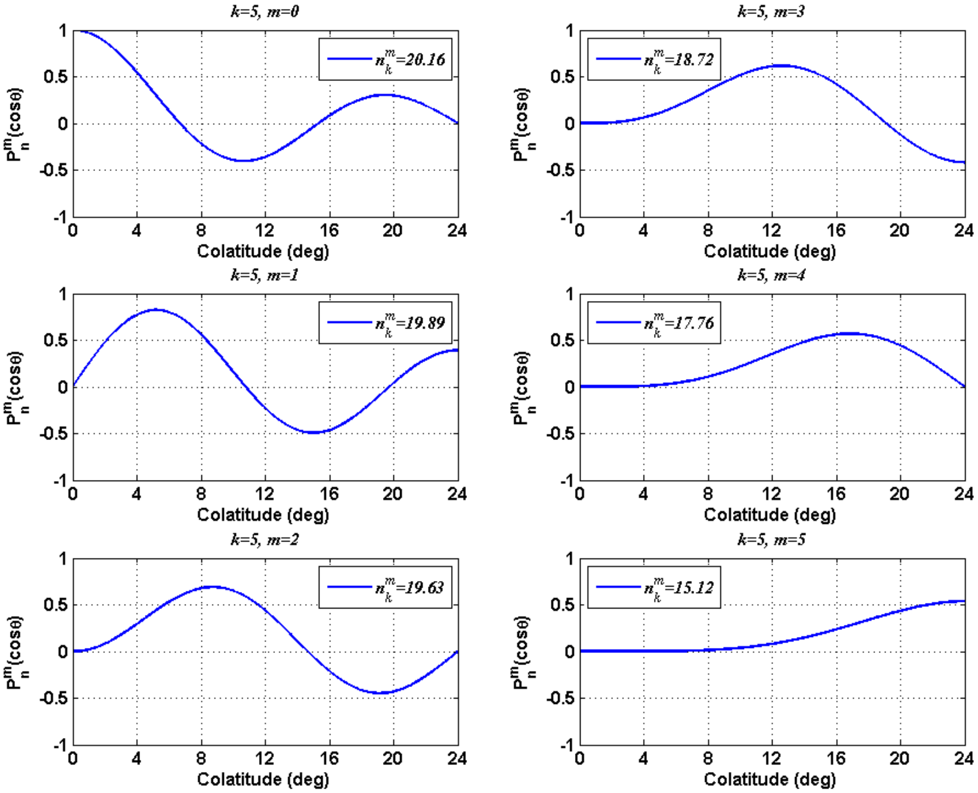

Figure 4.10: Associated Legendre functions for a spherical cap of half-angle $\theta_o = 24°$, for $k = 5, m = 0, 1, \ldots 5$

4.6.3 Empirical Orthogonal Functions (EOF)

The vertical resolution of the ionospheric tomographic problem is poor. Therefore, a priori information is used to form the vertical basis functions that span the entire space in the vertical direction. This is accomplished using Empirical Orthogonal Function (EOF). EOF analysis is a powerful tool for data analysis and reduction of data dimensions. These functions are widely used in meteorology. EOFs are derived from empirical data of the ionospheric electron density, such as the International Reference Ionosphere (IRI) model. Using such functions, the vertical profiles of electron density are obtained. Given the date, time and location of GPS measurements, the ionospheric electron density profile $N_e(\lambda, \phi, h, t)$ can be obtained from the IRI-2007 model (Bilitza and Reinisch, 2008) and specific EOFs can be tailored for different geophysical conditions. In this way, the electron density profiles are limited to a certain range of possible solutions. The electron density profile data matrix G ($M \times N$ matrix) can be arranged as:

$$G_{M\times N} = \begin{bmatrix} N_e(\lambda_1, \phi_1, h_1, t_1) & N_e(\lambda_1, \phi_1, h_1, t_2) & \dots & N_e(\lambda_1, \phi_1, h_1, t_N) \\ N_e(\lambda_1, \phi_1, h_2, t_1) & N_e(\lambda_1, \phi_1, h_2, t_2) & & N_e(\lambda_1, \phi_1, h_2, t_N) \\ \vdots & \vdots & \ddots & \vdots \\ N_e(\lambda_i, \phi_j, h_k, t_1) & N_e(\lambda_i, \phi_j, h_k, t_2) & \cdots & N_e(\lambda_i, \phi_j, h_k, t_N) \end{bmatrix} \quad (4.40)$$

where $M = i \times j \times k$ is the number of voxels, and N is the number of times series. To obtain the required EOFs, Singular Value Decomposition (SVD) can be used:

$$G_{M\times N} = U_{M\times M} S_{M\times N}\, V^T_{N\times N} \quad (4.41)$$

where **U** and **V** are orthogonal matrices with columns that span the data and model spaces respectively, and **S** is a diagonal matrix:

$$S_{M\times N} = \mathrm{diag}(s_1, s_2, \dots, s_M) \quad (4.42)$$

where the singular values along the diagonal of S are customarily arranged in decreasing order:

$$s_1 \geq s_2 \geq \cdots \geq s_M \geq 0 \quad (4.43)$$

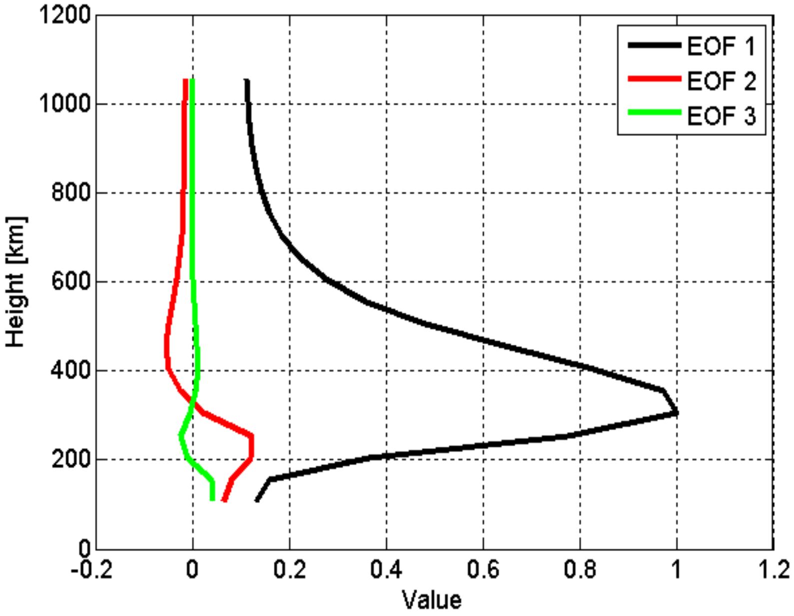

Figure 4.11: First three EOFs derived from IRI-2007 model

Figure 4.11 shows the first 3 EOFs extracted from electron density profiles obtained from IRI-2007 model for July 3rd, 2000. Although the columns of **U** form a basis that constrains the model vertically, only a subset that corresponds to the significant singular values (s) is sufficient. The first EOF describes the mean of the electron density profile. However, a variation of the mean profile is required to offer more possible profiles that can fit the model. Using a low number of EOF (such as one) will limit the solution vertically to the mean value represented by the first EOF. Including higher number of EOF's leads to a higher number of possible combinations (profiles) that constrain the model vertically.

This is important especially around the maximum electron density peak (~300 km altitude) where the profile can deviate from the mean. In order to determine the number of EOFs, i.e. number of **U** columns, to be used in the model, a further investigation is conducted and the results are shown in Chapter 5.

Combining spherical cap harmonic functions and the EOFs, the electron density distribution $\mathrm{N_e}(\lambda, \phi, \mathrm{h})$ can be expressed as follows:

$$\mathrm{N_e}(\lambda, \phi, \mathrm{h}) = \sum_{q=1}^{Q} \sum_{k=0}^{K_{max}} \sum_{m=0}^{k} \left[a_{kq}^{m} \cos(m\lambda) + b_{kq}^{m} \sin(m\lambda)\right] P_{n_k}^{m}(\cos\theta)\, Z_q(\lambda, \phi, h) \tag{4.44}$$

where $Z_q(\lambda, \phi, h)$ represents the empirical orthogonal function, Q is the order of EOFs, a_{kq}^{m} and b_{kq}^{m} are the tomography model coefficients that characterize the field of the ionosphere and the unknowns to be estimated in the model. Based on Equation (4.44), the number of unknowns is:

$$\text{Number of coefficients} = Q \times (K_{max} + 1)^2 \tag{4.45}$$

Equation (4.44) is expressed in a matrix form as:

$$\overrightarrow{\mathbf{N_e}} = \mathbf{B}.\vec{\mathbf{m}} \tag{4.46}$$

where **B** contains the basis functions generated using EOFs and SCH expansion, and **m** contains the tomography model coefficients. Substituting Equation (4.46) in Equation (4.24), the ionospheric tomography problem can be expressed as follows:

$$\overrightarrow{\boldsymbol{\Delta STEC}} = \mathbf{G} \cdot \vec{\mathbf{m}} + \vec{\boldsymbol{\varepsilon}} \tag{4.47}$$

where

$$\mathbf{G} = \Delta \mathrm{H} \cdot \mathbf{B} \tag{4.48}$$

4.7 Weighted Least Squares

In Equation(4.47), the change in STEC is expressed as a linear system of the form:

$$\vec{\mathbf{d}} = \mathbf{G} \cdot \vec{\mathbf{m}} \tag{4.49}$$

where $\mathbf{G}$ is defined in Equation (4.48), $\vec{\mathbf{d}}$ are the change in the observed STECs, and $\vec{\mathbf{m}}$ is the vector of the tomography model coefficients to be estimated. To solve this system of equations, the method of least squares is used. This method finds the vector $\vec{\mathbf{m}}$ which minimizes the sum of the squares of the errors made in solving every equation. In other words, the least squares method minimizes the 2-norm of the residuals. The residual is defined as the difference between the observation and its expected value. In a vector form, the residual vector $\vec{\mathbf{v}}$ is defined by:

$$\vec{\mathbf{v}} = \left(\vec{\mathbf{d}} - \mathbf{G} \cdot \vec{\mathbf{m}}\right) \tag{4.50}$$

However, any *a priori* information about the accuracy of the observation must be taken into account when solving Equation (4.49). As a result, the weighted least squares solution satisfies the following (Bjõrck, 1996):

$$\mathbf{min}\left(\|\vec{\mathbf{v}}\|_{\mathbf{P}}^{\mathbf{2}}\right) = \mathbf{min}(\vec{\mathbf{v}}^{\mathbf{T}}\mathbf{P}_{\mathbf{d}}\vec{\mathbf{v}}) \tag{4.51}$$

and the weighted least squares solution can be expressed as follows:

$$\hat{\mathbf{m}} = \overrightarrow{\mathbf{m_0}} + (\mathbf{G}^{\mathbf{T}}\mathbf{P}_{\mathbf{d}}\mathbf{G})^{-1}\mathbf{G}^{\mathbf{T}}\mathbf{P}_{\mathbf{d}}\left(\vec{\mathbf{d}} - \mathbf{G} \cdot \overrightarrow{\mathbf{m_0}}\right) \qquad \text{given} \qquad \mathbf{P}_{\mathbf{d}} = \sigma_0^2\mathbf{C}_{\mathbf{l}}^{-\mathbf{1}} \tag{4.52}$$

where $\overrightarrow{\mathbf{m_0}}$ is the initial parameter estimates, σ_0^2 is the *a priori* variance, and $\boldsymbol{C_l}$ is the measurement variance-covariance matrix. The variance-covariance matrix of the estimated parameters is given by

$$\mathbf{C}_{\hat{\mathbf{x}}} = \hat{\sigma}^2(\mathbf{G}^{\mathbf{T}}\mathbf{P}_{\mathbf{d}}\mathbf{G})^{-1} \tag{4.53}$$

where $\hat{\sigma}^2$ is the *a postoriori* variance of unit weight which is computed by

$$\widehat{\sigma}^2 = \frac{\vec{\mathbf{v}}^{\mathbf{T}}\mathbf{P_d}\vec{\mathbf{v}}}{\mathrm{n-u}} \tag{4.54}$$

where n is the number of observations and u is the number of unknowns .

4.8 Generalized Tikhonov Regularization

The design matrix **G** in Equation (4.48) is nearly singular (large condition number with respect to singular values). It is difficult to invert it without round-off errors affecting the solution and even causing it to converge to the wrong solution. Therefore, ionospheric tomography is part of the family of inverse problems. The ionospheric tomography inverse problem is often ill-posed, which is characterized by instability, non-uniqueness and even non-existence of the solution. Therefore, ordinary inversion techniques (i.e. ordinary least squares) are not efficient and special inversion techniques must be considered in ionospheric tomography.

Many methods have been proposed for regularizing such a problem in order to achieve reasonable estimates. Generalized Tikhonov regularization is one of the most common methods for regularization that satisfies the following (Mead, 2007).

$$\mathbf{min}\left(\|\vec{\mathbf{v}}\|_{\mathbf{P_d}}^{\mathbf{2}} + \|\overrightarrow{\mathbf{v_x}}\|_{\mathbf{P_m}}^{\mathbf{2}}\right) = \mathbf{min}\left(\left\|\vec{\mathbf{d}} - \mathbf{G}\vec{\mathbf{m}}\right\|_{\mathbf{P_d}}^{\mathbf{2}} + \alpha^2\|(\widehat{\mathbf{m}} - \overrightarrow{\mathbf{m_0}})\|_{\mathbf{P_m}}^{\mathbf{2}}\right) \tag{4.55}$$

where $\mathbf{P_d}$ and $\mathbf{P_m}$ are the inverse of the variance-covariance matrix of the observations and the initial parameter estimates $\overrightarrow{\mathbf{m_0}}$, respectively**.** The regularization parameter $\alpha \geq 0$ controls the weight given to the norm of $\widehat{\mathbf{m}} - \overrightarrow{\mathbf{m_0}}$**,** relative to the minimization of the residual norm. The parameter α can be determined using a technique explained in Section 4.8.1. Setting the following

$$\begin{aligned}
\mathbf{A} &= \boldsymbol{P_d}^{\frac{1}{2}}\,\mathrm{G}\,\boldsymbol{P_m}^{-\frac{1}{2}} \\
\vec{\boldsymbol{y}} &= \boldsymbol{P_d}^{\frac{1}{2}}\left(\vec{\boldsymbol{d}} - \mathrm{G}\overrightarrow{\mathbf{m_0}}\right) \\
\hat{\mathbf{x}} &= \boldsymbol{P_m}^{\frac{1}{2}}(\widehat{\mathbf{m}} - \overrightarrow{\mathbf{m_0}})
\end{aligned} \tag{4.56}$$

Equation (4.55) is transformed to a simpler form and the minimization problem is replaced with:

$$\mathbf{min}\left(\|\mathbf{A}\hat{\mathbf{x}} - \vec{\boldsymbol{y}}\|^{\mathbf{2}} \; + \alpha^2\|\hat{\mathbf{x}}\|^{\mathbf{2}} \right) \tag{4.57}$$

Equation (4.57) can be written as

$$\mathbf{min}\left(\left\|\begin{bmatrix}\mathbf{A}\\ \alpha\mathbf{I}\end{bmatrix}\hat{\mathbf{x}} - \begin{bmatrix}\vec{\mathbf{y}}\\ \mathbf{0}\end{bmatrix}\right\|^2\right) \tag{4.58}$$

which can be solved by the method of normal equations, i.e.,

$$[\mathbf{A}^{\mathbf{T}} \quad \alpha\mathbf{I}]\begin{bmatrix}\mathbf{A}\\ \alpha\mathbf{I}\end{bmatrix}\hat{\mathbf{x}} = [\mathbf{A}^{\mathbf{T}} \quad \alpha\mathbf{I}]\begin{bmatrix}\vec{\mathbf{y}}\\ \mathbf{0}\end{bmatrix} \tag{4.59}$$

Equation (4.59) simplifies to

$$[\mathbf{A}^{\mathbf{T}}\mathbf{A} + \alpha^2\mathbf{I}]\hat{\mathbf{x}} = \mathbf{A}^{\mathbf{T}}\vec{\mathbf{y}} \tag{4.60}$$

and the solution of the minimization problem of Equation (4.57) can be written as

$$\hat{\mathbf{x}} = [\mathbf{A}^{\mathbf{T}}\mathbf{A} + \alpha^2\mathbf{I}]^{-\mathbf{1}}\mathbf{A}^{\mathbf{T}}\vec{\mathbf{y}} \tag{4.61}$$

Substituting Equation (4.56) in Equation (4.61), the generalized Tikhonov solution of Equation (4.55) can be expressed as follows:

$$\widehat{\mathbf{m}} = \overrightarrow{\mathbf{m_0}} + (\mathbf{G}^{\mathbf{T}}\mathbf{P_d}\mathbf{G} \; + \; \alpha^2\mathbf{P_m})^{-1}\mathbf{G}^{\mathbf{T}}\mathbf{P_d}\left(\vec{\mathbf{d}} \; - \; \mathbf{G}\cdot\overrightarrow{\mathbf{m_0}}\right) \tag{4.62}$$

and the variance-covariance matrix is given by:

$$\mathbf{C}_{\hat{\mathbf{x}}} = \hat{\sigma}^2(\mathbf{G}^{\mathbf{T}}\mathbf{P_d}\mathbf{G} + \alpha^2\mathbf{P_m})^{-\mathbf{1}} \tag{4.63}$$

where $\hat{\sigma}^2$ is the *a postoriori* variance of unit weight which is computed by

$$\hat{\sigma}^2 = \frac{\vec{\mathbf{v}}^{\mathbf{T}}\mathbf{P_d}\vec{\mathbf{v}} + \vec{\mathbf{v}}_{\mathbf{x}}{}^{\mathbf{T}}\mathbf{P_m}\vec{\mathbf{v}}_{\mathbf{x}}}{\mathbf{n-u}} \tag{4.64}$$

where n is the number of observation and u is the number of unknowns.

4.8.1 Regularization Parameter Selection

The choice of regularization parameter α is a key element of any Tikhonov regularized solution. If α is chosen to be too small, the solution will be dominated by noise. If α is chosen too large, the solution will be too smooth and major features of the distribution will not appear in the solution. The method of L-curve is the most common method for selecting a regularization parameter α. The L-curve is an L-shaped plot of optimal values of $\|(\hat{\mathbf{m}} - \overrightarrow{\mathbf{m_0}})\|^2$ versus $\left\|\vec{\mathbf{d}} - \mathbf{G}\vec{\mathbf{m}}\right\|^2$ on a log-log scale. The regularization parameter α is selected so that it gives the solution closest to the L-curve corner (Aster et al., 2012). Figure 4.12 shows the generic form of the L-curve. Once the optimum value α is computed, the generalized Tikhonov solution and its variance-covariance matrix are computed using Equation (4.62) and Equation (4.63), respectively.

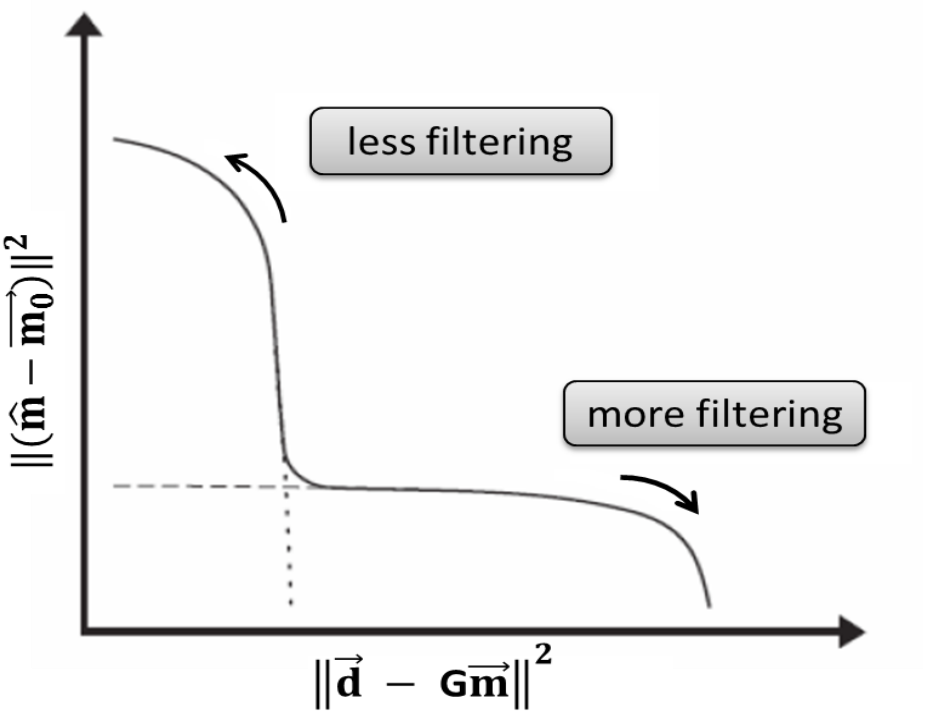

Figure 4.12: The L-curve

4.9 Advantages of Ionospheric Tomography

Three-dimensional ionospheric tomography has many advantages. Compared to two-dimensional imaging, ionospheric tomography has the capability to model the electron density with multiple layers which is an improvement over two-dimensional imaging. This is beneficial since it provides more fundamental information about the ionosphere and many ionospheric parameters can be derived from the electron density profile such as maximum peak value and height. Therefore ionospheric tomography is regarded as an important cost effective tool to monitor and study the ionosphere. (Meggs et al., 2004) and (Meggs and Mitchell, 2006) investigated the benefits gained by using three-dimensional tomography over the two-dimensional imaging over a wide geographical area. Results showed that both algorithms gave comparable results during the nighttime; however, the uncertainty in TEC determination during the daytime using two-dimensional imaging were up to three times greater than those produced by the three-dimensional ionospheric tomography.

4.10 Applications of Ionospheric Tomography

Ionospheric tomography is useful for many applications. One application is frequency selection for HF radio communication. Signals at High Frequency (HF) are reflected back to the Earth. The electron density defines the refractive path of the signals, which is important for radio frequency selection. It helps in determining the Maximum Usable Frequency (MUF) and Lowest Usable Frequency (LUF) which are important parameters for a successful communication. Ionospheric tomography can be used to recover information about the electron density distribution and aid in planning the MUF and LUF for HF radio communication. (Rogers et al., 2001) showed that ionospheric tomography can be used to help scheduling HF communications.

Range errors due to the ionosphere are the main error source in GPS positioning. Many real-time mapping systems such as WAAS monitor the ionosphere continuously and provide correction to single-frequency GPS users to compensate for such range errors. The accuracy of the ionospheric model determines the position accuracy of single-frequency users. As stated earlier, (Meggs et al., 2004) and (Meggs and Mitchell, 2006) showed that three-dimensional imaging provides more accurate TEC maps than those produced by two-dimensional imaging. Therefore, ionospheric tomography has potential application in deriving ionospheric corrections for wide area networks.

Chapter Five: Ionospheric Tomography Modelling – Simulation

5.1 Introduction

A new ionospheric tomographic technique has been developed and presented in Chapter 4. To demonstrate the feasibility of the technique, a number of simulations using the IRI model are performed. Simulations of different ionospheric conditions are used to investigate the capability of the technique to recover different ionospheric parameters such as electron density, TEC, and electron density peak value. The conditions are divided into two categories: 1) nominal ionospheric conditions, and 2) storm conditions. The first category represents typical ionospheric conditions during different phases of the solar cycle. Three periods of the solar cycle are chosen: sunspot minimum, maximum and moderate. The second category represents challenging storm conditions such as a storm enhanced density (SED) event. In this chapter, the feasibility and performance of the technique under these conditions are demonstrated and analyzed, via simulation, and a quantitative comparison of the results is conducted and discussed. The outcome of the analysis determines the most appropriate combination of $\mathrm{K}_{\mathrm{max}}$ and Q in Equation (4.44) for the Canadian polar region, where these values are adopted for the processing of real data in the Chapter 6.

5.2 Tomographic Modelling of Canadian Polar Region

The region of interest in this thesis is the polar cap, due to its importance and effect on radio propagation and communication especially during solar maximum. The polar cap region is lacking spatial resolution of TEC measurements due to the orbit limitations of spaced-based measurements and sparse networks providing such measurements. To overcome these limitations, the Canadian High Arctic Ionospheric Network (CHAIN) was designed and took advantage of Canada's most accessible landmass in the high arctic regions (Jayachandran et al., 2009). The network consists of 10 (eight within the polar cap region) high data-rate GPS ionospheric scintillation and TEC monitors and six Canadian Advanced Digital Ionosondes (CADI). Having access to such data, and applying the new Computerized Ionospheric Tomographic (CIT) technique, a clear understanding of the quality and limitations of the technique, particularly in high-latitude regions, is achieved. The importance of the implementation of the new tomographic technique allows determination of various ionospheric parameters. For example the peak height of electron density is used in monitoring and predicting HF communication capabilities for aircraft polar routes. Imaging the three-dimensional extent of ionospheric structures allows identification of gradients associated with development of ionospheric scintillations. Velocities of such polar cap patches can be estimated and evolution of scintillation regions predicted.

5.3 Simulated Data Description

Simulations are based on availability of real data in high-latitude regions. Ten GPS reference stations from the CHAIN Network are used and twenty-six International Global Navigation Satellite System (GNSS) Service (IGS) stations are selected to form the network over the Canadian polar region. The coordinates of the network stations used are listed in Table 5.1 and their geographic distribution is illustrated in Figure 5.1. All sites are equipped with dual-frequency GPS receivers. This allows the derivation of STEC at each site using the procedure presented in Chapter 4. Once the coordinates of the ground receivers and the GPS satellites are known, electron density profiles can be recovered and TEC maps can be computed using the proposed CIT technique.

Figure 5.1: The geographic distribution of the IGS and CHAIN stations based on Google Earth^{TM}.

Table 5.1: Station coordinates of the Canadian polar region network

Station	Location	Network	Geographic Lat (°N)	Geographic Lon (°E)	Geomagnetic Lat (°N)	Geomagnetic Lon (°E)	Height (m)
EURC	**Eureka (NU)**	**CHAIN**	**79.99**	**274.10**	**87.62**	**265.43**	**33.56**
RESC	**Resolute (NU)**	**CHAIN**	**74.75**	**265.00**	**82.77**	**305.51**	**80.71**
PONC	**Pond Inlet (NU)**	**CHAIN**	**72.69**	**282.04**	**82.45**	**346.82**	**63.89**
TALC	**Taloyoak (NU)**	**CHAIN**	**69.54**	**266.44**	**78.17**	**321.39**	**15.27**
CBBC	**Cambridge Bay (NU)**	**CHAIN**	**69.12**	**254.97**	**76.32**	**304.77**	**16.17**
HALC	**Hall Beach (NU)**	**CHAIN**	**68.78**	**278.74**	**78.41**	**343.46**	**7.24**
QIKI	**Qikiqtarjuaq (NU)**	**CHAIN**	**67.53**	**295.97**	**77.20**	**14.31**	**13.27**
IQAC	**Iqaluit (NU)**	**CHAIN**	**63.73**	**291.46**	**73.53**	**5.78**	**23.14**
SANC	**Sanikiluaq (NU)**	**CHAIN**	**56.54**	**280.77**	**66.25**	**350.34**	**15.64**
EDMC	**Edmonton (AB)**	**CHAIN**	**53.35**	**247.03**	**60.11**	**308.25**	**771.38**
ALBH	**Victoria (BC)**	**IGS**	**48.39**	**236.51**	**53.75**	**298.42**	**31.74**
ALGO	**Algonquin Park (ON)**	**IGS**	**45.96**	**281.93**	**55.69**	**352.75**	**200.83**
BAKE	**Baker Lake (NU)**	**IGS**	**64.32**	**264.00**	**72.86**	**323.40**	**4.41**
BREW	**Brewster (WA)**	**IGS**	**48.13**	**240.32**	**54.07**	**302.74**	**238.63**
CAGS	**Gatineau (QC)**	**IGS**	**45.59**	**284.19**	**55.36**	**355.56**	**235.02**
CHUR	**Churchill (MB)**	**IGS**	**58.76**	**265.91**	**67.58**	**329.40**	**-19.54**
CHWK	**Chilliwack (BC)**	**IGS**	**49.16**	**237.99**	**54.73**	**299.75**	**174.01**

			Geographic		Geomagnetic		
Station	**Location**	**Network**	**Lat (°N)**	**Lon (°E)**	**Lat (°N)**	**Lon (°E)**	**Height (m)**
DRAO	**Penticton (BC)**	**IGS**	**49.32**	**240.37**	**55.24**	**302.34**	**541.86**
ESCU	**Escuminac (NB)**	**IGS**	**47.07**	**295.20**	**56.76**	**9.27**	**-16.02**
FLIN	**Flon Flon (MB)**	**IGS**	**54.73**	**258.02**	**62.82**	**320.93**	**311.49**
HLFX	**Halifax (NS)**	**IGS**	**44.68**	**296.39**	**54.34**	**10.55**	**3.12**
HOLM	**Ulukhaktok (BC)**	**IGS**	**70.74**	**242.24**	**0.40**	**75.78**	**285.42**
KUUJ	**Kuujjuarapik (QC)**	**IGS**	**55.28**	**282.25**	**-0.47**	**65.02**	**352.50**
NAIN	**Nain (NL)**	**IGS**	**56.54**	**298.31**	**33.49**	**66.12**	**14.48**
NRC1	**Ottawa (ON)**	**IGS**	**45.45**	**284.38**	**82.48**	**55.22**	**355.80**
PICL	**Pickle Lake (ON)**	**IGS**	**51.48**	**269.84**	**315.10**	**60.66**	**336.85**
PRDS	**Calgary (AB)**	**IGS**	**50.87**	**245.71**	**57.51**	**307.78**	**1247.94**
RESO	**Resolute (NU)**	**IGS**	**74.69**	**265.11**	**19.92**	**82.73**	**305.96**
SASK	**Saskatoon (SK)**	**IGS**	**52.20**	**253.60**	**578.58**	**59.83**	**316.53**
SCH2	**Schefferville (QC)**	**IGS**	**54.83**	**293.17**	**498.19**	**64.58**	**7.27**
SHE2	**Shediac (NB)**	**IGS**	**46.22**	**295.45**	**-15.30**	**55.90**	**9.51**
UNBJ	**Fredericton (NB)**	**IGS**	**45.95**	**293.36**	**21.81**	**55.69**	**6.91**
VALD	**Val-d'Or (QC)**	**IGS**	**48.10**	**282.44**	**312.77**	**57.84**	**353.27**
WILL	**Williams Lake (BC)**	**IGS**	**52.24**	**237.83**	**1095.66**	**57.70**	**298.25**
WSLR	**Whistler (BC)**	**IGS**	**50.13**	**237.08**	**909.24**	**55.54**	**298.35**
YELL	**YellowKnife (NT)**	**IGS**	**62.48**	**245.52**	**180.72**	**68.71**	**300.64**

5.4 Data Analysis Strategy and Results Validation

Validating a developed model is a necessity to prove its feasibility to perform the assigned task, in this case retrieving different ionospheric parameters. However, many models can work well under nominal but not challenging conditions. To demonstrate the performance of the proposed CIT technique and establish its limitations, the model is validated under different quiet and challenging ionospheric conditions:

1. Solar minimum ionospheric condition (01 January 2009).
2. Solar moderate ionospheric condition (01 January 2004).
3. Solar maximum ionospheric condition (01 January 2000).
4. Storm enhanced density event (29-30 October 2003).

The first three dates were picked based on the solar cycle sunspot number as shown in Figure 5.2. The fourth date was picked on the date of the SED storm which was on 29-30 October 2003.

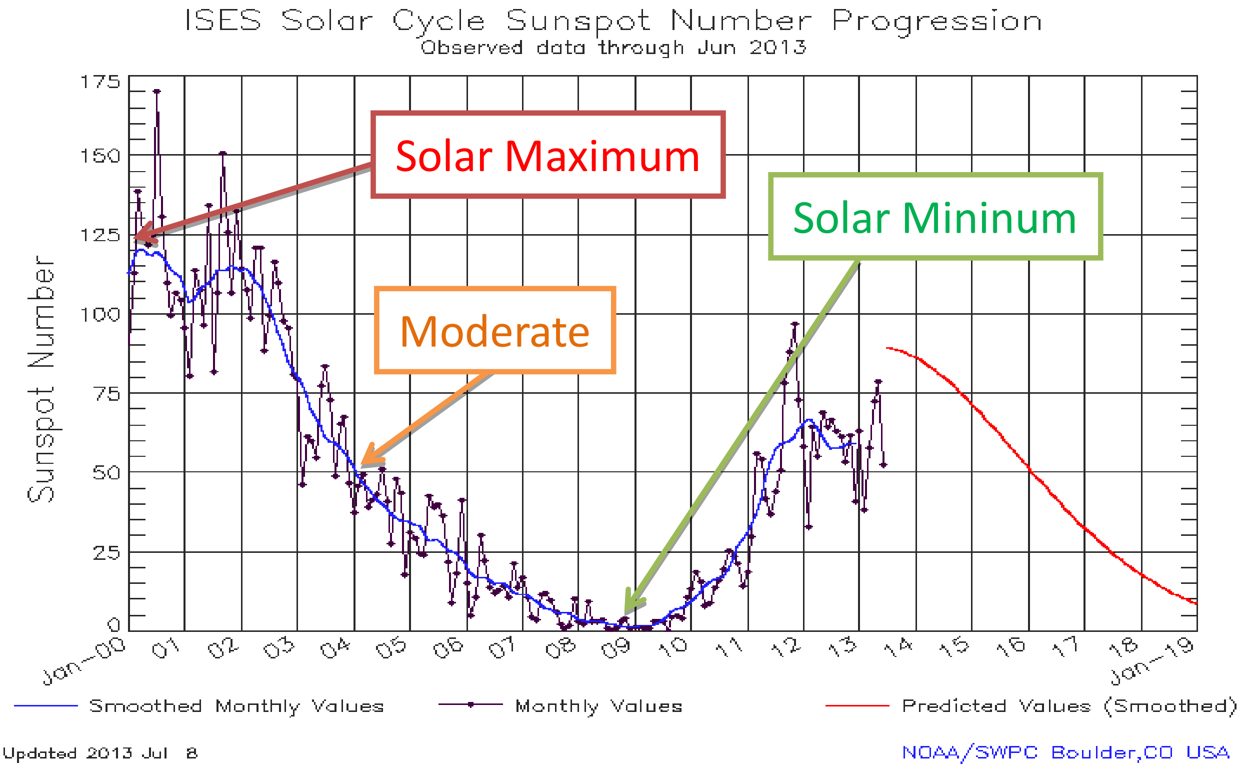

Figure 5.2: Solar Cycle Sunspot Number (http://www.swpc.noaa.gov/SolarCycle/, July 2013)

There are no standard metrics to evaluate the ionospheric tomography technique. Different authors use various metrics. For example, Arikan et al.(2007) used the normalized reconstruction error, Mitchell and Spencer (2003) used the mean absolute error, Materassi and Mitchell (2005) used the average error of the reconstructed peak height,…etc. These metrics are adopted in this work since they describe the model in three different domains (electron density, TEC and maximum peak value) which represent a more complete picture than using only TEC or electron density. Arikan et al.(2007) reported a reconstruction error of ~0.2–0.5 using different combinations of basis functions. Mitchell and Spencer (2003) reported a mean absolute error of better than 1 TECU. Materassi and Mitchell (2005) reported an average error of the reconstructed maximum peak of 2×10^{11} el/m^3. The values reported by these authors are used as a benchmark and set as performance metrics to assess the performance of the proposed CIT technique. To evaluate the performance of the proposed method, the reconstruction and the original IRI model are compared at the start of the hour, based on the aforementioned metrics. The metrics are defined using the following:

$$\mathrm{Re} = \frac{\left\| \overrightarrow{\mathbf{N_e}}^{\mathbf{Estimated}} - \overrightarrow{\mathbf{N_e}}^{\mathbf{Truth}} \right\|}{\left\| \overrightarrow{\mathbf{N_e}}^{\mathbf{Truth}} \right\|} \tag{5.1}$$

$$\mathrm{MAE} = \frac{1}{\mathrm{N}} \sum_{\mathrm{i}=1}^{\mathrm{N}} \left| \mathrm{TEC}_{\mathrm{i}}^{\mathrm{Estimated}} - \mathrm{TEC}_{\mathrm{i}}^{\mathrm{Truth}} \right| \tag{5.2}$$

$$\overline{\Delta \mathrm{N}_{\mathrm{e}_{\max}}} = \frac{1}{\mathrm{N}} \sum_{\mathrm{i}=1}^{\mathrm{N}} \left| \max\left(\mathrm{N_e}^{\mathrm{Estimated}}(\lambda, \phi, \mathrm{h}) \right) - \max\left(\mathrm{N_e}^{\mathrm{Truth}}(\lambda, \phi, \mathrm{h}) \right) \right| \tag{5.3}$$

where Re is the normalized reconstruction error, MAE is the mean absolute error in TEC, and $\overline{\Delta \mathrm{N}_{\mathrm{e}_{\max}}}$ is the average error of the reconstructed maximum peak. N in Equations (5.2) and (5.3) is the number of horizontal voxels.

5.5 Numerical Simulation

To demonstrate the capability and reliability of the method, it is necessary to validate the technique using simulated STEC observations. As stated in Chapter 4, STEC can be expressed in matrix form as:

$$\overrightarrow{\mathbf{STEC}} = \mathbf{H}.\,\overrightarrow{\mathbf{N_e}} \tag{5.4}$$

Any ionospheric model such as IRI or PIM models can be utilized to generate STEC observations using the following procedure:

I. The ionosphere is divided into equally-sized voxels based on the pre-set voxel spacing ($\Delta\phi$, $\Delta\lambda$, and Δheight)

II. For a specific time period, the electron density at the centre of each voxel is computed using an ionospheric model and assumed to be homogeneous within the voxel and constant over the period of simulation.

III. For the same time period, the actual Cartesian coordinates of GPS satellites are computed using the broadcast ephemeris of that period.

IV. Given the coordinates of the ground GPS receivers, the design matrix H in Equation (5.4) is computed (one row for each LOS).

V. The vector of simulated STEC is then computed using Equation (5.4).

VI. An independent distributed random noise with zero mean and a standard deviation of 0.1 TECU is added to the synthetic STEC measurements since the precision of the smoothed

STEC is usually better than 0.1 TECU (Skone et al., 2002). The final noisy simulated STEC observation can be expressed as:

$$\overrightarrow{\mathbf{STEC}}_{\boldsymbol{noisy}} = \overrightarrow{\mathbf{STEC}} + \vec{\boldsymbol{\varepsilon}} = \mathbf{H}.\overrightarrow{\mathbf{N_e}} + \vec{\boldsymbol{\varepsilon}} \tag{5.5}$$

Figure 5.5 summarizes the simulation and validation procedure. Given the coordinates of GPS stations, the setup of voxel dimensions is initialized. Voxel intialization consists of two steps: 1) setting the boundaries of the geographical area of interest in latitude, longitude and height and 2) setting the spacing of each voxel (Δϕ, Δλ, and Δheight). The geographical region used in this work extends from 45° N to 80° N in latitude, 240° E to 304° E in longitude and 80 km to 1180 km in altitude. After voxel initialization, the GPS satellite coordinates are simulated. Providing simulation date, time and duration, GPS satellite coordinates are computed using real broadcast ephemeris corresponding to the simulation time. A relatively low sampling rate of one sample per 120 seconds is used and a cutoff angle of 15° is applied. If the signal is sampled at a higher rate, more rays will penetrate the voxel. However, this will increase the number of rows in the design matrix which will increase the required processing power and time, as well as memory. Additionally, the range of angles between rays within a short period of time does not add significant information. Therefore, a trade-off between the sampling rate, and processing power and memory should be considered.

At this point, all the components required to compute the design matrix **H** in Equation (5.4) are available. The discretization of the problem and computation of the design matrix **H** is explained in Chapter 4. To simulate the measurements, i.e. $\overrightarrow{\mathbf{STEC}}$, a simulation of the ionospheric electron density distribution is required. This can be done using different ionospheric models, such as IRI, PIM and many others. In the voxel-based approach, the electron density is assumed to be homogeneous within each voxel and equal to the density at the centre of the voxel. By extracting the centre coordinates of each voxel and passing them to the ionosphere simulator along with the simulation date and time used to simulate GPS satellite coordinates, the ionosphere is simulated and the truth electron density profile $\overrightarrow{\mathbf{N_e}}^{\mathbf{Truth}}$ is generated. Using Equation (5.4) noise free synthetic $\overrightarrow{\mathbf{STEC}}$ is computed.

To make the simulation more realistic, white Gaussian noise with a standard deviation of 0.1 TECU is added to the synthetic STEC. The design matrix $\mathbf{H}$ and the $\overrightarrow{\mathbf{STEC}}$ measurements vector are differenced with respect to the reference measurement to eliminate the satellite and receiver inter-frequency biases. The outcome of the differencing operation $\mathbf{\Delta H}$ and $\overrightarrow{\mathbf{\Delta STEC}}$ are passed to the ionospheric tomography engine. However, to apply the proposed CIT technique, the spherical cap harmonics parameters and the empirical orthogonal functions are required. Empirical orthogonal functions are computed using the procedure provided in Chapter 4. The spherical cap harmonics are computed after setting the spherical cap pole and half-angle $\boldsymbol{\theta_o}$. The pole is set at the centre of the area of interest, i.e. 62.5° N and 272° E and the half-angle is set equal to half of the latitude span plus a small number to assure the coverage of the longitude span. It is found that the half-angle required to cover the area is 27.5°. Figure 5.3 shows the boundary of the area of interest (green) and the spherical cap boundary (red) required to cover such an area.

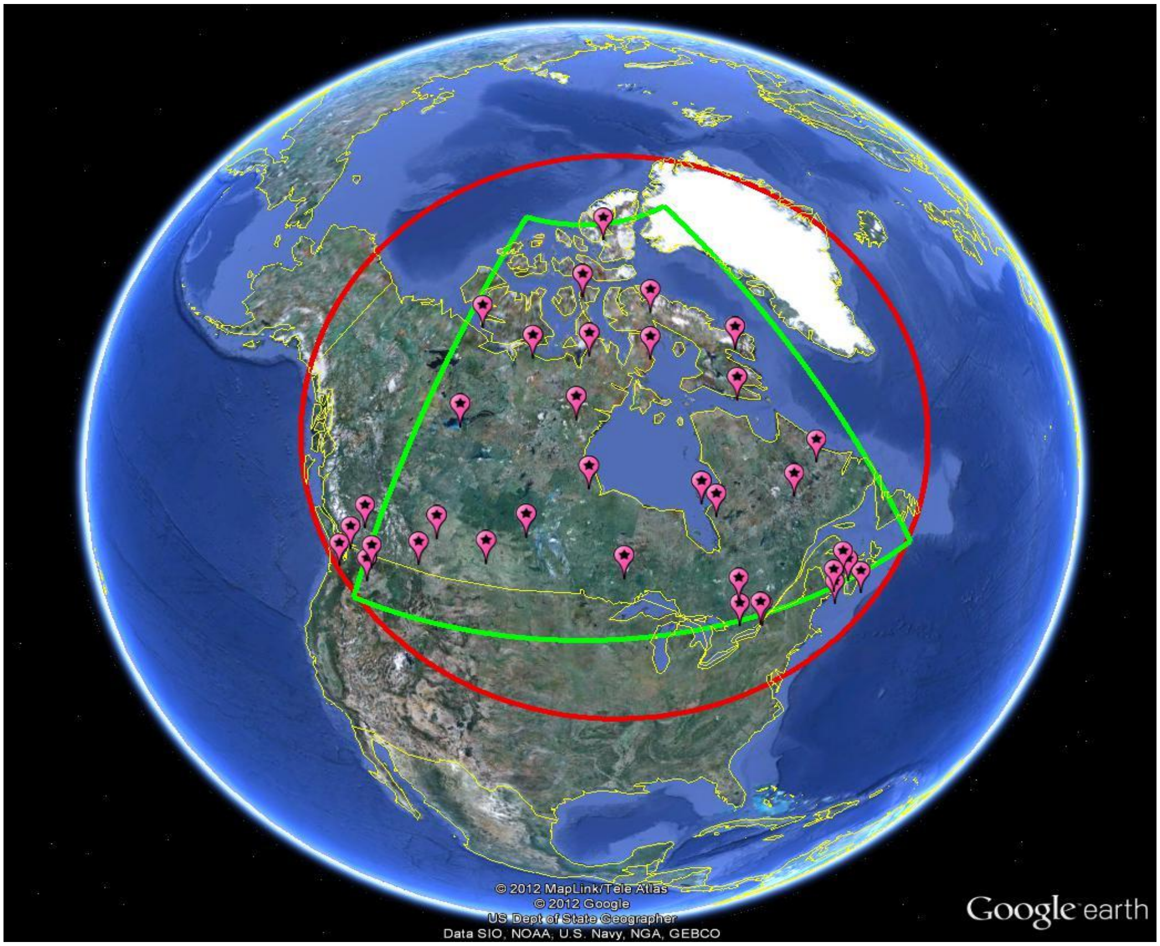

Figure 5.3: Spherical cap boundary (red) and voxel footprints (green)

Setting the number of empirical orthogonal functions (Q) and the maximum order of spherical cap harmonics ($\mathrm{K_{max}}$), the basis functions expressed in a matrix form **B** are computed. Using the design matrix $\mathbf{\Delta H}$, the measurements vector $\overrightarrow{\mathbf{\Delta STEC}}$ and the basis functions matrix **B**, the tomography model coefficients $\vec{\mathbf{m}}$ of Equation (4.44) are estimated using Generalized Tikhonov regularization technique. The estimated electron distribution is then computed using the following:

$$\overrightarrow{\mathbf{N_e}}^{\mathbf{Estimated}} = \mathbf{B}.\vec{\mathbf{m}} \tag{5.6}$$

Equations (5.1), (5.2), and (5.3) are used to assess and validate the inversion technique. The output of the inversion technique is the electron density distribution. TEC is required to compute the metric MAE. TEC can be computed as shown in Figure 5.4. For simplicity, the ionosphere is schematically divided into 9 voxels where each voxel is assigned a different electron density value. Since the voxels' centres are equally spaced, TEC above a point (λ_i, ϕ_i) can be computed using the trapezoidal rule as:

$$\mathrm{TEC}(\lambda_\mathrm{i}, \phi_\mathrm{i}) = 10^{-16} \times \Delta\mathrm{height} \times \sum_{\mathrm{j}=1}^{\text{number of vertical layers}} \mathrm{N_e}\,(\lambda_\mathrm{i}, \phi_\mathrm{i}, \mathrm{h_j}) \tag{5.7}$$

where the units of $\mathrm{N_e}$ and Δheight are el/m^3 and m, respectively. For example, the TEC above point $\mathrm{P_1}$ is equal to $10^{-16} \times \Delta\mathrm{height} \times (\mathrm{N_{e_3}} + \mathrm{N_{e_6}} + \mathrm{N_{e_9}})$ and above $\mathrm{P_2}$ is equal to $10^{-16} \times \Delta\mathrm{height} \times (\mathrm{N_{e_2}} + \mathrm{N_{e_5}} + \mathrm{N_{e_8}})$.

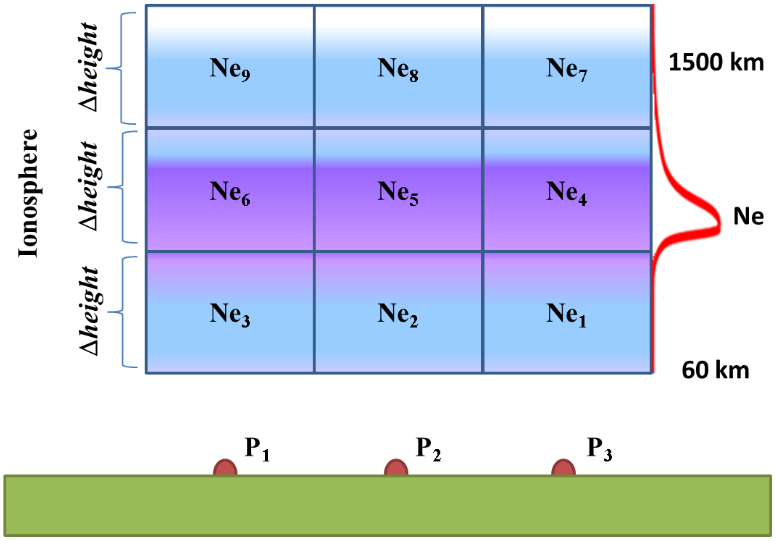

Figure 5.4: Computation of vertical TEC

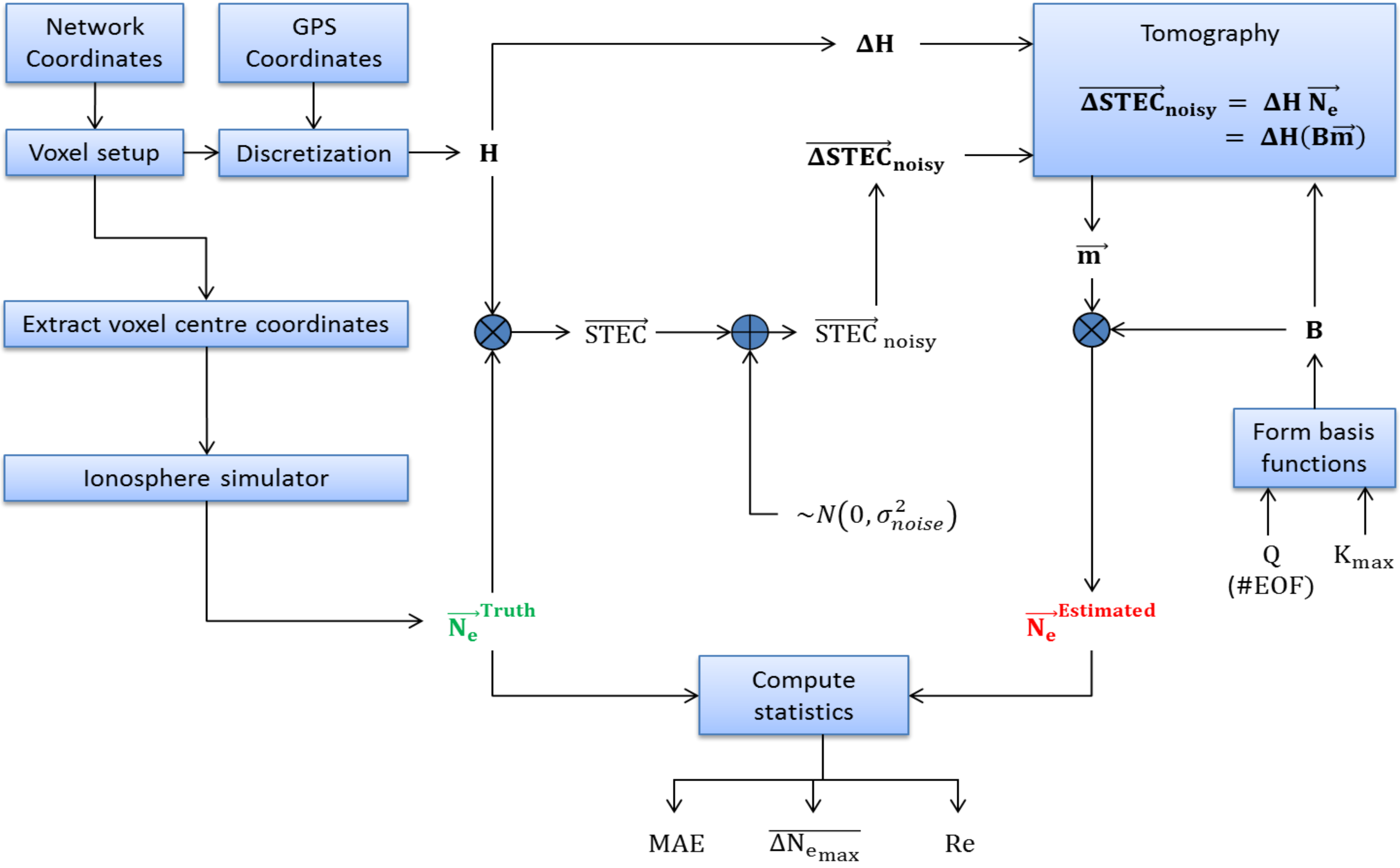

Figure 5.5: Flow chart summarizing the simulation and validation procedure

5.5.1 Simulation of Nominal Ionospheric Conditions

The voxel spacing used in these scenarios is 1° latitude by 4° longitude and 25 km altitude. Based on this spacing, there are 35×16×44 = 24640 unknowns to be estimated using the voxel-based approach. Using the proposed CIT technique, the number of unknowns can be reduced significantly.

The IRI model is used to model the ionosphere. Each scenario consists of two runs where each run has one hour duration and the ionosphere is assumed to be constant within that hour. Following the procedure in Section 5.5, STEC measurements are simulated. Figure 5.6 shows the simulated STEC along PRN 03 LOS for solar maximum (01 January 2000) and minimum (01 January 2009) using IRI-2007 model and real broadcast ephemeris. The satellite elevation and STEC are significantly correlated. As the satellite rises in the sky, the distance travelled through the ionosphere gets shorter resulting in smaller STEC values. The magnitude of STEC is affected by the condition of the ionosphere. During a solar maximum, there is increased ionization causing larger electron densities and thus higher integrated values (i.e. STEC). As a result, the STEC is expected to be larger in solar maximum than solar minimum, which can be seen in Figure 5.6. The magnitude of STEC during solar maximum is almost four times than that of solar minimum.

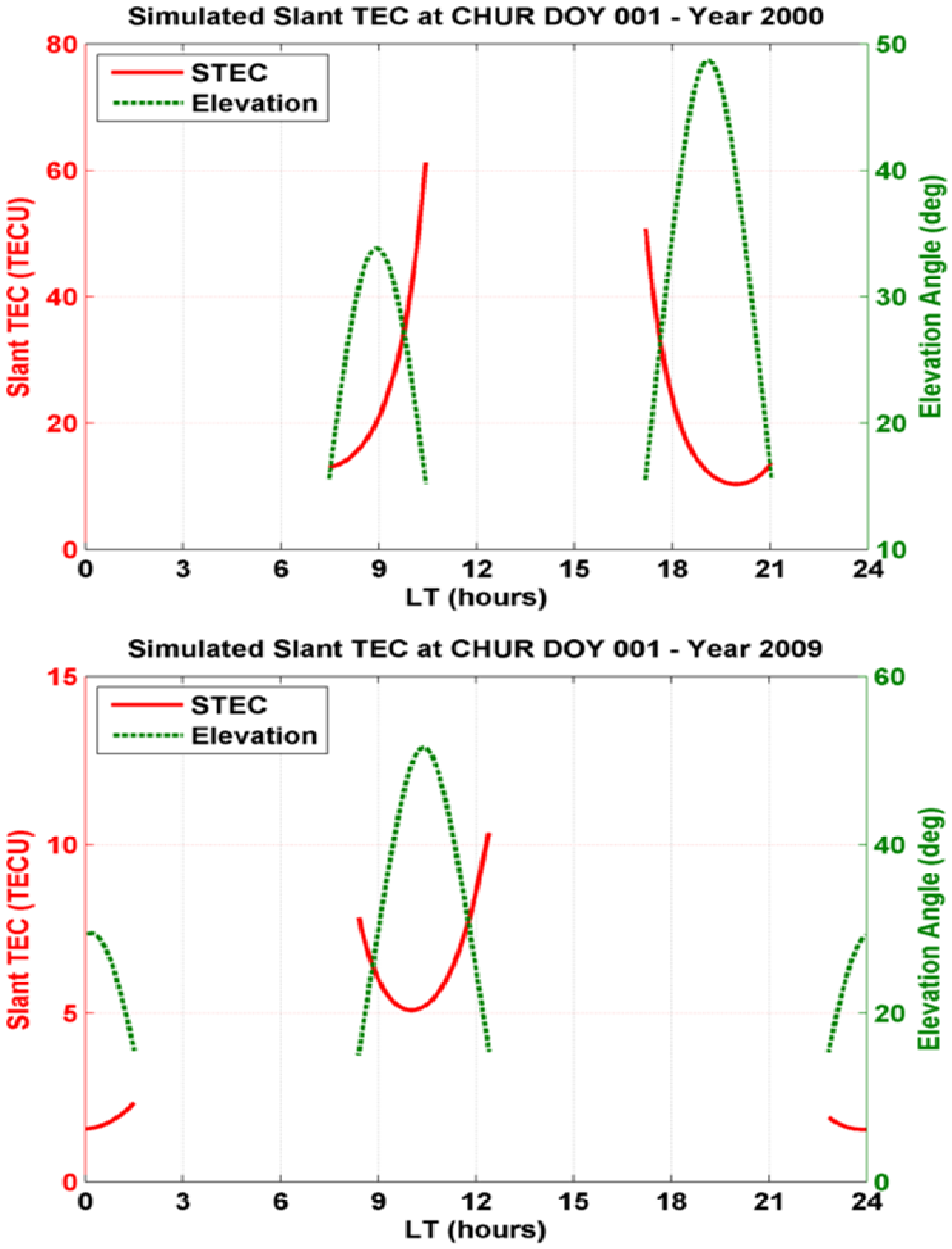

Figure 5.6: Simulated STEC along PRN 3 line-of-sight for Churchill site in solar maximum (top) and solar minimum (bottom)

Figure 5.7 shows the simulated Vertical TEC using IRI model for the three simulated scenarios over the centre voxel (62.5° N and 272° E) over 24 hours in local time. Two important features can be extracted from the figure: The diurnal variation and the peak value of the vertical TEC.

The diurnal variation is evident where the maximum peak occurs at 14:00 LT and the minimum value occurs around sunrise. These scenarios are simulated for different ionospheric conditions; the peak values are a function of these conditions. As expected, the peak value is highest (~26 TECU) during solar maximum (red) and lowest during solar minumum (~4 TECU) .

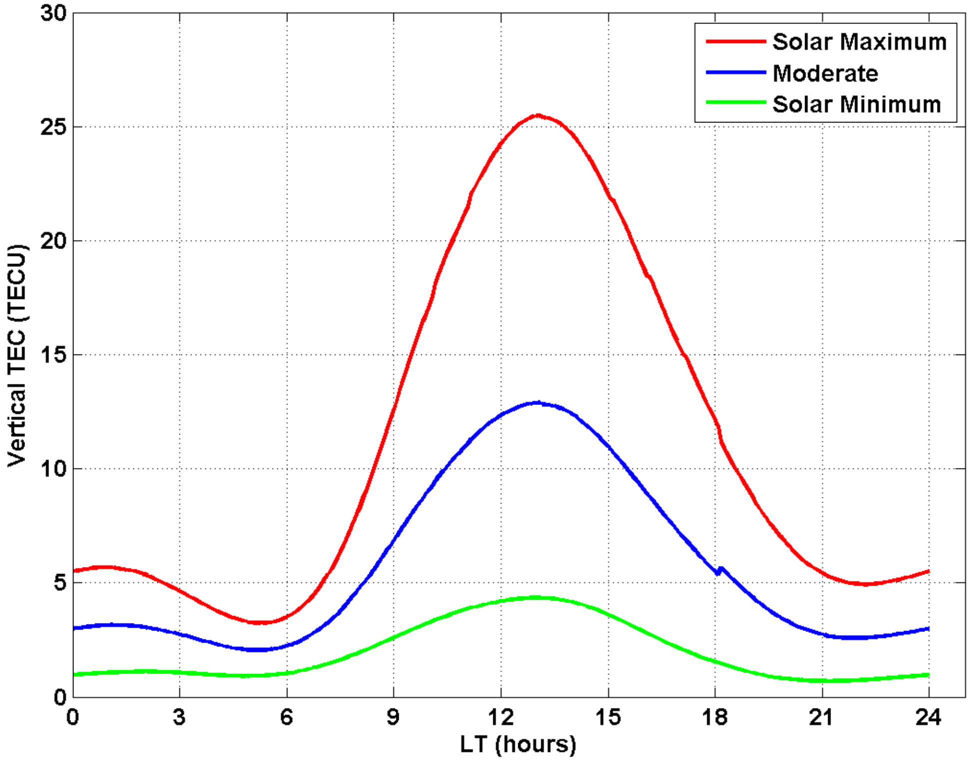

Figure 5.7: Comparison of reference diurnal IRI-TEC variation for solar maximum (red), moderate (blue) and solar minimum (green)

To conduct the analysis, certain times of the day were picked. These times were selected to represent the maximum and minimum vertical TEC value in a day during the three nominal ionospheric conditions. Figure 5.8 shows the maximum value of vertical TEC in the area (Canadian sector) over a period of 24 hours. As expected, it is found that the minimum and maximum vertical TEC values in all different ionospheric conditions occur at 10:00 UT and

21:00 UT, respectively. Therefore, the investigation and the analysis of results are conducted for these specific hours.

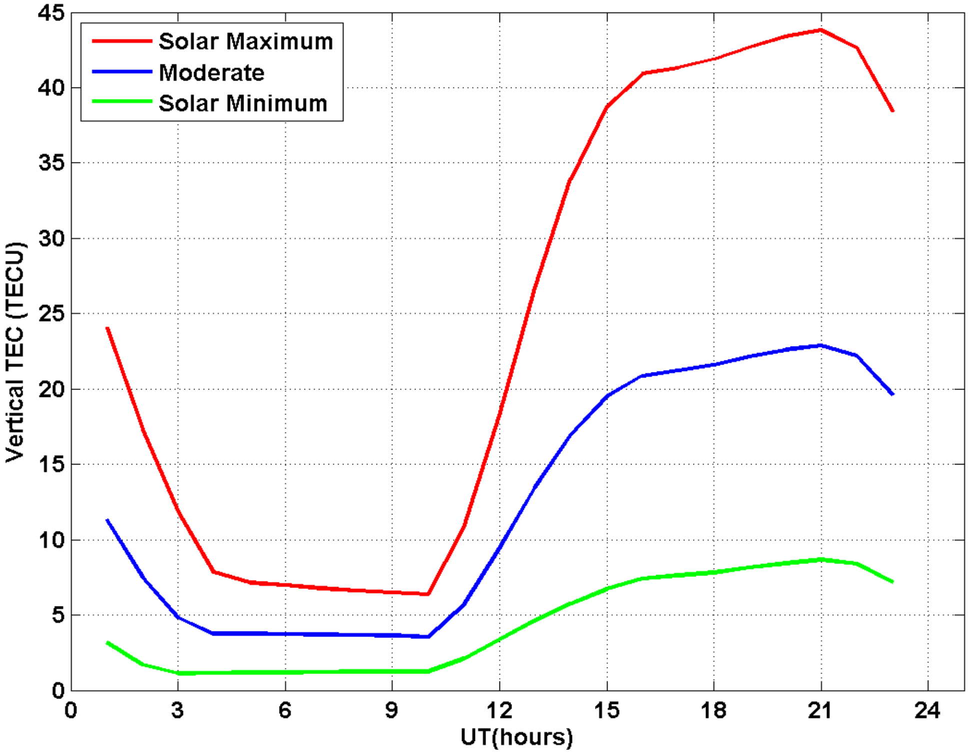

Figure 5.8: Comparison of reference diurnal maximum IRI-TEC variation for solar maximum (red), moderate (blue) and solar minimum (green) in the Canadian sector

Vertical TEC maps computed from simulated electron density profiles are shown in Figure 5.9. Different levels of TEC values are evident during different solar cycle periods. While low TEC values (0.75 – 7 TECU) are common for all solar cycle periods at approximately 10:00 UT, higher values are dominant over much of Canada at 21:00 UT. The ionosphere's dependence on solar activity cycle is observed when comparing the vertical TEC values between 21:00 UT during solar minimum and 10:00 UT during solar maximum. The minimum values of vertical TEC (at 10:00 UT) during solar maximum are close to the maximum values of the day (at 21:00 UT) during solar minimum, which emphasizes the high correlation of vertical TEC with the solar cycle.

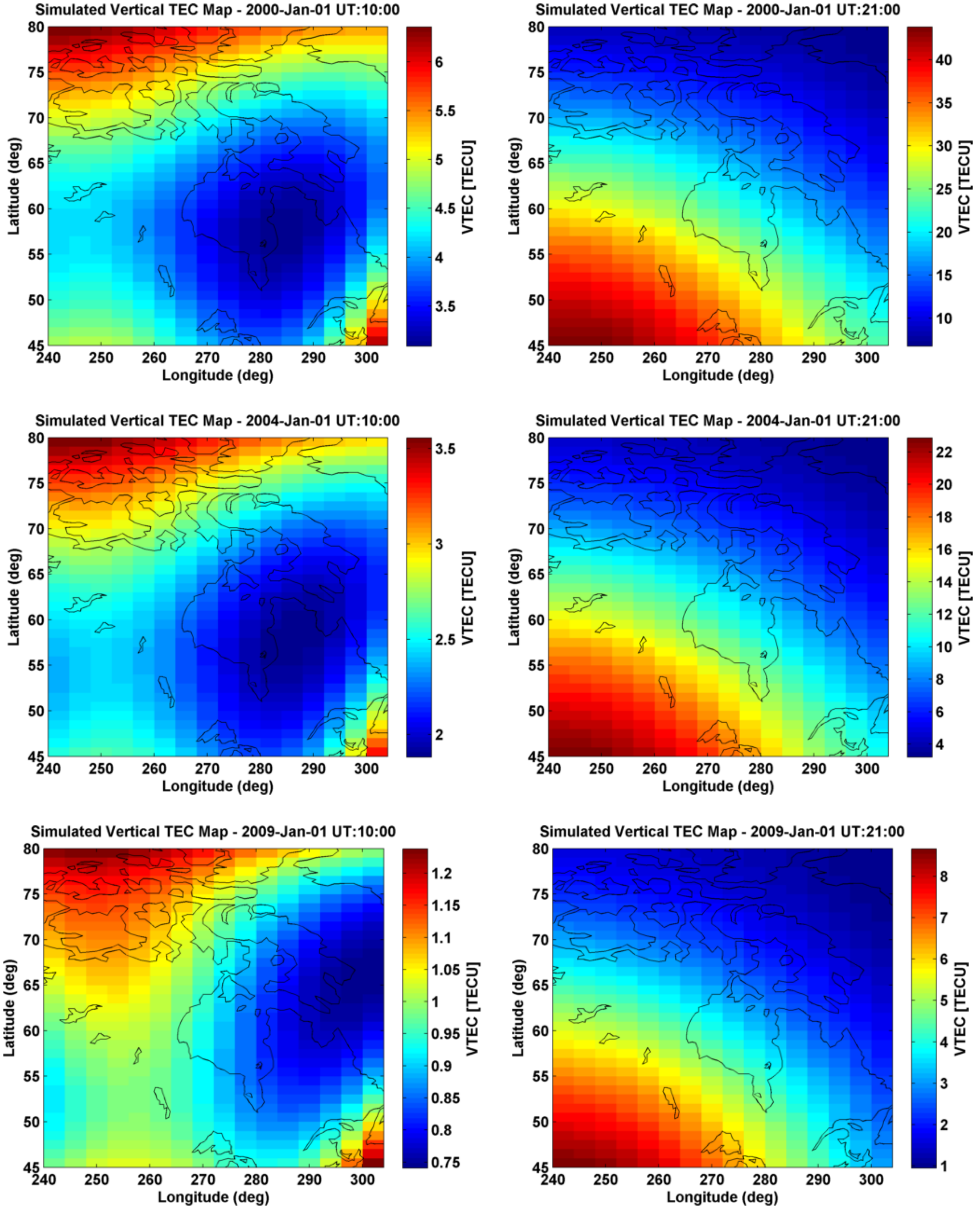

Figure 5.9: Simulated Vertical TEC for 01-January of years 2000 (top), 2004 (middle) and 2009 (bottom) for 10:00 UT(left) and 21:00 UT(right)

5.5.2 Simulation of Storm Ionospheric Conditions

The Storm Enhanced Density (SED) phenomenon can occur over North America. The SED is characterized by a plume of enhanced electron density evolving and extending to higher latitudes (Coster and Skone, 2009). The plume is associated with large vertical TEC gradients causing a sharp drop of TEC values at the edges. Such localized ionospheric events and TEC gradients cause large differential ionospheric range errors affecting Differential GPS (DGPS) and Wide Area Augmentation System (WAAS) users especially near the SED plume where positioning errors can exceed more than 20m (Coster and Skone, 2009).

Modelling SED in three dimensions is challenging and has not been added to available ionospheric models, such as IRI. Therefore, the simulation of this event was done with the assistance of external data. The electron density distribution during 29-30 October 2003 storm was estimated using IDA3D model (Bust et al., 2004). The electron density profile for 21:00 UT was provided along 240° E longitude using 5° latitude spacing. A voxel spacing of 5° in latitude, 5° in longitude and 25km in altitude is used for the SED simulation. For simulation purposes, these profiles are shifted to the middle of the area of interest at 266.5° E. IRI model is also used as background and the electron density is simulated at the centre of the remaining voxels to compensate for the missing electron density profiles. This simple approach initially results in unrealistic electron density profiles since there are only high electron density values along 266.5° E longitude which is ~30 times greater than those simulated by IRI. Therefore, a weighted averaging of the IDA3D and IRI electron density profiles is used to simulate large westward and northward gradients at the edges of the plume. The simulation of the electron density profile along 266.5° E longitude and the vertical TEC map are shown in Figure 5.10.

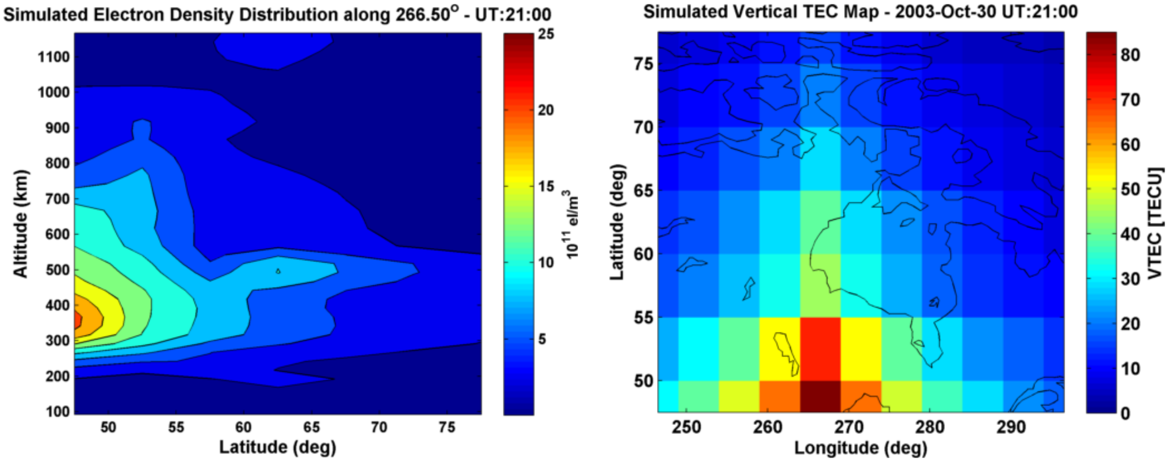

Figure 5.10: Simulated electron density profile (left) and vertical TEC map (right) of a storm enhanced density

Table 5.2: Simulation settings

	Nominal conditions	Storm conditions (SED)
Region boundaries	ϕ = 45° N – 80° N λ = 240° E – 304° E height = 80 km – 1180 km	
Voxel spacing ($\Delta\phi \times \Delta\lambda \times \Delta$height)	1° × 4° × 25km	5° × 5° × 25km
Ionosphere simulator	IRI – 2007	External source (IDA3D) + IRI-2007
Simulation date and year	Solar maximum (01 Jan 2000) Solar moderate (01 Jan 2004) Solar minimum (01 Jan 2009)	SED (30 Oct 2003)
Simulation time of day	10:00 UT and 21:00 UT	21:00 UT
Simulation duration	60 minutes	
Data sampling rate	Sample per 120 seconds	
SCH pole	62.5° N and 272° E	
SCH half-angle θ_o	27.5°	

5.6 Determination of SCH and Number of EOF

The degree of Spherical cap harmonics (K_{max}) and the number of empirical orthogonal functions (Q) control the number of unknowns to be estimated. Using lower K_{max} and Q leads to lower number of unknowns. Choosing high degree and number of EOFs generally results in a better representation (higher resolution) of the electron density profile, but this makes the design matrix singular and severely ill-conditioned which can make the problem susceptible to noise and small errors affecting the solution - even causing it to converge to the wrong solution. Therefore, determining the appropriate degree of spherical cap harmonics (K_{max}) and the number of empirical orthogonal functions (Q) is important in this model.

As will be shown later, high values of Q and K_{max} result in better fitting. However, the condition number of the design matrix will be very high affecting the accuracy of the inversion significantly. Therefore, a trade-off between model accuracy and ability to invert the problem must be considered. The determination process consists of two parts: 1) evaluation of the system model representing the electron density, i.e. SCH and EOF, and 2) evaluation of the measurement model and the proposed CIT technique to reconstruct the electron density. In the first part, the lowest possible values of K_{max} and Q are determined and these values are used to evaluate the measurement model.

Since the ionospheric tomography problem is a severely ill-conditioned problem, the level of noise and the observation geometry play a major role in the performance of the proposed technique. Therefore, the initial procedure to determine the optimized K_{max} and Q values is based on how well the model can describe the electron density distribution, i.e. Equation (4.44).

IRI model is used to simulate electron densities over the Canadian polar region which in turn are used to assess the fit. The criteria used in the assessment are Re, MAE, and $\overline{\Delta N_{e_{max}}}$.

5.7 Model Evaluation

As discussed in Chapter 4, EOFs and spherical cap harmonics can be utilized to represent the electron density distribution in 3D. EOFs are used to describe the distribution vertically and spherical cap harmonics are used to describe the distribution horizontally. To determine the order of spherical cap harmonic (K_{max}) and number of EOFs (Q), different combinations of K_{max} and Q are used and an assessment of the system model is conducted. The goal of this assessment is to assess the ionospheric model of Equation (4.44) and to choose the minimum K_{max} and Q that meet the targeted performance metrics (if not better) and yield a good representation of the electron density profile and extraction of different ionospheric parameters.

5.7.1 Nominal Ionospheric Conditions

Figure 5.11,Figure 5.12 and Figure 5.13 show the average maximum peak value error ($\overline{\Delta N_{e_{max}}}$), mean absolute error in TEC (MAE) and the normalized reconstruction error in the electron density (Re), respectively. The results confirm the fact that the electron density profiles can be described more accurately if higher K_{max} and Q are used. The first EOF, which is the most dominant function, represents a mean electron density profile. The higher order EOF's allow the variation of the profile from the mean. However, their significance decreases gradually to a point where including additional EOFs does not add any significant information. This can be seen clearly in the figures. The variance generated by the higher order EOF's decreases significantly and including such EOF's will increase the condition number of the design matrix and make the inversion technique unstable. During all ionospheric conditions, the performance of the model is poor when using Q = 1 or 2. The performance improves drastically if Q = 3 or higher is used. This is expected since using higher degree of EOF's allows the model to represent the profile accurately especially around the maximum peak height (~300 km altitude) as explained earlier in Chapter 4. As a result, the minimum value of Q that should be used in this model should be higher than or equal to three.

EOF's are used as the basis function describing the profiles vertically. To be able to represent the profile horizontally, spherical cap harmonics are used. For cases where Q = 3, results show that the minimum $\mathrm{K}_{\mathrm{max}}$ at which the results are improved significantly is equal to three. As a result, the minimum optimum values of $\mathrm{K}_{\mathrm{max}}$ and Q over the Canadian polar region chosen for this work are chosen to be 3 and 3, respectively.

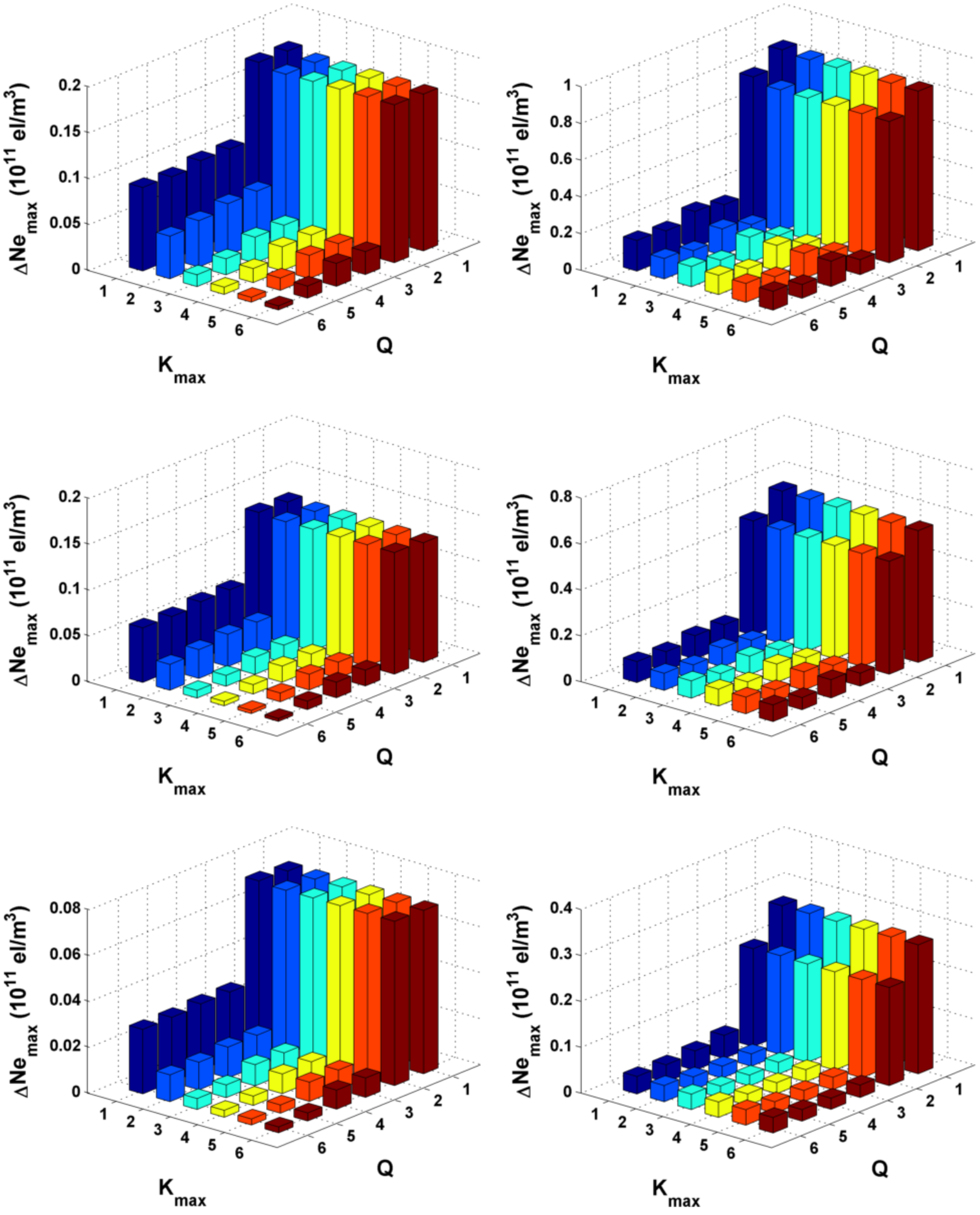

Figure 5.11: Average maximum peak value error $\left(\overline{\Delta N_{e_{max}}}\right)$ for 01-January of years 2000 (top), 2004 (middle) and 2009 (bottom) for UT 10:00 (left) and UT 21:00 (right)

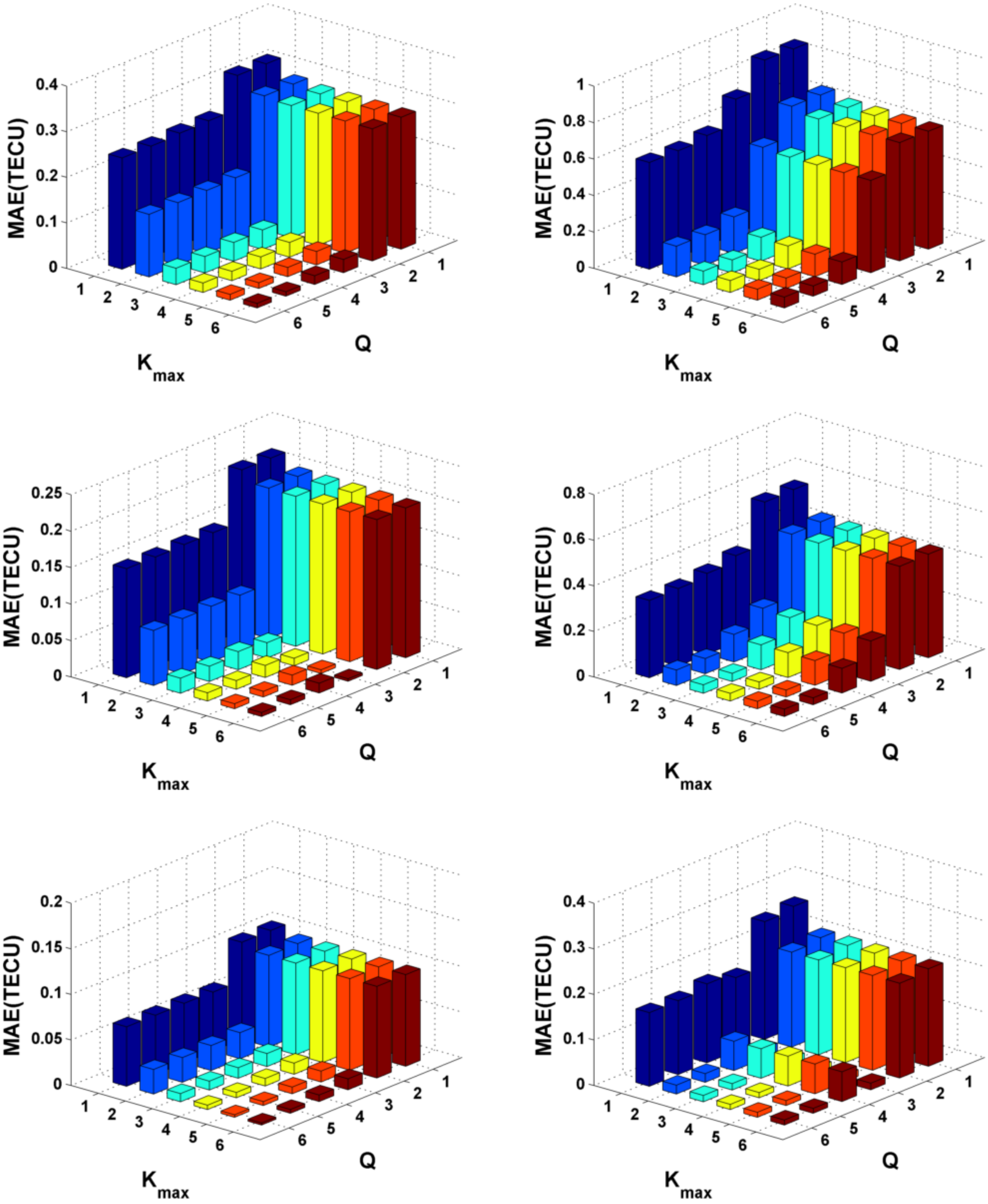

Figure 5.12: Mean absolute error (MAE) in TEC for 01-January of years 2000 (Top), 2004 (Middle) and 2009 (Bottom) for UT 10:00 (Left) and UT 21:00 (Right)

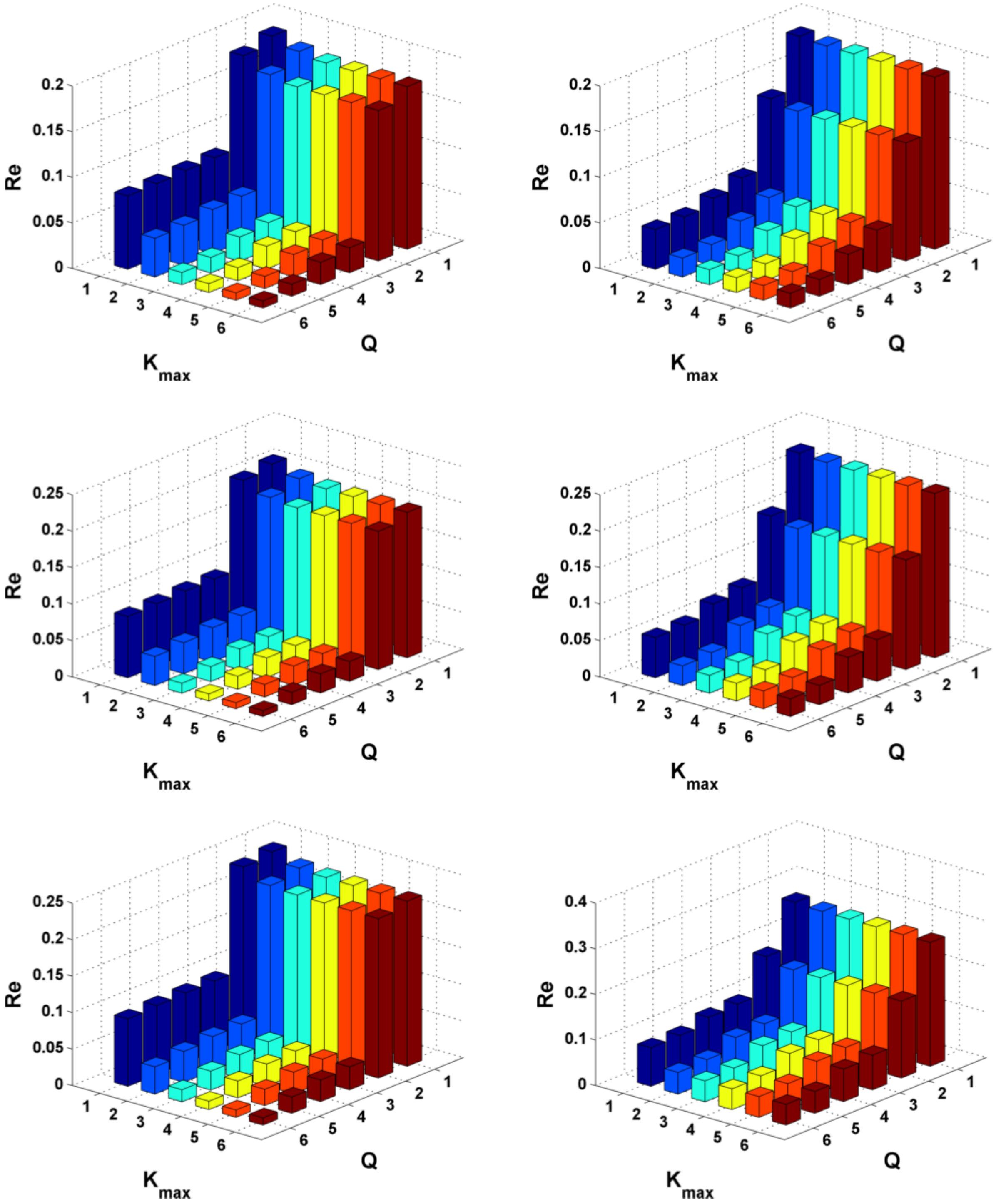

Figure 5.13: Reconstruction error (Re) for 01-January of years 2000 (top), 2004 (middle) and 2009 (bottom) for UT 10:00 (left) and UT 21:00 (right)

In the previous step, the best minimum $\mathrm{K_{max}}$ and Q values are determined through evaluating the model fit and how well it can represent the electron density profile. The next step is to test the performance of the proposed CIT technique using these values. Table 5.3 summarizes the results of the inversion for the three nominal ionospheric conditions at 10:00 and 21:00 UT. Results show high correlation between the ionspheric conditions and the different error metrics. As the solar activity decreases from maximum to minimum, the errors decrease. This is evident in the average maximum electron density peak $\overline{\Delta \mathrm{N_{e_{max}}}}$ where the error is lower for solar minimum than solar maximum. The same applies to the errors for local day (21:00 UT or 14:00 LT) versus local night (10:00 UT or 03:00 LT). Re and MAE in TEC behave similarly for day versus night. However, it is observed that the errors during 2004 (moderate case) are higher than during solar maximum for MAE and Re.

Table 5.3: Assessment of the model using $\mathbf{K_{max}}$ = 3 and Q = 3

	10:00 UT			**21:00 UT**		
	Re	**MAE** (TECU)	$\overline{\Delta \mathrm{N_{e_{max}}}}$ 10^{11} el/m^3	**Re**	**MAE** (TECU)	$\overline{\Delta \mathrm{N_{e_{max}}}}$ 10^{11} el/m^3
2000	**0.12**	**0.07**	**0.31**	**0.22**	**0.17**	**0.91**
2004	**0.18**	**0.13**	**0.16**	**0.27**	**0.18**	**0.73**
2009	**0.11**	**0.09**	**0.10**	**0.19**	**0.14**	**0.20**

Since the three cases are similar, the results for 21:00 UT are presented as an example to demonstrate the capability of the proposed technique for estimating different ionospheric parameters over the Canadian polar region. Figure 5.14 shows the estimated vertical TEC map and the associated errors in the estimation. It can be seen that the technique has produced a very accurate representation of the vertical TEC and the gradients associated with it. The reconstructed maps show underestimation of TEC in some regions and overestimation in other regions. This is due to the use of a limited number of empirical orthogonal functions and low degree of spherical cap harmonics. However, a higher degree and number of orthogonal function will lead to a higher condition number making the design matrix sensitive to small errors resulting in a worse solution.

The proposed CIT technique estimates the model coefficients rather than the electron density profiles. The estimated coefficients are then used in Equation (4.46) to describe the electron density distribution. Figure 5.15 shows an example of the reconstructed electron density profile along 270° E longitude using the estimated coefficients. It can be observed that most of the features are well replicated and the image represents the peak height, maximum electron density and electron density distribution adequately. Re for 01 January 2000, 2004 and 2009 at 21:00 UT simulations are 0.22, 0.27 and 0.19, respectively, which are within the required values and meet the targeted performance metrics. The error in the maximum peak height is within 25 km, which is the thickness of the voxel.

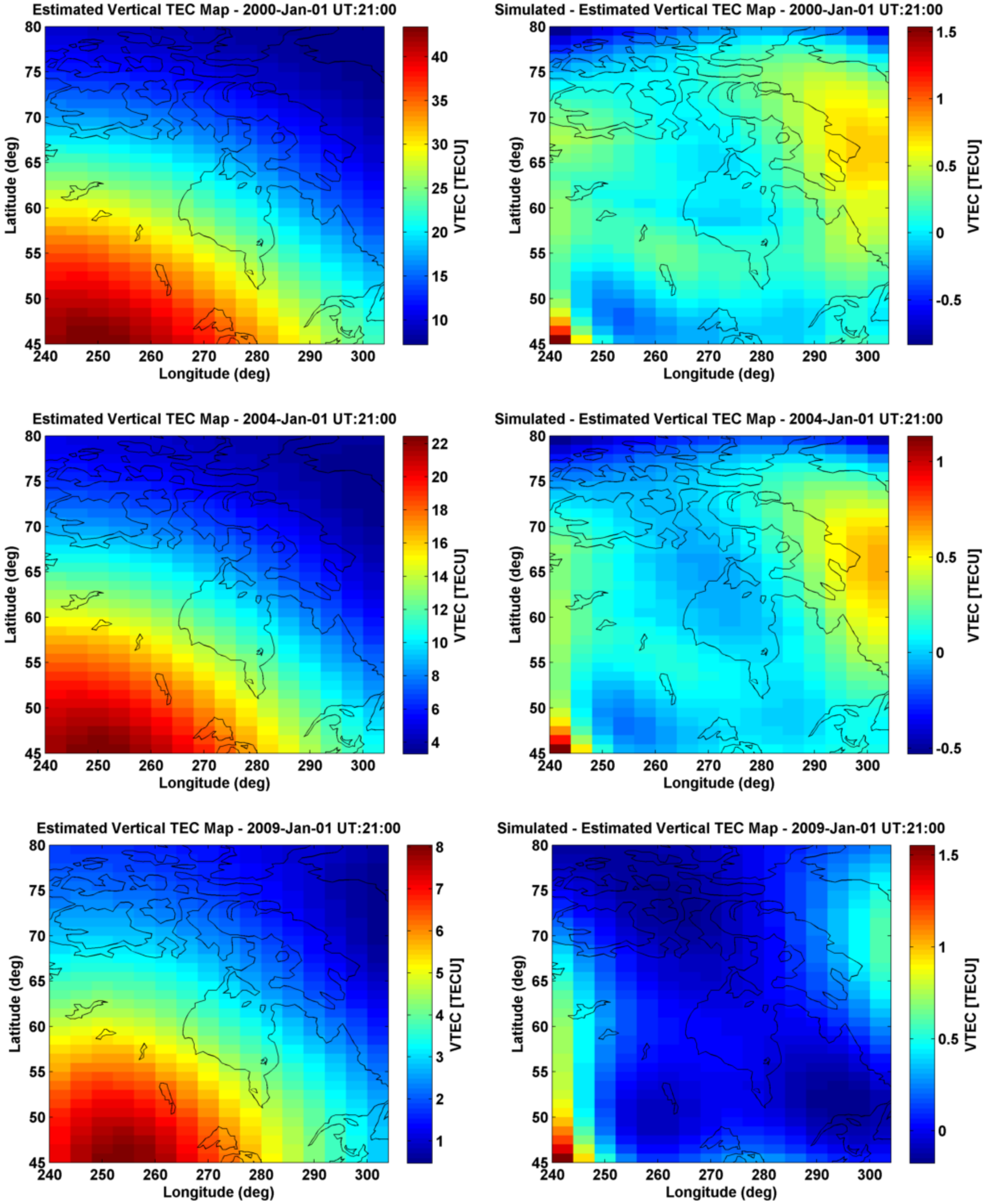

Figure 5.14: Estimated vertical TEC maps using simulated IRI STEC (left) and the difference between the estimated and simulated TEC maps (right) for 01 January 2000 (top), 2004 (middle) and 2009 (bottom) for UT 21:00 (K_{max} =3 and Q = 3)

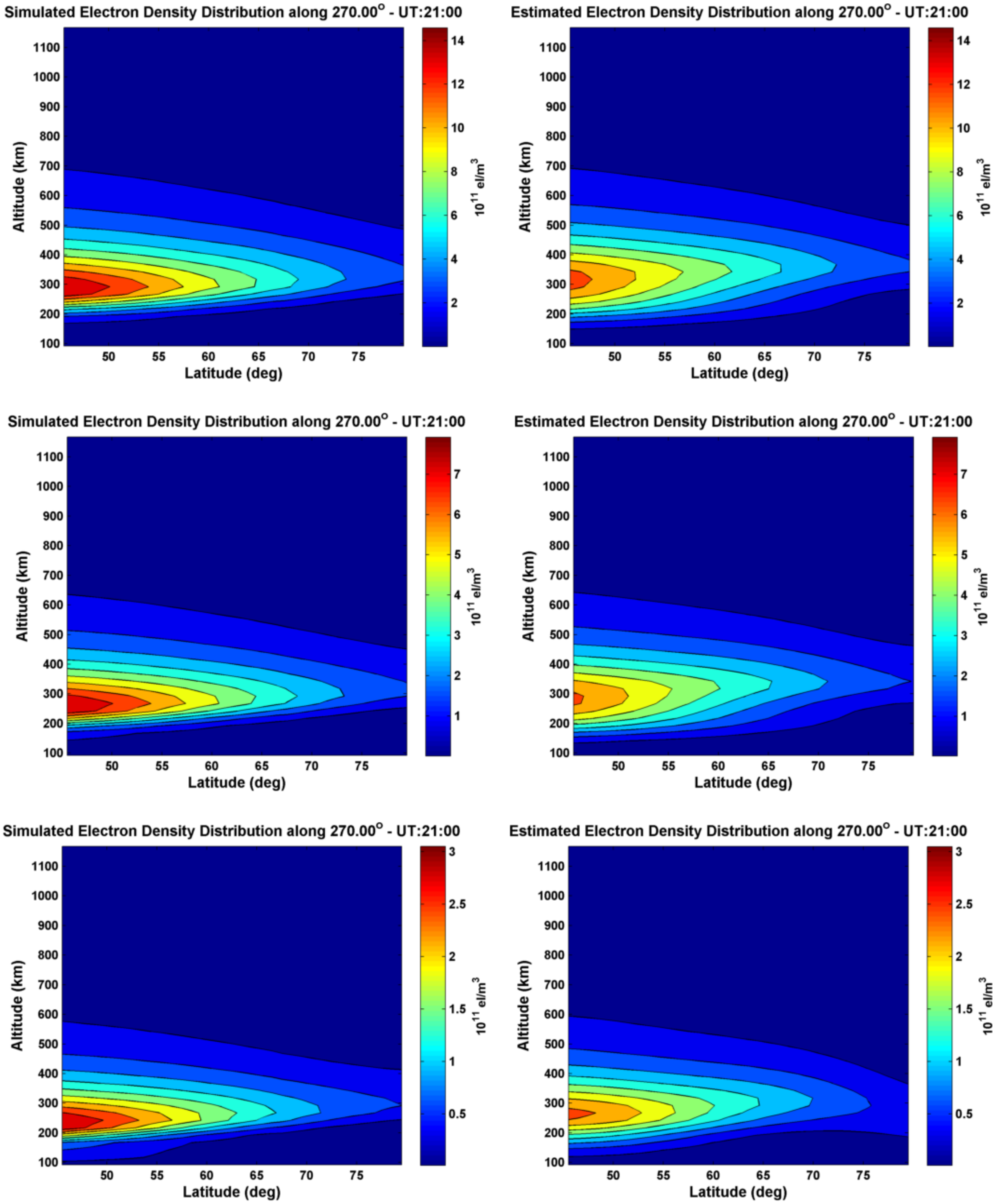
Simulated Electron Density Distribution along 270.00° - UT:21:00

Estimated Electron Density Distribution along 270.00° - UT:21:00

Simulated Electron Density Distribution along 270.00° - UT:21:00

Estimated Electron Density Distribution along 270.00° - UT:21:00

Simulated Electron Density Distribution along 270.00° - UT:21:00

Estimated Electron Density Distribution along 270.00° - UT:21:00

Figure 5.15: Simulated (left) and estimated (right) electron density distribution IRI along 270° E longitude for 01 January 2000 (top), 2004 (middle) and 2009 (bottom) for UT 21:00 (K_{max} =3 and Q = 3)

Residual analysis provides useful information; for example residuals must be checked for blunders and goodness of fit. Histograms of the residuals for the three ionospheric conditions at 21:00 UT are shown in Figure 5.16. As expected, the residuals are normally distributed, which confirms the assumption (parameters are normally distributed). The absolute values of the residuals are less than 0.5 TECU, which indicates statistically a good fit of the solution to the model given that an independent distributed random noise with standard deviation of 0.1 TECU is added to the simulated measurements. The root mean square of the residuals is 0.14 TECU which is higher than the noise standard deviation. This can be explained by the law of propagation error. As mentioned in Chapter 4, the measurement matrix is differenced to eliminate the receiver and satellite biases. This operation will increase the noise standard deviation by a factor of $\sqrt{2}$ resulting in noise with a standard deviation of $\sqrt{2} \times 0.1 = 0.14$ TECU.

As explained earlier, the electron density profiles can be reconstructed using the proposed CIT technique. Using the reconstructed profiles, the vertical TEC above a given point can be computed using Equation (4.46) and vertical TEC maps can be generated. Figure 5.17 and Figure 5.18 present the vertical TEC maps on 01 January 2000 for the selected hours. The computed maps are compared to the simulated vertical TEC maps and the statistics of the errors are presented in Table 5.4. Slight variation in the accuracy is observed over time. Nevertheless, the accuracy of the inversion is better than 0.5 TECU.

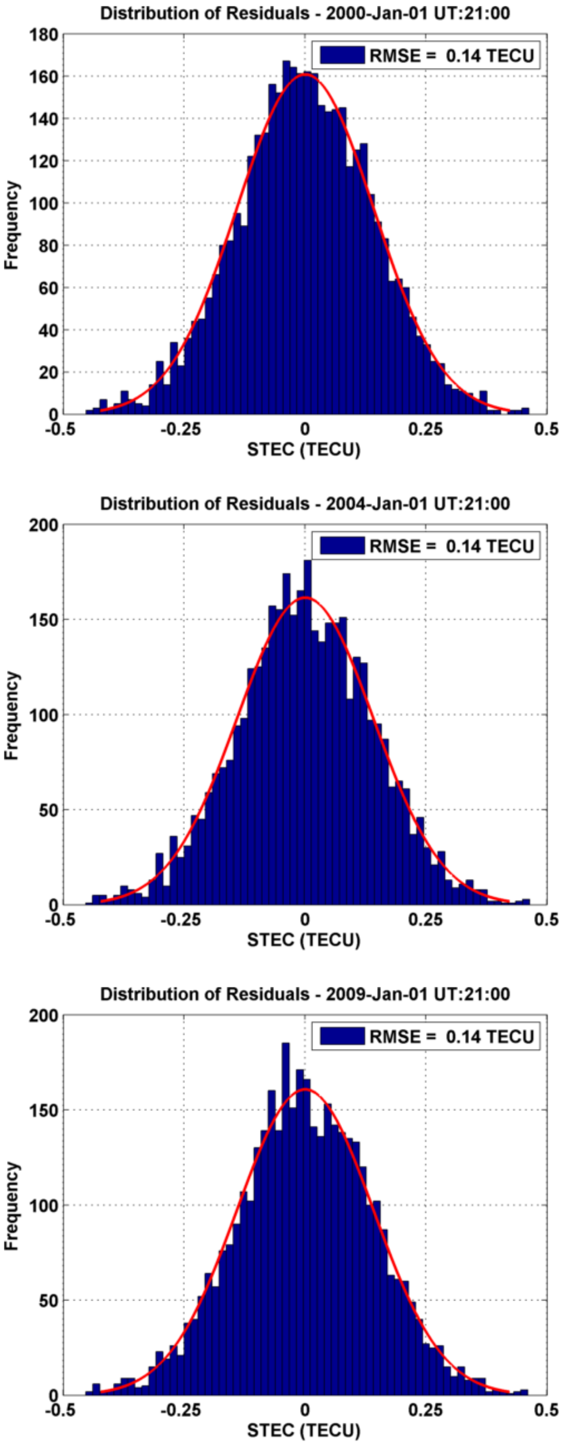

Figure 5.16 Histogram of the residuals for 01 January 2000 (top), 2004 (middle) and 2009 (bottom) for UT 21:00 (K_{max} =3 and Q = 3)

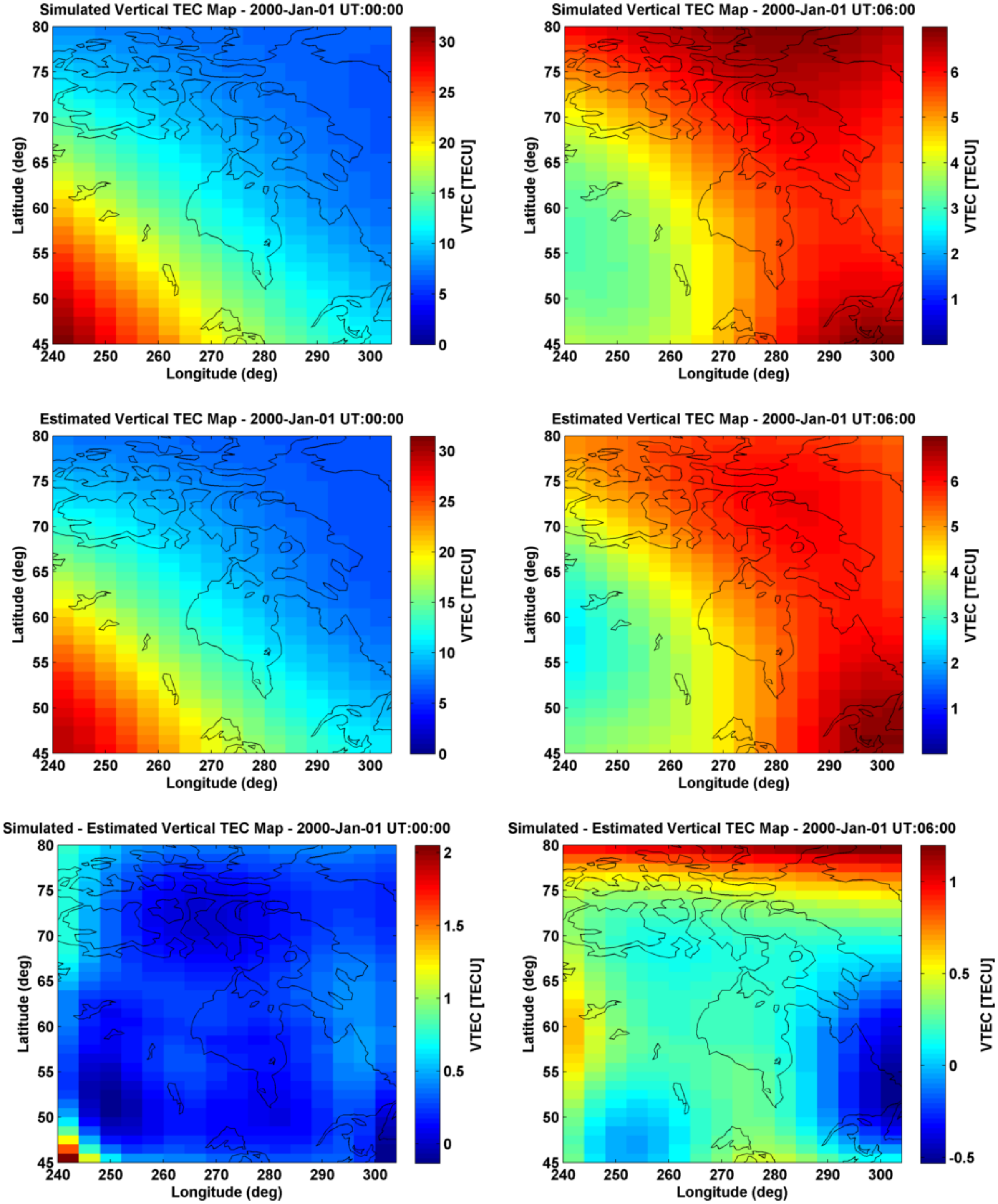

Figure 5.17:Comparison between simulated (top), estimated (middle) vertical TEC maps and the error in the estimation (bottom). Results are shown for 01 January 2000 for UT 00:00 (left) and UT 06:00 (right) using K_{max} =3 and Q = 3.

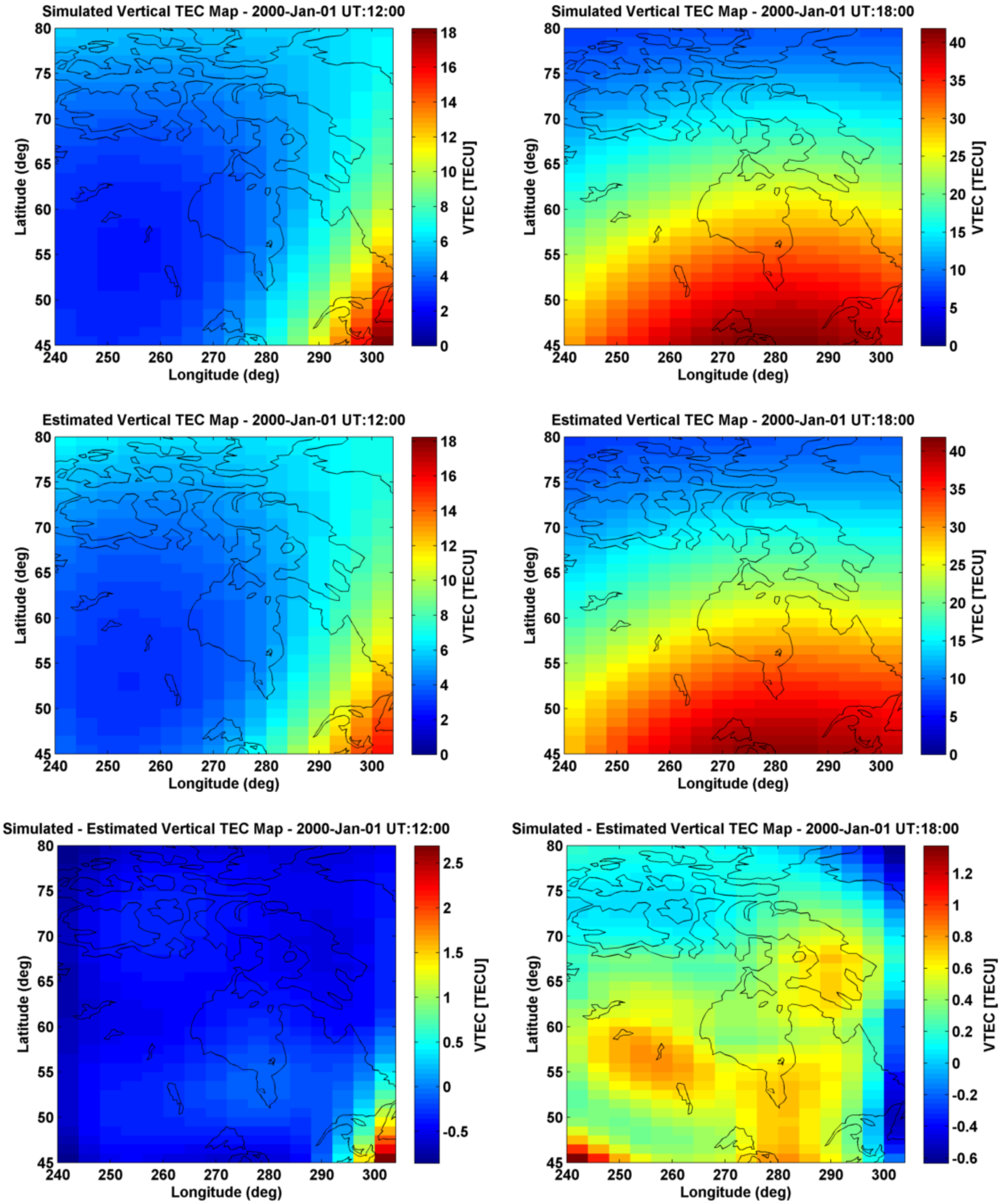

Figure 5.18 Comparison between simulated (top), estimated (middle) vertical TEC maps and the error in the estimation (bottom). Results are shown for 01 January 2000 for UT 12:00 (left) and UT 18:00 (right) using K_{max} =3 and Q = 3.

Table 5.4: Statistics on the vertical TEC error on 01 January 2000.

Hour (UT)	Min (TECU)	Max (TECU)	Mean (TECU)	RMSE (TECU)
00:00	-0.13	2.05	0.26	0.19
06:00	-0.53	1.20	0.25	0.31
12:00	-0.85	2.69	-0.35	0.33
18:00	-0.63	1.38	0.35	0.29

5.7.2 Storm Conditions

The model has been tested and challenged in nominal ionospheric conditions during solar minimum and maximum. To generate additional realistic and quantitative performance measures, the model is tested under ionospheric storm conditions (in this case SED). An assessment of the CIT model is conducted under SED challenging conditions.

Using K_{max} = 3 and Q = 3, the CIT technique produces vertical TEC maps shown in Figure 5.19. Due to the limitation of the technique, the model is not able to retrieve an accurate representation of vertical TEC map. The errors in TEC values (MAE = 7.5 TECU) are considerably high, especially along the plume and its edges. This is due to the fact that the limited number of EOFs do not fully represent a highly variable ionosphere. IRI model (used to generate the EOF's) was derived using long-term mean values of ionospheric measurements. IRI reflects average approximation of nominal ionosphere conditions which does not include such challenging conditions as SED. Therefore, even if a higher number of EOFs are used, the results will not improve and they may be worse due to the fact that the condition number of the design matrix will be larger causing the model to be more sensitive to errors. This is demonstrated in Table 5.5. Different K_{max} and Q values are used and the statistics of the errors corresponding to the solution using these values are listed. As the number of EOF increases the condition number of the design matrix increases and as a result the errors become larger.

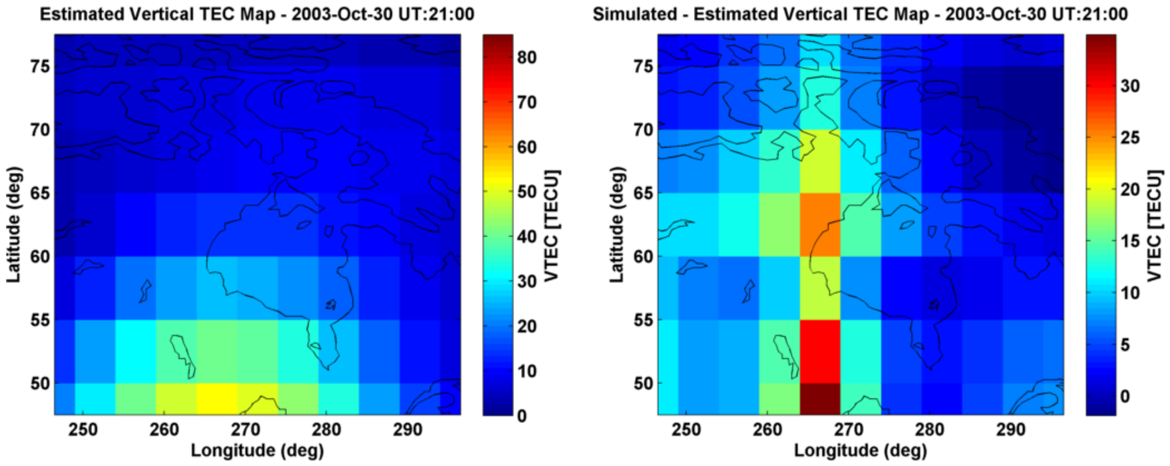

Figure 5.19: Estimated vertical TEC map (left) and the error in the estimation (right) using K_{max} =3 and Q = 3.

Table 5.5: Error statistics using different K_{max} and Q

(K_{max},Q)	Re	MAE (TECU)	$\overline{\Delta N_{emax}}$ **10^{11} el/m^3**	Condition Number
(3,3)	**0.55**	**7.42**	**1.59**	**800**
(4,4)	**0.63**	**12.28**	**2.12**	**8581**
(5,5)	**0.69**	**15.50**	**2.47**	**73184**

Although the proposed CIT technique does not produce accurate images, the solution computed by the technique minimizes the errors in a least squares sense. To further make use of this information, the solution can be used as an initial guess and a constraint imposed on the ionospheric tomography in its original form as in Equation (4.22). This approach forces the model to be close to the initial guess and refines it to a better solution so that the residuals are minimized. However, the design matrix (**H**) is rank-deficient and severely ill-conditioned; therefore the regularization technique described in Chapter 4 is used to solve the problem. Figure 5.20 shows the refined image using the solution of the proposed CIT as an initial guess. The SED feature is recognisable and the gradients at the edges of the plume are recovered. The errors in vertical TEC maps are reduced significantly (MAE = 3.7 TECU).

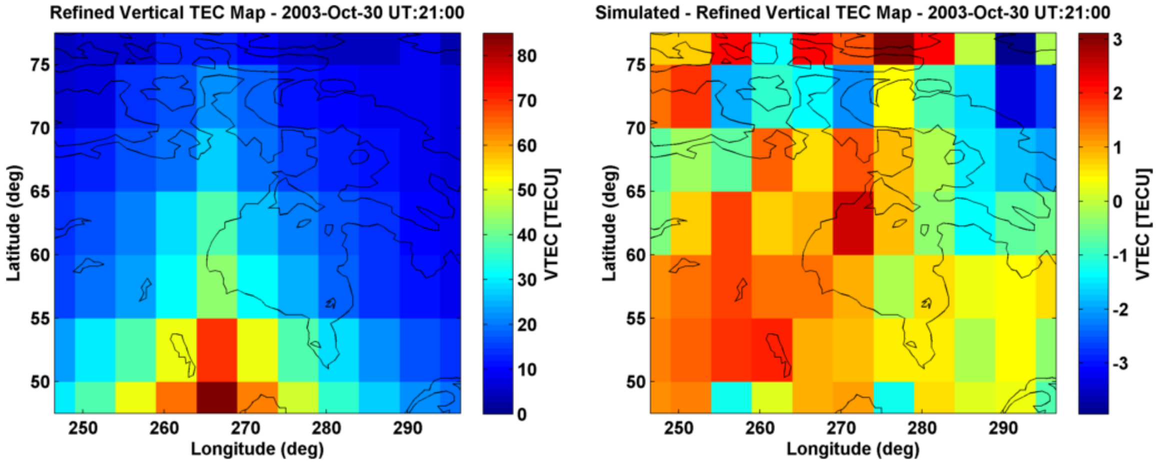

Figure 5.20:Refined vertical TEC map (left) and the error in the estimation (right).

Figure 5.21 shows the estimated electron density using the proposed CIT technique and the refined estimated electron density achieved by solving the ionospheric tomography model using the first solution as an initial guess to constrain the model. As explained earlier, CIT using EOF and SCH does not recover the values of electron density profile accurately. However, this technique can estimate the peak altitude of maximum electron density adequately. Using the refinement technique, more features are recovered and better representation of the peak height and value is achieved. As a result, the reconstruction error of the electron density (Re) is improved from 0.55 to 0.38.

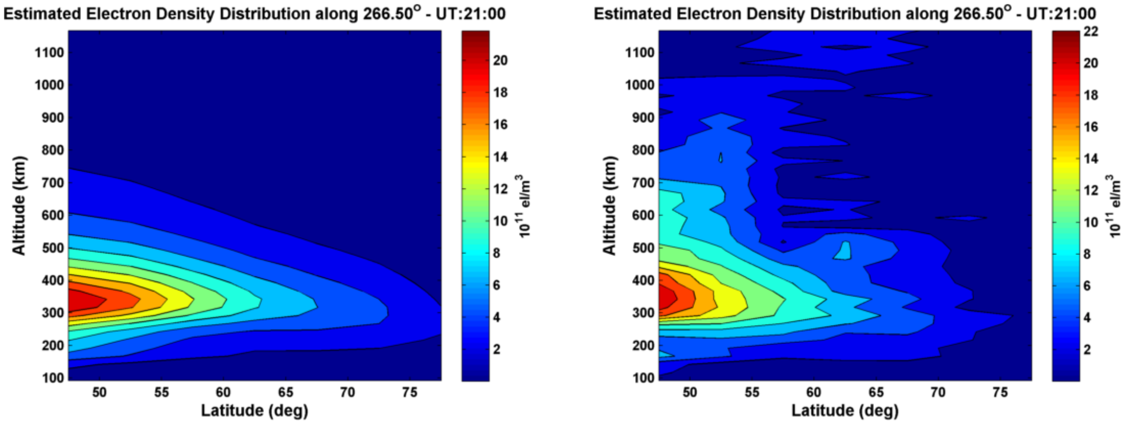

Figure 5.21: Estimated electron density profile along 266.5° E longitude. Results are shown for CIT using SCH and EOF (left) and constrained CIT (right)

5.8 Chapter Summary

A new CIT technique using SCH and EOF has been developed and evaluated to estimate different ionospheric parameters using ground GPS observations. In this chapter the proposed technique is tested using simulation. IRI-model is used to generate simulation and reference data as an input to the model. Also, SED ionospheric condition has been simulated using IRI model with the help of external data (IDA3D). Qualitative and quantitative TEC and electron density profile comparisons are generated. The model is tested under different nominal ionospheric conditions during solar minimum and maximum, and the best optimum values of $K_{\max}$ and Q over Canadian polar region are determined to be 3 and 3, respectively. Simulation results are promising and show that the technique performs well in meeting the targeted performance metrics under nominal conditions. To add higher levels of complexity to the analysis, the technique is tested under challenging storm conditions, i.e. SED, and limitations of the model are identified and quantified under such conditions. Under storm challenging conditions, the proposed CIT technique fails to replicate and reconstruct electron density profiles that meet the targeted performance metrics due to the fact that the enhanced electron density of such a storm is not modeled in the background ionosphere from which the EOF are derived. Therefore, the basis functions (EOF) will not be able to model the electron density profile vertically. An approach is proposed to better estimate the electron density distribution, where the solution of the proposed CIT technique is used to impose a constraint on the ionospheric tomography in its original form. However, this approach requires high computational load and memory and inverting the problem might be challenging, especially if a higher resolution, i.e. higher number of unknowns, is required.

Chapter Six: Ionospheric Tomography Modelling – Real Data

6.1 Introduction

As determined in Chapter 5, the most appropriate combination of values for $\mathrm{K}_{\mathrm{max}}$ and Q for the Canadian polar region is found to be 3 and 3 respectively. These values are determined based on a realistic wide area network of GPS reference stations and simulated ionospheric conditions. The electron density distribution is simulated using IRI-2007 model and the GPS satellite coordinates are simulated using real GPS broadcast ephemeris. Utilizing this information, the STEC can be integrated and used as an input to the CIT model. However, simulated data demonstrate the feasibility of the proposed tomographic technique without the effect of errors (such as outliers) found in real data. GPS derived STEC measurements are susceptible to cycle slips and highly affected by noise. Since the design matrix is singular and severely ill-conditioned, these errors can affect the outcome of the model significantly. Therefore, it is important to validate the model using real data.

Similar to Chapter 5, the model is assessed and the results are analysed during periods of nominal and active ionosphere. The dates for analysis are chosen based on the planetary Kp index and local geomagnetic data. The purpose of the analysis is to 1) test the feasibility of the model for Canadian polar region using real GPS data; 2) test the model under quiet and active ionospheric conditions; and 3) confirm that the $\mathrm{K}_{\mathrm{max}}$ and Q values determined in Chapter 5 are appropriate for real data. The results are validated using: 1) Radio Occultation (RO) products; and 2) tests for stability of the Inter-Frequency Biases (IFB).

6.2 Results Validation

Since a true unbiased vertical profile of the electron density cannot be achieved from external data sources, a direct comparison and validation of the reconstructed electron density profile cannot be conducted. Therefore, in order to validate the accuracy of the proposed ionospheric tomography technique with real data, two approaches are considered: 1) comparing the reconstructed electron density profile against the one estimated using radio occultation methods, and 2) checking the stability of the receivers' inter-frequency biases.

6.2.1 Radio Occultation

GPS Radio Occultation (RO) is a technique used to profile different parameters of the atmosphere, such as the free electron density. It involves a Low-Earth Orbit (LEO) satellite receiving signals from GPS satellites while orbiting the Earth. As these satellites move, the LOSs between the LEO satellites and different GPS satellites pass through different layers of the ionosphere allowing profiling of the electron density in each layer. Figure 6.1 illustrates the geometry for probing and retrieving the ionospheric parameters such as electron density profiles.

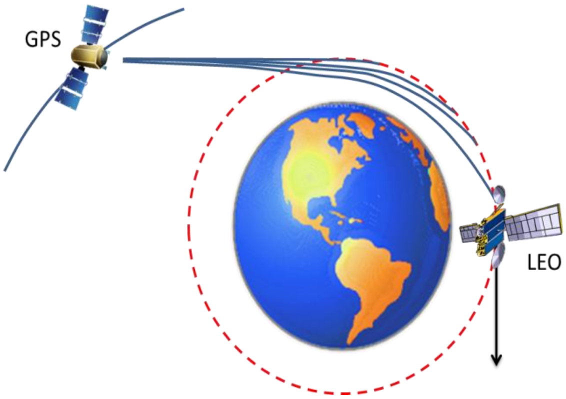

Figure 6.1: Illustration of the geometry of the GPS-LEO for ionospheric sounding.

The Constellation Observing System for the Meteorology, Ionosphere and Climate (COSMIC) is one of several radio occultation missions where the data collected by GPS receivers onboard of LEO satellites are post-processed and the electron density profiles are derived. The ionospheric profiles of electron density (ionPrf) product can be downloaded at COSMIC website with a reported accuracy of 0.1 – 1 $\times 10^{11}$ el/m^3 (“COSMIC Program Office Website”, 2013). Many authors have investigated the accuracy of electron density profile derived from radio occultation measurements: Yue et al. (2013) reported an accuracy of 0.5 $\times 10^{11}$ el/m^3 , Jakowski et al. (2005) reported a systematic positive bias in the order of less than 0.8 $\times 10^{11}$ el/m^3 and a standard deviation of 1.3 $\times 10^{11}$ el/m^3. In this research, the accuracy of 1 $\times 10^{11}$ el/m^3 reported by COSMIC Program Office Website is used as a reference of the accuracy measure of the radio occultation retrieved electron density profiles. These profiles are used to validate the electron density profiles reconstructed using the proposed ionospheric tomographic technique.

6.2.2 Stability of Receiver Inter-Frequency Biases (IFB)

STEC measurements are biased by the unknown satellite and receiver Inter-Frequency Biases (IFB). The mean values of the biases are stable over a period of one day (Sardón and Zarraoa, 1997). This information can be useful to assess the solution of the proposed technique. Since the main goal of the technique is to estimate the electron density using GPS data, it is possible to reduce the number of unknowns and eliminate the IFB using a differencing technique explained in Chapter 4. Once the electron density profiles are estimated, the residuals of Equation (4.22) can be used to estimate the IFBs as follows:

$$\overrightarrow{\boldsymbol{\delta}\mathbf{STEC}}_{\mathrm{M}\times 1} = \overrightarrow{\mathbf{STEC}}_{\boldsymbol{noisy}} - \mathbf{H}.\overrightarrow{\mathbf{N}_{\mathbf{e}}}^{\mathbf{Estimated}} \tag{6.1}$$

$$\overrightarrow{\boldsymbol{\delta STEC}}_{\mathrm{M}\times 1} = \mathbf{F}_{\mathrm{M}\times(\mathrm{N}+\mathrm{P})} . \vec{\mathbf{Y}}_{(\mathrm{N}+\mathrm{P})\times 1} \tag{6.2}$$

where M, N, and P are the number of measurements, number of receivers, and number of satellites used in the inversion, respectively. $\vec{\mathbf{Y}}$ is a vector of the receiver and satellite inter-frequency biases in units of TECU:

$$\vec{\mathbf{Y}}_{(\mathrm{N}+\mathrm{P})\times 1} = \begin{bmatrix} \mathrm{IFB}_{\mathrm{Rec1}} \\ \mathrm{IFB}_{\mathrm{Rec2}} \\ \vdots \\ \mathrm{IFB}_{\mathrm{RecN}} \\ \mathrm{IFB}_{\mathrm{Sat1}} \\ \mathrm{IFB}_{\mathrm{Sat2}} \\ \vdots \\ \mathrm{IFB}_{\mathrm{SatP}} \end{bmatrix} \tag{6.3}$$

The design matrix **F** is defined as:

$$\mathrm{F}_{kq}(\mathrm{i},\mathrm{j}) = \begin{cases} 1 & q = i \text{ or } q = N + j \\ 0 & \text{otherwise} \end{cases} \tag{6.4}$$

where k = 1,2, … M, and q = 1,2,… (N+P), and i and j are the receiver and satellite indices used to derive the k^{th} δSTEC measurement, respectively. For example, if N = 39 receivers and P = 10 satellites are used, then the k^{th} row of the design matrix **F** corresponding to a measurement derived using receiver i = 2 and satellite j = 2 is

$$\mathrm{F}_k(2,2) = [\underbrace{0 \quad 1 \quad 0 \quad \cdots \quad 0}_{1\times\mathrm{N}} \qquad \underbrace{0 \quad 1 \quad 0 \quad \cdots \quad 0}_{1\times\mathrm{P}}] \tag{6.5}$$

In order to estimate the receiver and satellite inter-frequency biases, a reference (pseudo-measurement) has to be introduced. This is due to the fact that the biases are relative values. One approach, used by Jet Propulsion Laboratory (JPL), is to assume that the sum of all satellite inter-frequency biases should be equal to zero. JPL estimates vertical TEC spatially and the inter-frequency biases using stations over the globe, allowing them to observe all operational GPS satellites. In this research, only the observations with LOS within the defined model space are considered, where the LOS associated with each observation must enter the grid from the bottom of the lowest layer and exit through the top of the highest layer as demonstrated in Chapter 4. This results in a lower number of satellites available for analysis compared to JPL. Therefore, another approach is adopted in this work where the summation of the satellites' inter-frequency biases is forced to be equal to the summation of the receiver inter-frequency biases. This will yield a different solution than JPL's (where the receiver inter-frequency biases absorb part of the satellite inter-frequency biases). To eliminate this effect, the inter-frequency biases of two receivers are differenced and the results are compared based on the relative inter-frequency biases between different sites.

Applying the aforementioned approach results in a measurement vector with one more element than the original observed $\overrightarrow{\boldsymbol{\delta STEC}}$**:**

$$\overrightarrow{\boldsymbol{\delta STEC}}_{(\mathrm{M}+1)\times 1} = \begin{bmatrix} \delta\mathrm{STEC}_1 \\ \delta\mathrm{STEC}_2 \\ \vdots \\ \delta\mathrm{STEC}_M \\ 0 \end{bmatrix} \tag{6.6}$$

and a design matrix **F** with one more row:

$$\mathrm{F}_{(M+1)\times(N+P)} = [\underbrace{1 \quad 1 \quad 1 \quad \cdots \quad 1}_{1\times\mathrm{N}} \quad \underbrace{-1 \quad -1 \quad -1 \quad \cdots \quad -1}_{1\times\mathrm{P}}] \tag{6.7}$$

The inter-frequency biases are then estimated using the weighted least squares method described in Chapter 4.

6.3 Data Description and Analysis Strategy

The GPS reference stations from CHAIN Network and the International GNSS Service (IGS) are selected to assess the tomographic technique over Canadian polar region. The stations names and geographic locations are listed in Table (5.1). Two types of STEC measurements are derived from dual frequency GPS data: code-derived STEC and phase-derived STEC. The phase-derived STEC is corrected for cycle slips, if possible, and then used to smooth the noisy code-derived STEC, as described in Chapter 4. These measurements are used as input for the CIT model.

The developed CIT model estimates the electron density profiles and generates vertical TEC maps using settings listed in Table 6.1, where one-hour data sets over a period of twenty four hours of GPS data are processed. The results are then validated against the ionospheric profiles of electron density generated by COSMIC Data Analysis and Archive Center (CDAAC) using the radio occultation approach.

Table 6.1: Model settings

	Nominal conditions
Region boundaries	**ϕ = 45° N – 80° N** **λ = 240° E – 304° E** **height = 80 km – 1180 km**
Voxel spacing ($\Delta\phi \times \Delta\lambda \times \Delta$height)	**1° × 4° × 25km**
Duration	**60 minutes**
Data sampling rate	**Sample per 120 seconds**
Cut-off angle	**15°**
SCH pole	**62.5° N and 272° E**
SCH half-angle θ_o	**27.5°**

Once the electron density distribution is estimated, the satellite and receiver inter-frequency biases are estimated using the approach explained in the previous section. The stability of the receiver inter-frequency biases, represented by the standard deviation, is analysed and a comparison with a third party product, i.e. JPL, is conducted.

6.4 Constraining the Ionospheric Tomography Problem

The advantages of the proposed CIT technique have been discussed in Chapters 4 and 5. The low number of required unknowns to represent the electron density profile and the low memory and computation load using this technique make it a potential candidate as a tool for regional ionospheric imaging. However, the ionospheric tomography technique is ill-conditioned and singular. The design matrix is affected by small errors and the occurrence of outliers could affect the solution significantly. An example of such an error is an undetected cycle slip. In addition to the errors and outliers, the geometry plays an important role in achieving a reliable and realistic solution. A realistic solution is an electron density profile that behaves as a Chapman-like profile with all values being positive. Since ground-based GPS measurements are only used in this technique, the orientation of the LOSs and the lengths of the rays intersecting certain voxels might not be sufficient to derive any useful information. The network of GPS receivers used in this work is sparse and a large number of voxels are not illuminated at all. The aforementioned points will affect the stability and robustness of the technique.

GPS signals are of sufficiently high strength to be tracked using commercial GPS receivers. Visibility is a major concern for implementing ionospheric tomography. The higher the number of visible satellites, the more LOS will illuminate different voxels. However, having many LOS intersecting each voxel is not enough to successfully conduct the tomographic inversion. The orientations of these LOS are also important. In some cases, the orientations and lengths of these rays in each voxel are too similar to reflect any new information about these voxels (LOS 1 and LOS 2 for example in Figure 6.2). For a ray to carry sufficient information about a voxel, a certain minimum length of that ray must illuminate that voxel with an orientation and lengths that are different from other rays intersecting the same voxel, as in the case of LOS 3 and LOS 1 in Figure 6.2.

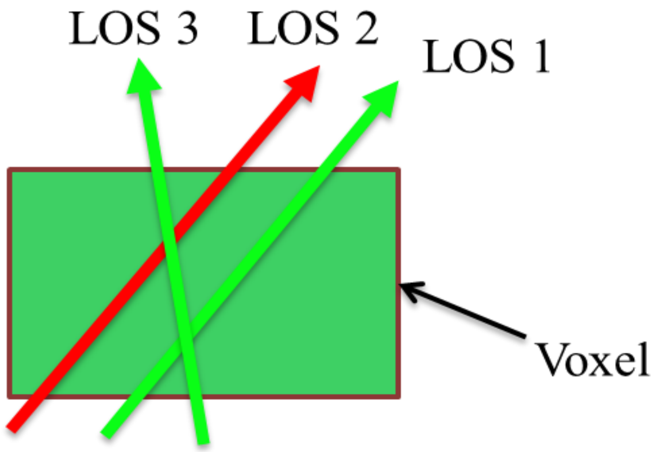

Figure 6.2: Illustration of the effect of orientation on geometry

Using an extra constraint is one approach to overcome these limitations, where the constraint will force the electron density distribution to follow a realistic profile. This can be achieved through the use of empirical orthogonal functions. As explained previously, the first EOF represents the mean value of the electron density profile and the other EOFs describe the deviation from that mean. Using the First EOF to define the ionosphere, the solution, i.e. coefficients, are constrained using an initial value for the coefficient (a_{01}^{0} of Equation(4.44)) corresponding to the first EOF and the variance-covariance matrix ($\boldsymbol{P_m}$) of the initial parameter. Setting $\overrightarrow{\mathbf{m_0}}$ and $\boldsymbol{P_m}$ as follows:

$$\overrightarrow{\mathbf{m_0}} = \begin{bmatrix} a_{01}^{0} \\ 0 \\ \vdots \\ 0 \end{bmatrix}_{Q\times(K_{max}+1)^2} \tag{6.8}$$

$$\boldsymbol{P_m} = \begin{bmatrix} 0 & 0 & 0 & 0 \\ 0 & 1 & 0 & 0 \\ 0 & 0 & \ddots & 0 \\ 0 & 0 & 0 & 1 \end{bmatrix}_{Q\times(K_{max}+1)^2} \tag{6.9}$$

the generalized Tikhonov solution can be expressed as follows:

$$\hat{\mathbf{m}} = \overrightarrow{\mathbf{m_0}} + (\mathbf{G^T P_d G} + \alpha^2 \mathbf{P_m})^{-1} \mathbf{G^T P_d}(\vec{\mathbf{d}} - \mathbf{G} \cdot \vec{\mathbf{m}}) \tag{6.10}$$

where the regularization parameter (α) is selected using the technique explained in Chapter 4. The initial coefficient a_{01}^{0} is determined using a background ionosphere such as the IRI model. Setting the variance of a_{01}^{0} to zero gives the coefficient the freedom to best fit the measurements but maintain a Chapman-like profile. Figure 6.3 shows the improvement of the solution achieved by constraining a_{01}^{0}. In the figure, each voxel is assigned a unique number represented by “Voxel ID”. The red dashed line represents the start of a horizontal layer at a different altitude. For example, the regions between the first and second lines and between the second and third lines describe the electron density distribution horizontally at 117.5 km and 142.5 km, respectively. It is clear that applying the constraint helps in shaping the reconstructed electron density profile. The values of electron density distribution are positive and follow a Chapman-like profile where the height of the electron density peak is in the F-region, as expected. The real data results represented in this Chapter are generated by constraining a_{01}^{0}.

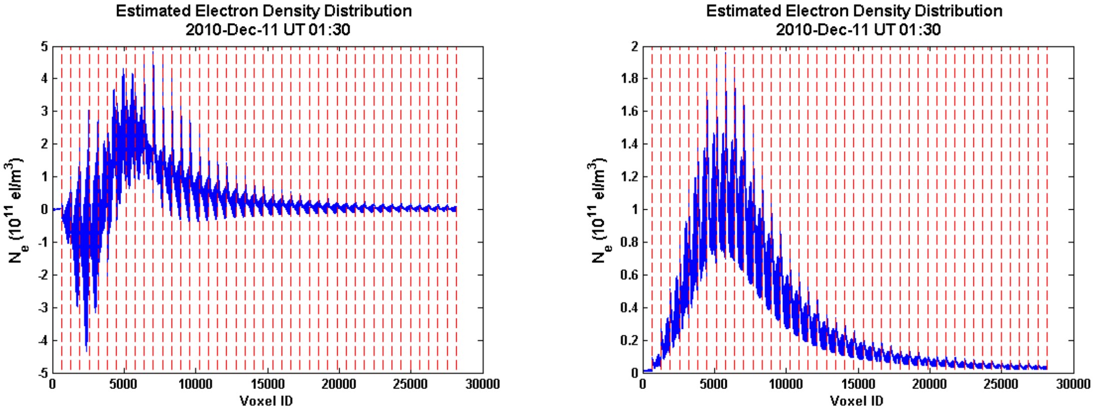

Figure 6.3: Estimated electron density profile before (left) and after (right) applying a_{01}^{0} constraint.

6.5 Data Analysis and Results

As in Chapter 5, the model is tested under nominal and active ionospheric conditions using real GPS data. The data analysis results of processing GPS data for different sample days are presented below. The dates were chosen based on the level of geomagnetic activity. For each day, the one-hour GPS data sets over a period of one day are processed, where the electron density profiles along different longitudes and TEC maps over time are estimated and presented. The electron density profiles are validated against RO derived profiles and the satellite and receiver inter-frequency biases are computed and their stability over the hours of the day is checked.

6.5.1 Nominal Ionospheric Conditions

The geomagnetic activities on January 16, 2010, May 01, 2010 and December 11, 2010 are shown in Figure 6.4. The activities are represented by a set of Kp indices. The Kp index is a global indicator that reflects the geomagnetic activity level in a given three-hour time interval (Gonzalez et al., 1994). It is derived using globally distributed (in longitude) sub-auroral ground-based magnetometers. Kp indices range from 0 to 9. A Kp index can be interpreted as follows: a value less than 4 indicates a low level of ionospheric activity, a value of 4 indicates a moderate ionospheric level, and a value of 5 or greater indicates a storm level of geomagnetic activity; however such values must be interpreted carefully since they reflect the global level of geomagnetic activity but do not specify the region of high activity. As seen in the Figure, the Kp index for the three selected dates ranges from 0 to 2 indicating a quiet nominal ionosphere.

The CIT-estimated vertical TEC maps for these dates are presented in Figure 6.5, Figure 6.6, and Figure 6.7. The vertical TEC maps are obtained by integrating through the CIT-estimated electron density profiles as described in Section 5.5. As expected, the results follow the expected diurnal variation of TEC values with low values during nighttime and high values at the middle of the day. The corresponding Root Mean Square (RMS) of the residuals is listed in Table 6.2. The RMS increases for local times closer to the midday maximum peak (~20:30 UT). However, the errors are no worse than ~2.5 TECU.

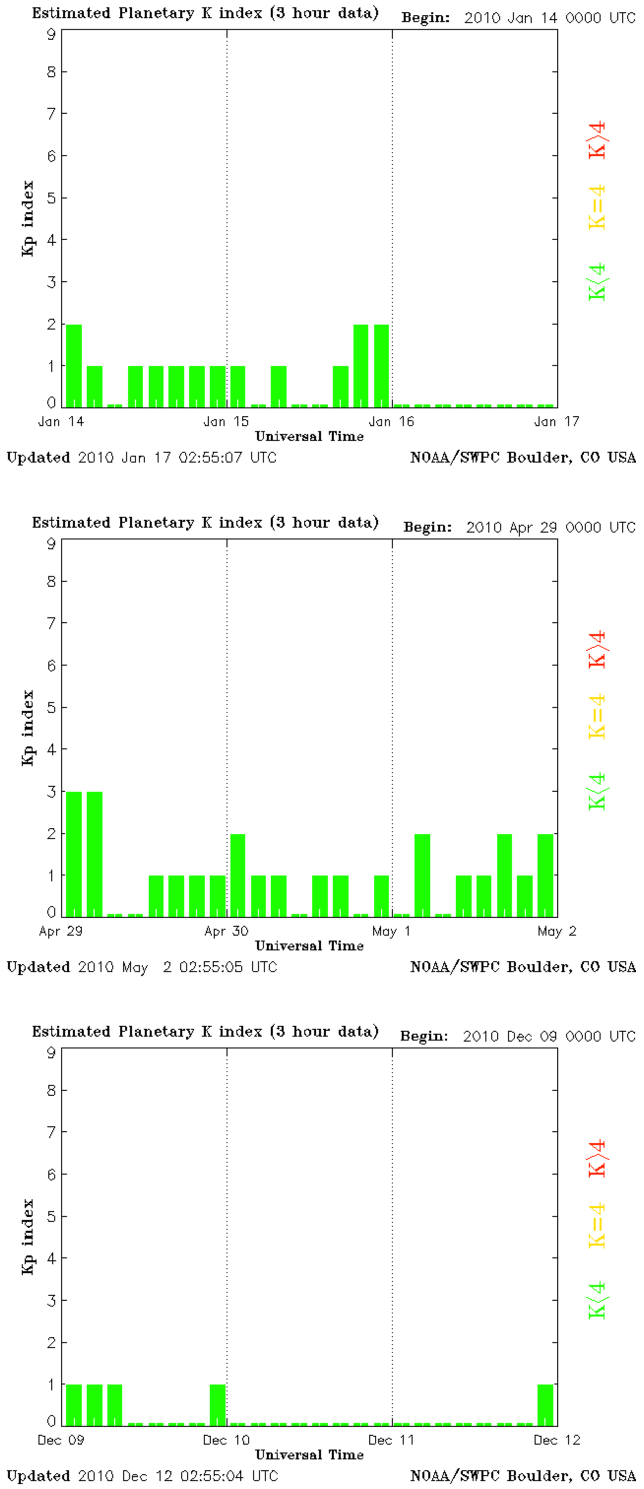

Figure 6.4: Planetary Kp indices for 16 January 2010 (top), 01 May 2010 (middle), and 11 December 2010 (bottom) (http://www.swpc.noaa.gov/ftpmenu/warehouse/2011/2011_plots.html, April 2013)

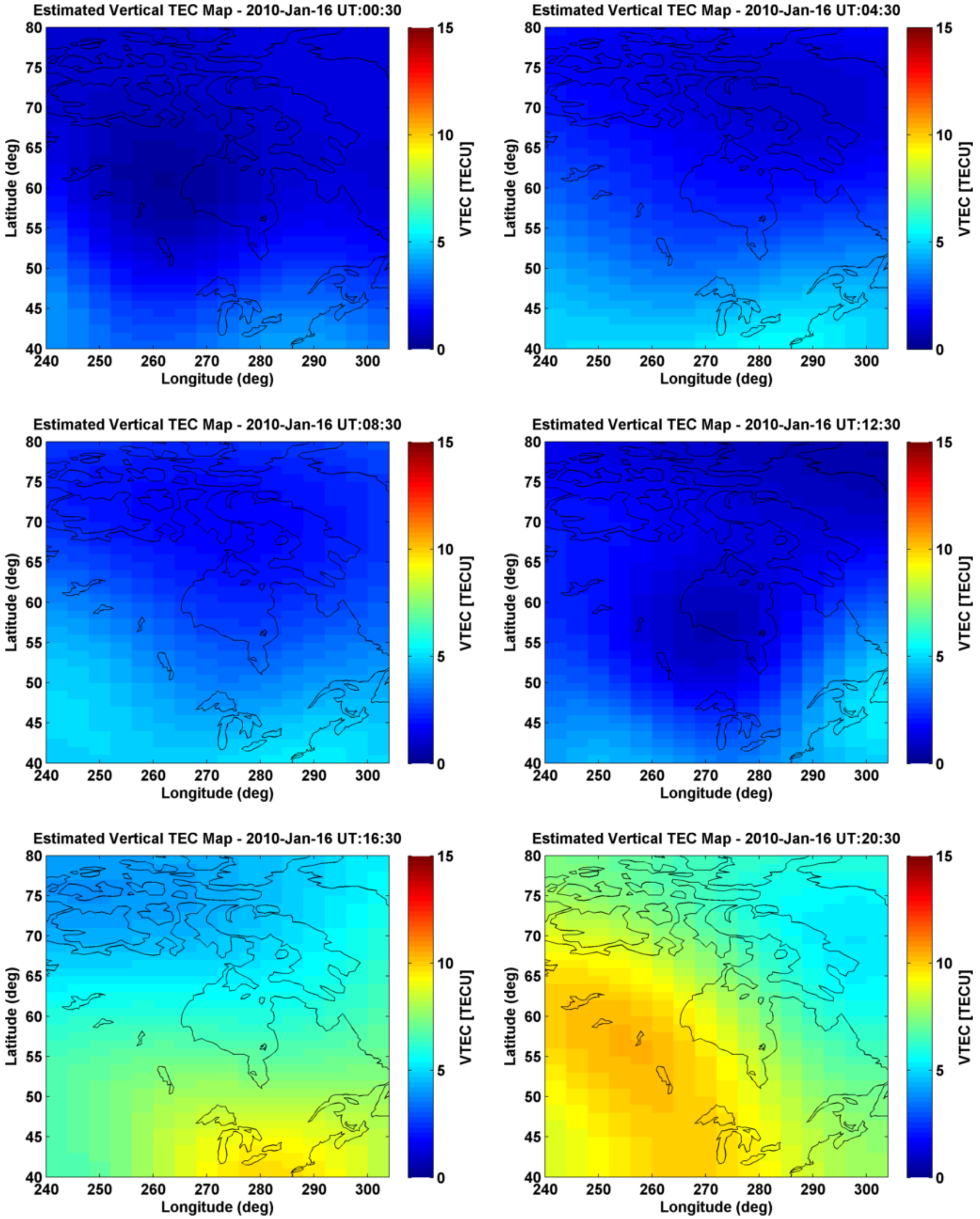

Figure 6.5: Estimated vertical TEC maps for 16 January 2010 (K_{max} =3 and Q = 3)

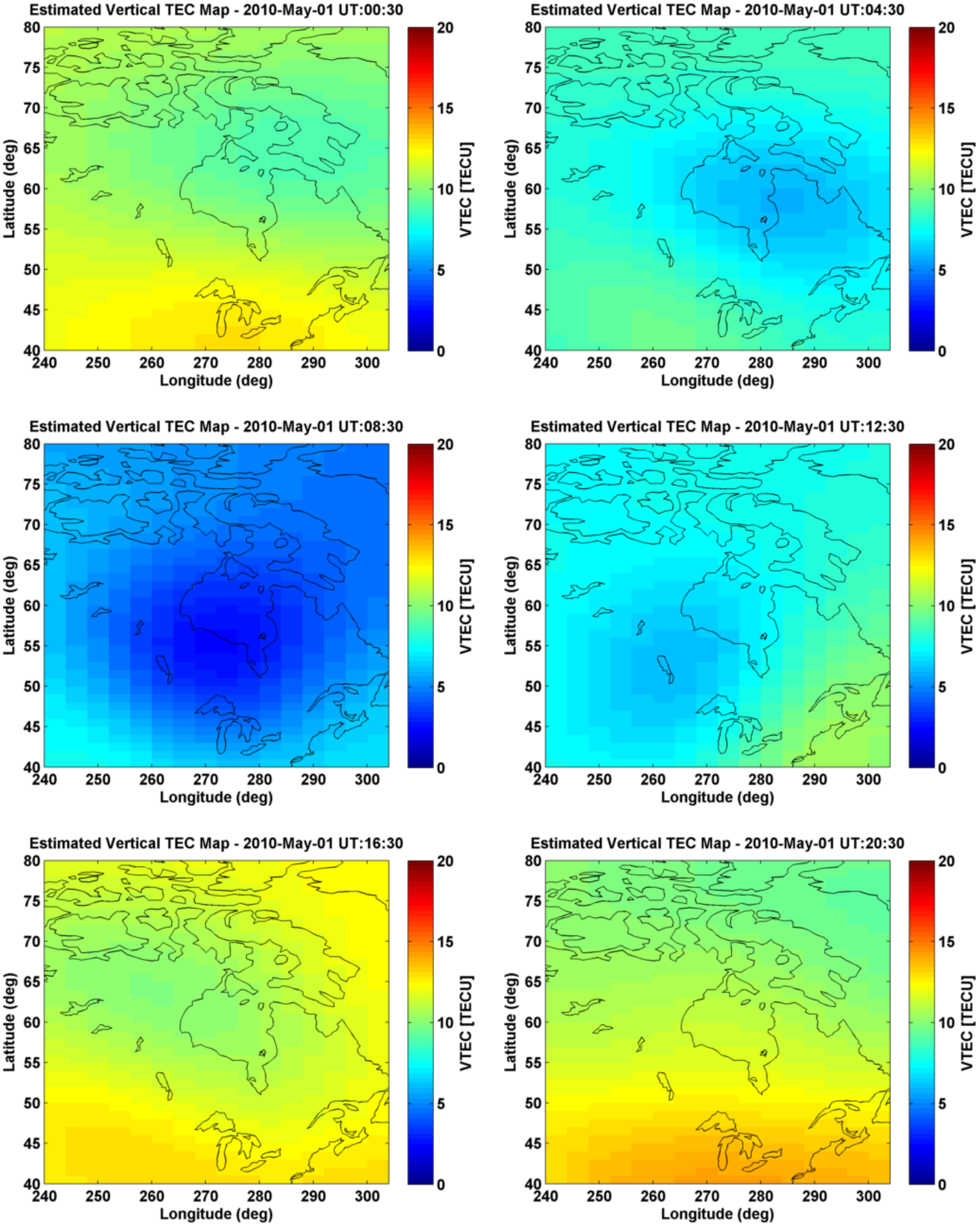

Figure 6.6: Estimated vertical TEC maps for 01 May 2010 (K_{max} =3 and Q = 3)

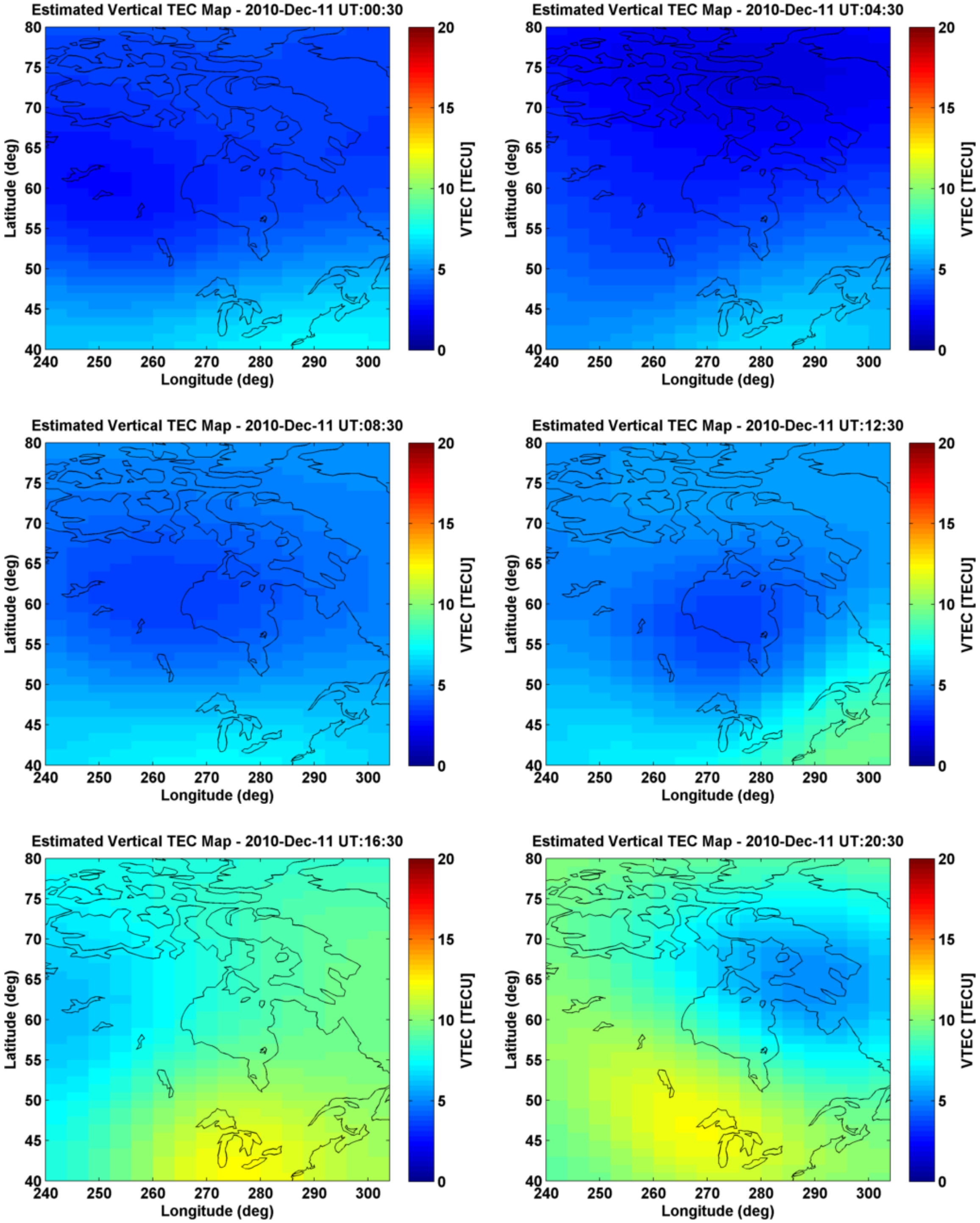

Figure 6.7: Estimated vertical TEC maps for 11 December 2010 (K_{max} =3 and Q = 3)

Table 6.2: Root mean square of the residuals in TECU (K_{max} =3 and Q = 3)

UTC	16 January 2010	01 May 2010	11 December 2010
00:30	1.19	2.00	1.70
04:30	1.87	1.86	1.85
08:30	1.89	1.37	1.70
12:30	1.67	1.89	1.91
16:30	1.75	1.47	1.68
20:30	2.07	2.39	1.93

6.5.1.1 Inter-Frequency Bias Stability

To conduct a quantitative assessment, the reconstruction result is first validated by examining the relative inter-frequency receiver biases. Figure 6.8 shows a comparison of relative biases of JPL versus the proposed technique for six IGS sites: ALGO, DRAO, CHUR, PRDS, HOLM and YELL. The JPL relative inter-frequency receiver biases between DRAO and ALGO, CHUR and ALGO, and CHUR and DRAO are –5.67 m, -3.54 m and -2.13 m, respectively. The JPL relative inter-frequency receiver biases between YELL and HOLM, PRDS and HOLM, and PRDS and YELL are –3.14 m, -1.14 m and -2.00 m, respectively. Comparing these values to the proposed technique estimates, the receiver inter-frequency biases are consistent within 1.5 TECU (~24 cm).

The mean value of inter-frequency receiver biases is expected to be stable over the day on an hour-to-hour basis. Therefore, this property can be used to determine accuracy of the ionosphere reconstruction using the proposed technique. Processing one-hour data sets over a period of twenty four hours, a measure of the stability can be computed by estimating the mean of the inter-frequency receiver biases and their corresponding standard deviations. Table 6.3 shows the biases and their standard deviation over the twenty four-hour period. As expected, a stable solution is estimated with a standard deviation less than ~ 60 cm (3.8 TECU).

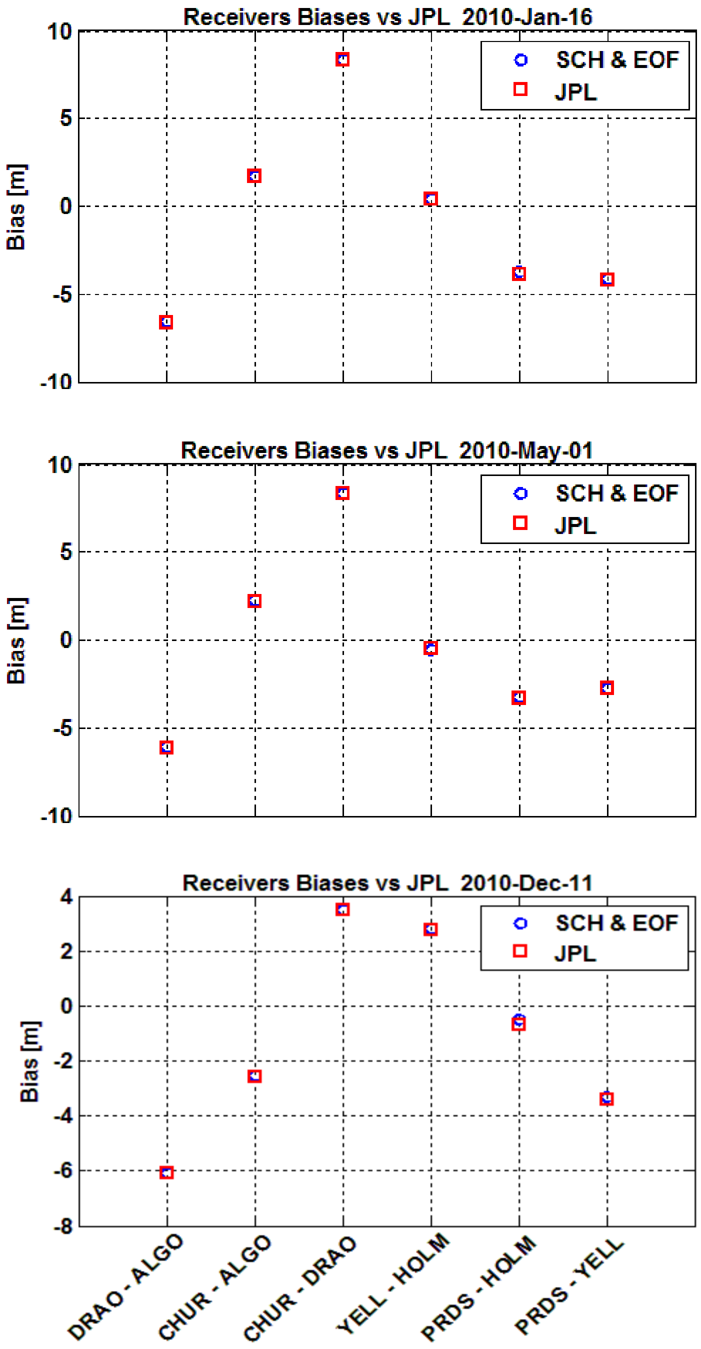

Figure 6.8: Relative receiver inter-frequency biases for 16 January 2010 (top), 01 May 2010 (middle), and 11 December 2010 (bottom) (K_{max} =3 and Q = 3)

Table 6.3: Estimated inter-frequency receiver biases (K_{max} =3 and Q = 3)

Station	16 January 2010		01 May 2010		11 December 2010	
	IFB [m]	Std [m]	IFB [m]	Std [m]	IFB [m]	Std [m]
ALGO	**-2.43**	**0.43**	**-3.34**	**0.33**	**-2.83**	**0.26**
BAKE	**-3.18**	**0.35**	**-3.60**	**0.20**	**-3.22**	**0.20**
BREW	**-0.24**	**0.43**	**-0.73**	**0.32**	**-0.17**	**0.22**
CAGS	**2.48**	**0.40**	**2.22**	**0.24**	**2.67**	**0.21**
CHUR	**-0.73**	**0.38**	**-1.08**	**0.18**	**-5.35**	**0.17**
DRAO	**-8.91**	**0.45**	**-9.30**	**0.34**	**-8.82**	**0.26**
ESCU	**0.89**	**0.46**	**0.63**	**0.21**	**1.11**	**0.28**
HLFX	**-6.67**	**0.53**	**-5.65**	**0.25**	**-3.89**	**0.24**
HOLM	**1.70**	**0.39**	**1.22**	**0.17**	**-5.04**	**0.33**
KUUJ	**-4.98**	**0.39**	**-5.07**	**0.26**	**-1.85**	**0.38**
NAIN	**0.59**	**0.41**	**0.16**	**0.25**	**-3.39**	**0.24**
NRC1	**5.79**	**0.51**	**5.42**	**0.47**	**0.62**	**0.27**
PICL	**-6.22**	**0.37**	**-6.55**	**0.23**	**7.41**	**0.41**
PRDS	**-1.97**	**0.47**	**-2.00**	**0.34**	**-6.47**	**0.18**
QIKI	**0.36**	**0.39**	**-0.12**	**0.27**	**-2.33**	**0.32**
RESO	**-1.32**	**0.37**	**-1.35**	**0.22**	**0.43**	**0.31**
SASK	**1.39**	**0.38**	**0.95**	**0.24**	**-1.23**	**0.31**
SCH2	**-4.82**	**0.41**	**-5.23**	**0.22**	**1.52**	**0.17**
SHE2	**1.79**	**0.43**	**1.42**	**0.28**	**-4.73**	**0.24**
UNBJ	**0.28**	**0.46**	**-0.02**	**0.26**	**0.92**	**0.28**
VALD	**-3.37**	**0.40**	**-4.31**	**0.21**	**0.56**	**0.29**
WILL	**-7.42**	**0.60**	**-7.97**	**0.52**	**-4.49**	**0.19**
YELL	**2.09**	**0.40**	**0.70**	**0.15**	**-7.52**	**0.43**
CBBC	**5.09**	**0.40**	**4.45**	**0.21**	**0.92**	**0.21**
EDMC	**4.56**	**0.44**	**4.19**	**0.27**	**5.15**	**0.25**
EURC	**4.97**	**0.49**	**4.99**	**0.43**	**4.58**	**0.31**
HALC	**5.08**	**0.35**	**4.94**	**0.26**	**4.78**	**0.36**
IQAC	**5.37**	**0.34**	**5.10**	**0.28**	**5.71**	**0.19**
PONC	**4.94**	**0.36**	**4.71**	**0.28**	**5.08**	**0.22**
QIKC	**3.28**	**0.37**	**2.78**	**0.36**	**3.29**	**0.22**
RESC	**4.58**	**0.40**	**4.49**	**0.36**	**4.52**	**0.28**
SANC	**4.59**	**0.35**	**4.22**	**0.26**	**4.67**	**0.18**
TALC	**4.70**	**0.35**	**4.49**	**0.20**	**4.65**	**0.25**

6.5.1.2 Electron Density Profile Comparisons

The proposed CIT method estimates the electron density profile using GPS observations. To further evaluate the performance of the method, radio occultation can be utilized and the CIT derived electron density profile is compared to the one derived using radio occultation measurements. Figure 6.9, Figure 6.10, and Figure 6.11 show four radio occultation events at different hours of the day. Each plot consists of three subplots. The top left subplot shows the geographical latitude and longitude of the perigee points. The green and red circles represent the geographical horizontal coordinates of the first and last perigee points, respectively. The bottom left subplot compares the electron density profiles derived using radio occultation (red) and tomographic technique (blue). The subplot on the right shows the difference between the two derived profiles. The red dotted line represent the accuracy range ($\pm 1 \times 10^{11}$ el/m^3) of the radio occultation derived electron density profile, as stated earlier in this Chapter.

The CIT derived electron density is defined at the centre of each voxel. To better compare and validate the results, CIT derived profiles are interpolated and the electron density profiles are computed at the geographical coordinates of the radio occultation perigee points. The error statistics of a full day of radio occultation events are summarized in Table 6.4. It is found that the CIT derived profile are biased by -0.3×10^{11} el/m^3 with an overall RMS of ~0.5×10^{11} el/m^3, which is within the range of the radio occultation accuracy. For completeness, the mean and RMS of the errors for all available occultation events for the selected dates are listed in Tables 6.5, 6.6, and 6.7.

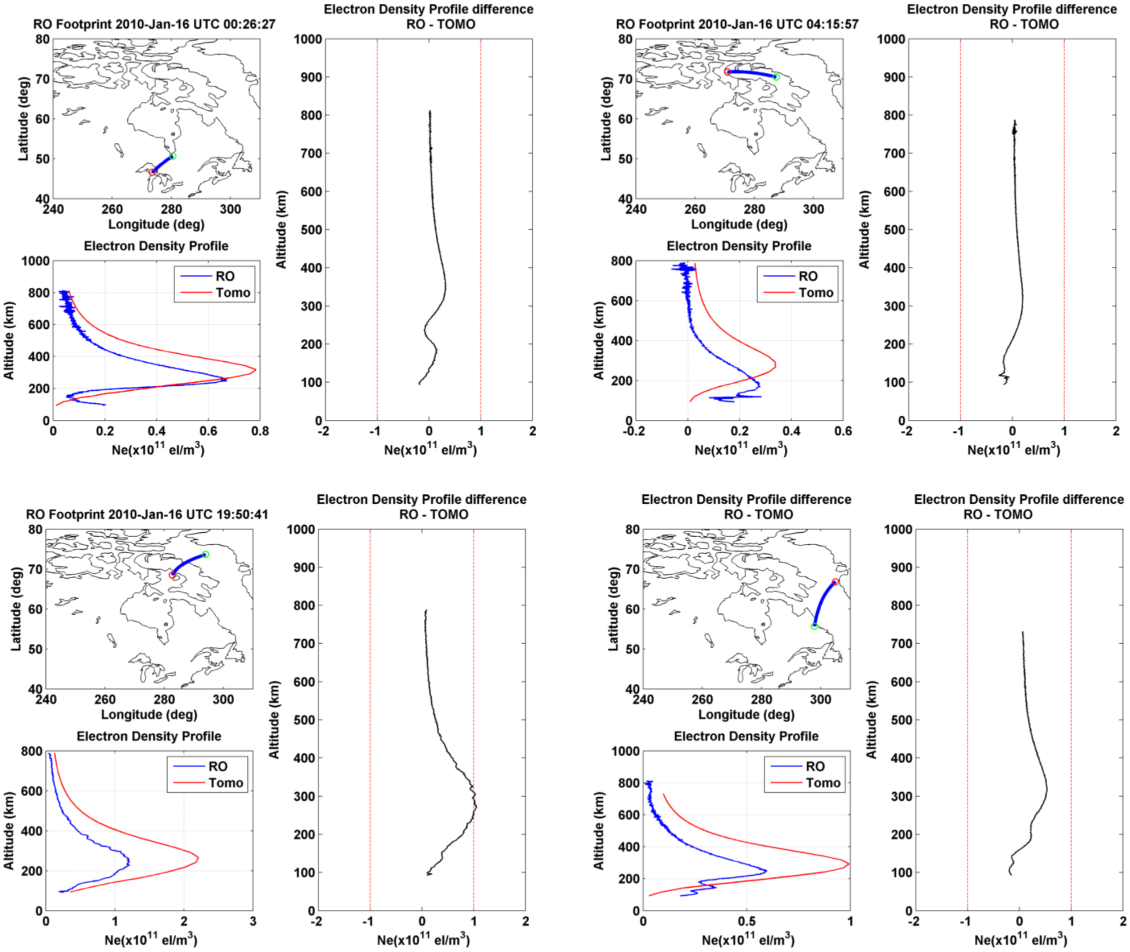

Figure 6.9: Radio occultation (RO) vs. tomography (TOMO) electron density profiles for 16 January 2010

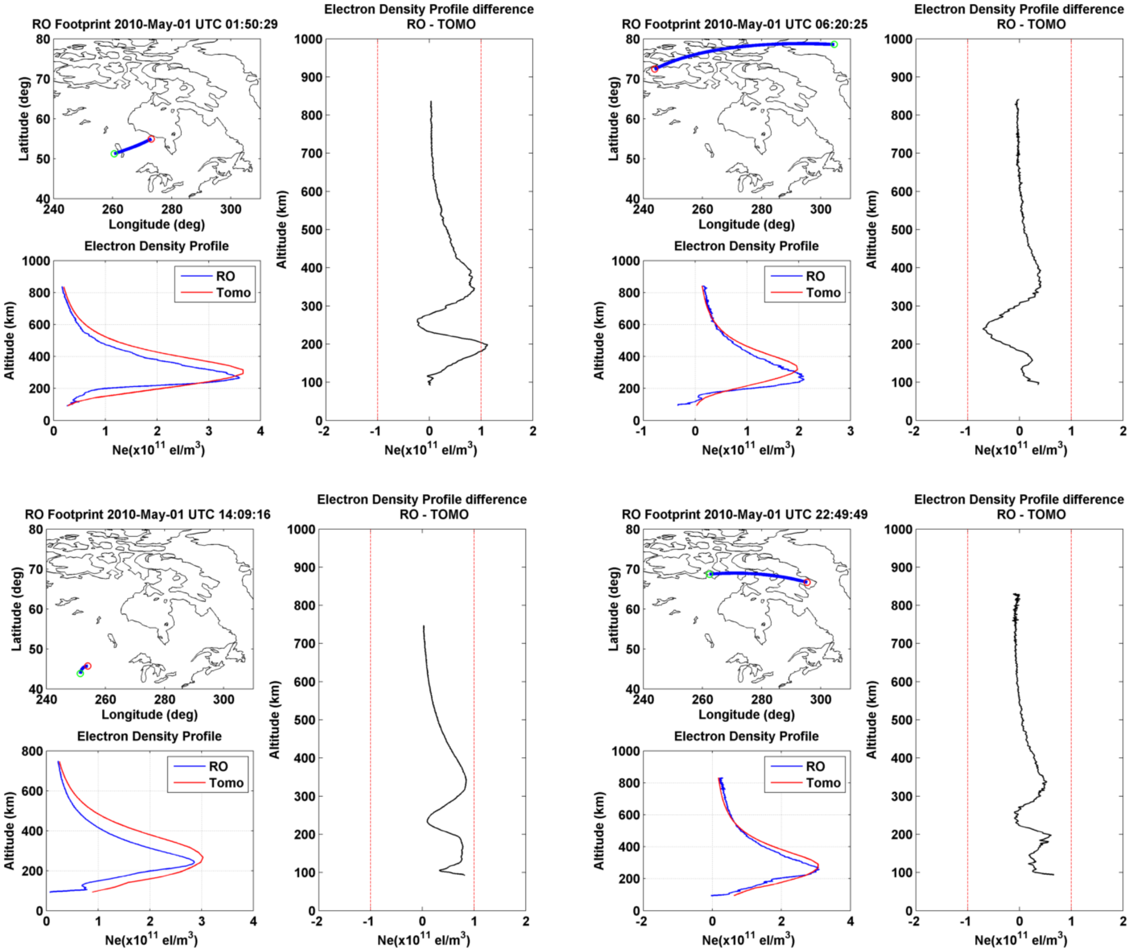

Figure 6.10: Radio occultation (RO) vs. tomography (TOMO) electron density profiles for 01 May 2010

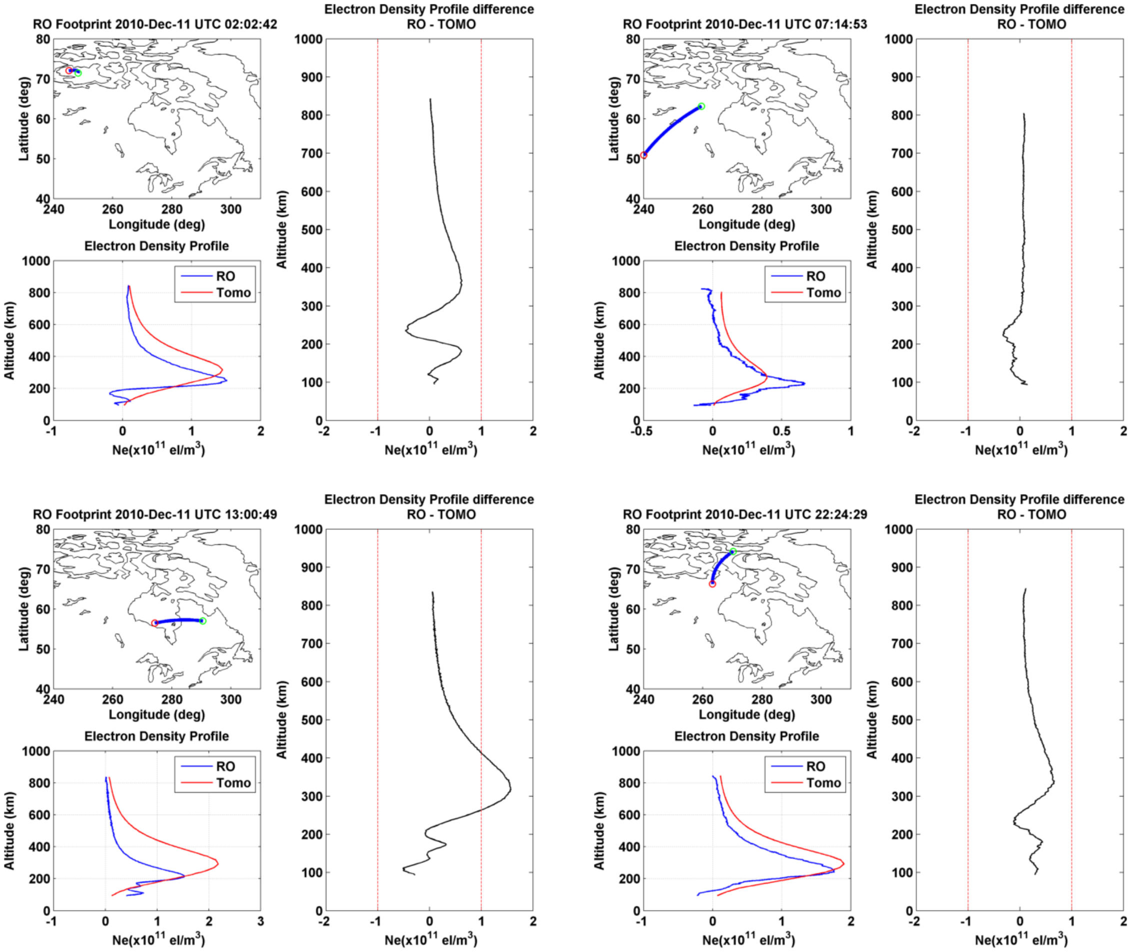

Figure 6.11: Radio occultation (RO) vs. tomography (TOMO) electron density profiles for 11 December 2010

Table 6.4: Summary of the statistics of the difference between the electron density profiles derived by radio occultation vs. CIT (K_{max} =3 and Q = 3)

Date	RMSE (10^{11} el/m^3)	Mean (10^{11} el/m^3)
16 January 2010	0.36	-0.20
01 May 2010	0.44	-0.29
11 December 2010	0.39	-0.26

Table 6.5: Statistics of the difference between the electron density profiles derived by radio occultation vs. CIT for 16 January 2010 (K_{max} =3 and Q = 3)

UTC	RMSE (10^{11} el/m^3)	Mean (10^{11} el/m^3)	UTC	RMSE (10^{11} el/m^3)	Mean (10^{11} el/m^3)
00:06:48	0.33	-0.14	07:45:57	0.48	0.31
00:13:34	0.15	0.09	07:46:35	0.48	0.36
00:26:27	0.14	0.09	08:03:40	0.70	0.60
00:26:31	0.37	-0.21	08:07:29	0.68	0.55
00:27:13	0.37	-0.22	09:45:15	0.39	0.29
01:09:27	0.12	0.06	09:46:23	0.28	0.17
01:09:46	0.10	0.09	09:49:16	0.17	0.08
01:25:26	0.14	0.07	11:01:20	0.48	0.21
01:25:58	0.09	0.06	11:36:37	0.63	0.49
01:33:35	0.62	0.47	13:04:45	0.58	0.49
01:33:59	0.71	0.57	13:16:01	0.66	0.53
02:06:08	0.08	0.07	13:17:16	0.59	0.36
02:14:33	0.06	0.06	14:53:09	0.29	0.23
02:15:36	0.07	0.07	14:57:36	0.63	0.39
02:54:03	0.22	0.18	15:01:39	0.27	0.19
02:58:39	0.05	0.05	16:07:04	0.55	0.18
02:59:10	0.50	0.34	16:40:13	0.53	0.19
03:10:58	0.09	0.04	17:48:04	0.64	0.20
03:12:49	0.18	0.12	17:52:54	0.69	0.60
03:16:38	0.03	-0.02	18:02:32	0.50	0.18
03:54:01	0.09	0.06	18:06:07	0.66	0.48
03:56:41	0.10	0.09	18:11:46	0.15	0.15
04:15:57	0.11	0.06	18:33:30	0.70	0.52
04:42:26	0.45	0.30	19:29:12	0.58	0.35
04:42:46	0.46	0.35	19:30:19	0.56	0.37
04:42:46	0.40	0.31	19:33:43	0.49	0.35
04:48:26	0.19	0.15	19:40:41	0.09	0.08
04:54:46	0.36	0.26	19:42:55	0.45	0.14
04:55:20	0.46	0.33	19:44:01	0.44	0.23
05:44:40	0.21	0.09	19:50:41	0.49	0.37
05:59:29	0.32	-0.07	19:56:34	0.90	0.72
06:01:40	0.11	0.10	20:15:32	0.34	0.13
06:02:27	0.18	0.16	20:36:55	0.49	0.26
06:03:26	0.41	0.30	20:54:50	0.12	0.12
06:19:40	0.22	0.16	21:12:55	0.80	0.50
06:22:53	0.43	0.28	21:13:16	0.59	0.36
06:23:08	0.44	0.34	21:17:38	0.45	0.31
06:23:30	0.46	0.35	21:18:15	0.50	0.36
06:24:22	0.49	0.37	21:19:05	0.77	0.58
06:25:48	0.08	-0.08	21:22:11	0.20	0.20
07:21:42	0.16	0.10	21:31:17	0.96	0.71
07:28:13	0.51	0.40	21:31:17	0.63	0.50

Table 6.6: Statistics of the difference between the electron density profiles derived by radio occultation vs. CIT for 01 May 2010 (K_{max} =3 and Q = 3)

UTC	RMSE (10^{11} el/m^3)	Mean (10^{11} el/m^3)	UTC	RMSE (10^{11} el/m^3)	Mean (10^{11} el/m^3)
01:10:04	0.05	-0.05	08:07:16	0.24	0.17
01:11:13	0.38	0.23	09:44:33	0.27	0.22
01:50:29	0.39	0.26	09:54:16	0.13	0.11
02:06:17	0.41	0.04	10:47:49	0.25	0.01
02:40:16	0.07	-0.07	10:50:01	0.28	-0.18
02:51:24	0.81	0.66	12:47:55	0.16	0.09
02:54:28	0.28	0.09	14:09:16	0.44	0.35
04:25:11	0.14	0.13	14:12:58	0.20	0.12
04:28:02	0.46	0.33	14:14:57	0.32	0.24
04:36:11	0.50	0.37	14:16:14	0.25	-0.05
04:39:12	0.41	0.25	14:16:31	0.41	0.23
05:35:39	0.27	-0.03	16:39:38	0.46	0.21
05:40:24	0.38	0.29	17:35:41	0.33	0.05
05:50:34	0.33	0.22	17:47:04	0.81	0.10
05:53:40	0.08	0.07	18:19:07	0.04	0.03
06:20:00	0.62	0.56	19:28:34	0.55	-0.27
06:20:25	0.21	0.02	19:30:39	0.30	-0.05
06:23:01	0.52	0.42	21:02:08	0.04	0.00
06:24:49	0.40	0.25	21:02:44	0.34	0.04
06:27:27	0.38	0.22	21:04:28	0.02	0.01
06:31:33	0.07	0.07	22:33:20	0.57	0.52
07:16:25	0.05	-0.05	22:42:49	0.22	0.11
07:40:53	0.03	0.03	22:49:45	0.01	-0.01
07:43:24	0.22	0.17	22:49:49	0.21	0.08
07:43:44	0.42	0.42	22:57:33	0.53	0.19
07:54:20	0.33	0.15	23:00:35	0.56	0.37
08:02:05	1.01	0.93	23:03:02	0.60	0.41
08:07:13	0.74	0.70	23:09:27	0.11	0.09

Table 6.7: Statistics of the difference between the electron density profiles derived by radio occultation vs. CIT for 11 December 2010 (K_{max} =3 and Q = 3)

UTC	RMSE (10^{11} el/m^3)	Mean (10^{11} el/m^3)	UTC	RMSE (10^{11} el/m^3)	Mean (10^{11} el/m^3)
01:17:05	0.07	0.06	07:48:50	0.35	0.26
02:02:42	0.30	0.19	07:49:50	0.04	0.04
02:13:26	0.96	0.80	07:50:39	0.11	0.11
02:14:14	0.86	0.73	09:15:05	0.20	0.19
02:20:38	0.27	0.18	09:22:09	0.47	-0.47
02:21:47	0.25	0.17	09:27:06	0.64	0.47
03:49:12	0.58	0.40	12:50:09	0.77	0.45
03:56:21	0.21	0.20	12:59:51	0.39	0.18
04:00:40	0.54	0.45	13:00:49	0.63	0.40
04:06:32	0.42	0.24	13:05:08	0.79	0.58
04:10:24	0.02	-0.02	13:06:02	0.16	0.16
05:47:48	0.42	0.29	16:24:48	0.82	0.35
05:46:03	0.52	0.37	17:12:17	1.38	0.95
05:51:09	0.03	0.01	20:22:21	0.71	0.37
05:46:28	0.17	0.15	20:35:27	0.74	0.42
05:48:47	0.36	0.27	20:37:28	0.82	0.44
05:58:05	0.64	0.49	20:40:25	0.29	0.09
05:59:23	0.48	0.35	20:43:18	0.05	0.04
07:14:53	0.10	0.03	22:03:24	1.15	0.25
07:16:24	0.16	0.09	22:12:20	0.39	0.22
07:32:01	0.17	0.12	22:20:54	0.52	0.27
07:33:16	0.22	0.19			

6.5.2 Disturbed Ionospheric Conditions

To assess the performance of the proposed CIT technique under more challenging conditions, GPS data during a period of enhanced ionospheric activity are processed and the CIT estimated profiles are validated. Initially, the disturbed day was chosen based on the Kp index. A Kp index higher than 4 indicates potentially disturbed local ionospheric conditions. After a thorough search in the Kp index of the years 2010 and 2011, it was found that 9 and 10 September, 2011 had a period with a Kp index that meets this criteria. Figure 6.12 shows the Kp index from 8 to 10 September, 2011. A Kp index of 7 was recorded after extremely quiet conditions. This is a strong indication that a geomagnetic storm was in progress. However, the Kp index is derived from globally distributed ground-based magnetometers. It reflects the conditions in a global sense and does not indicate where the activity is taking place. Therefore, another indicator (K-index) is required to confirm the disturbed conditions over a local region such as the Canadian polar region. The Canadian Geomagnetism Program computes the K-indices for three Canadian observatories: Ottawa (OTT), Meanook (MEA), and Victoria (VIC). Figure 6.13 shows the K-indices at these observatories for 09 and 10 September, 2011. It can be seen that K-indices of 4 or greater were recorded on 09 and 10 September, 2011. Specifically, the K-index at MEA ranges between 5 and 7 during the period of interest confirming that the ionosphere was disturbed during these days. As a result, the GPS data of 10 September are processed for the 24 hours of day as in the case of quiet days and the results are presented below.

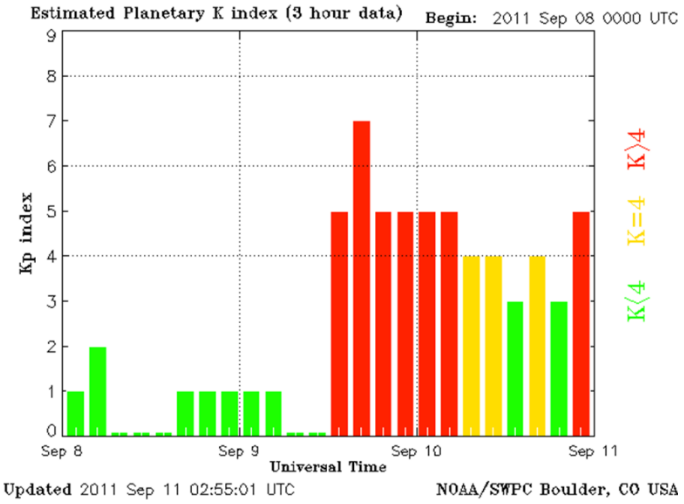

Figure 6.12: Planetary Kp indices for 10 September 2011 (<u>http://www.swpc.noaa.gov/ftpmenu/warehouse/2011/2011_plots.html</u>, April 2013)

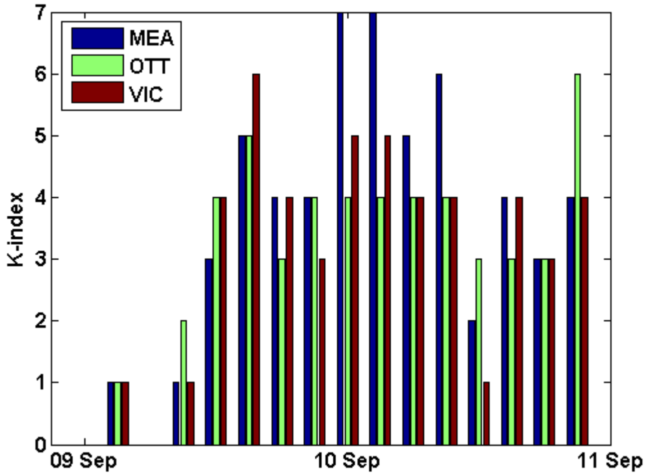

Figure 6.13: Local K-index for 9-10 September, 2011 (data courtesy of NRCAN)

Figure 6.15 shows the vertical TEC maps at selected hours of the day. The maps show the expected diurnal variation with no negative TEC values. The RMS of the residuals (Table 6.8) are noticeably high (~4 TECU) for UTC 00:30 and are generally higher than those computed for quiet days (Table 6.2). This can be explained by considering Figure 6.14 which shows the geomagnetic field observations at several Magnetic Observatories across Canada. The observations agree with the local K-index , where a variation along the North-South magnetic field component was persistent and lasted for the first ~10 hours for most of the stations especially those located between 49.5° N and 62.5° N and 246° E and 291.5° E. High fluctuations and sharp spikes in the geomagnetic field were detected especially in the first two hours of the day. During the same period, a local K-index value of 7 was recorded at MEA. This indicates a higher local level of geomagnetic activity occurred during these hours, which resulted in higher TEC residuals.

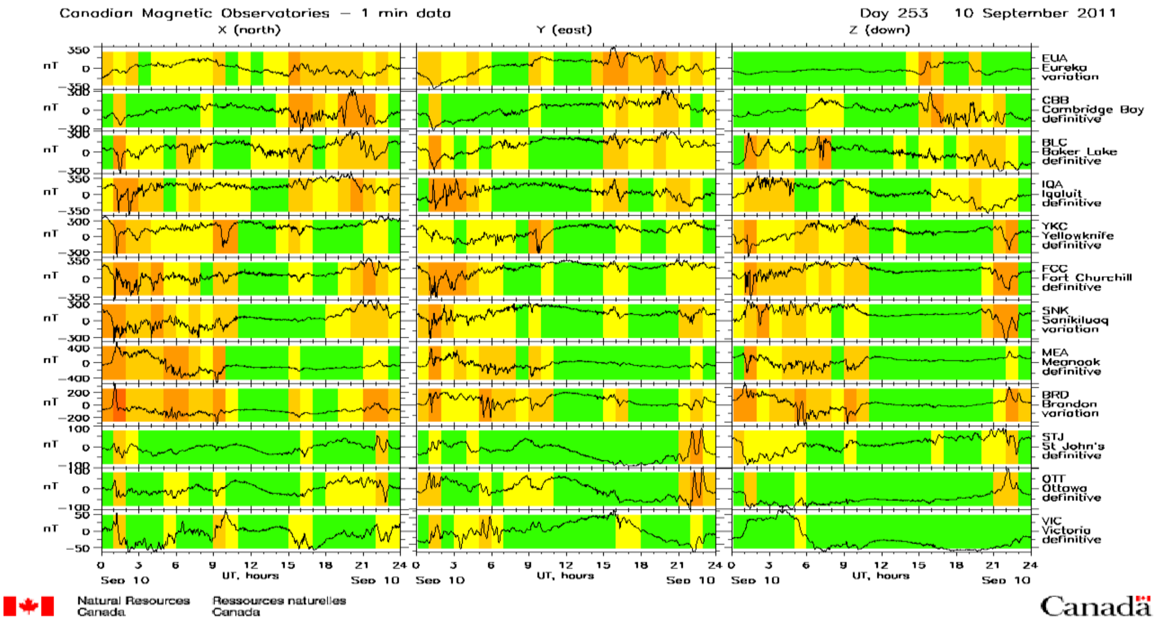

Figure 6.14: Geomagnetic field observations for Canadian magnetic observatories for 10 September, 2011 (http://www.geomag.nrcan.gc.ca; April 2013)

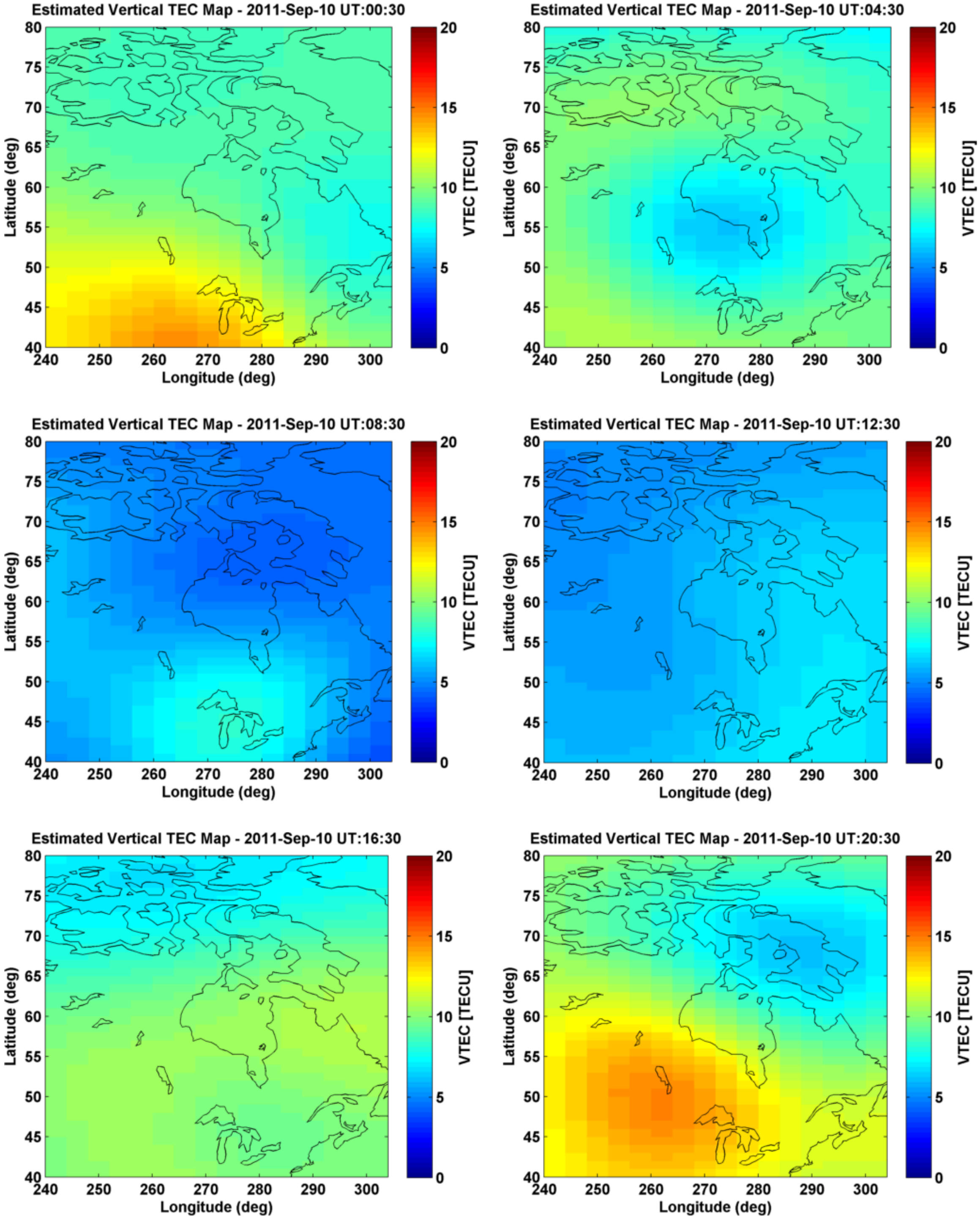
Estimated Vertical TEC Map - 2011-Sep-10 UT:00:30

Estimated Vertical TEC Map - 2011-Sep-10 UT:04:30

Estimated Vertical TEC Map - 2011-Sep-10 UT:08:30

Estimated Vertical TEC Map - 2011-Sep-10 UT:12:30

Estimated Vertical TEC Map - 2011-Sep-10 UT:16:30

Estimated Vertical TEC Map - 2011-Sep-10 UT:20:30

Figure 6.15: Estimated vertical TEC maps for 10 September 2011 (K_{max} =3 and Q = 3)

Table 6.8: Root mean square of the residuals in TECU (K_{max} =3 and Q = 3)

UTC	10 September 2010
00:30	4.03
04:30	2.31
08:30	2.19
12:30	1.94
16:30	2.02
20:30	2.76

Comparing the CIT electron density profiles to the RO-derived electron density profiles, the errors statistics of the full day of radio occultation events are found to be biased by 0.1 $\times 10^{11}$ el/m^3 with an overall root mean square of the errors of ~0.6×10^{11} el/m^3, which is slightly higher than that computed for the quiet days but within the range of the radio occultation accuracy. The estimated receiver IFB are listed in Table 6.9 and found to be stable with a standard deviation less than ~60 cm (3.8TECU). Comparison of the relative biases for JPL versus the proposed CIT technique (for the same sites analysed in Section 6.5) is presented in Figure 6.16 and results are consistent within 1.44 TECU (~23 cm). For completeness, the statistics of the difference between the electron density profiles derived by radio occultation versus CIT for all available occultation events are listed in Table 6.10.

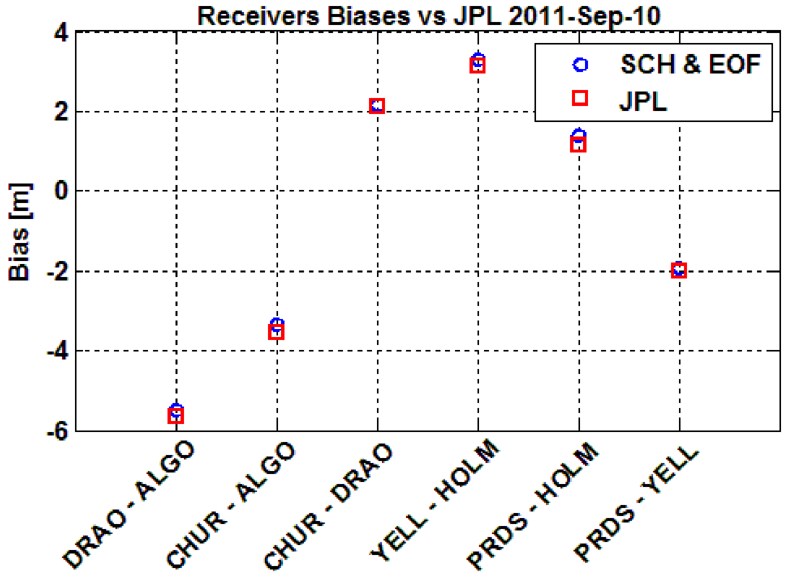

Figure 6.16: Comparison of JPL relative receiver inter-frequency biases for 10 September 2011 (K_{max} =3 and Q = 3)

Table 6.9: Estimated inter-frequency receiver biases for 10 September 2011 (K_{max} =3 and Q = 3)

Station	IFB [m]	Std [m]	Station	IFB [m]	Std [m]
ALGO	**-2.55**	**0.57**	**SASK**	**2.36**	**0.38**
BAKE	**-3.05**	**0.24**	**SCH2**	**-5.50**	**0.27**
BREW	**0.07**	**0.56**	**SHE2**	**1.09**	**0.44**
CHUR	**-5.84**	**0.31**	**UNBJ**	**0.68**	**0.39**
DRAO	**-8.05**	**0.55**	**VALD**	**-4.15**	**0.37**
ESCU	**1.61**	**0.39**	**WILL**	**-6.92**	**0.58**
FLIN	**-7.83**	**0.38**	**YELL**	**1.34**	**0.26**
HLFX	**-4.73**	**0.43**	**CBBC**	**4.89**	**0.33**
HOLM	**-1.85**	**0.30**	**EDMC**	**5.07**	**0.45**
KUUJ	**-3.03**	**0.31**	**EURC**	**5.34**	**0.51**
NAIN	**1.12**	**0.30**	**HALC**	**5.52**	**0.34**
NRC1	**6.53**	**0.48**	**IQAC**	**5.58**	**0.31**
PICL	**-5.59**	**0.34**	**PONC**	**5.20**	**0.38**
PRDS	**-0.63**	**0.46**	**RESC**	**4.84**	**0.44**
QIKI	**1.45**	**0.36**	**SANC**	**5.08**	**0.26**
RESO	**-0.84**	**0.36**	**TALC**	**4.89**	**0.31**

Table 6.10: Statistics of the difference between the electron density profiles derived by radio occultation vs. CIT for 10 September 2011 (K_{max} =3 and Q = 3)

UTC	RMSE (10^{11} el/m^3)	Mean (10^{11} el/m^3)	UTC	RMSE (10^{11} el/m^3)	Mean (10^{11} el/m^3)
01:37:38	0.15	-0.13	09:14:47	0.22	0.18
01:42:04	0.37	0.00	09:20:04	0.44	0.31
02:23:41	0.80	-0.33	09:23:31	0.65	0.22
02:23:53	0.30	-0.06	11:01:24	0.96	0.46
02:24:31	0.47	0.15	16:36:26	0.34	-0.03
04:12:00	0.86	0.41	18:14:55	0.50	-0.17
04:20:33	0.57	0.16	18:17:13	0.49	0.20
04:23:04	0.70	0.51	19:58:35	0.37	-0.34
05:03:37	0.64	0.55	20:02:45	0.71	0.39
05:10:36	0.57	-0.37	20:46:53	0.77	0.36
05:50:59	0.37	0.36	20:55:28	0.22	0.05
05:54:55	0.10	0.08	21:35:58	0.66	0.40
05:56:17	0.20	0.09	21:44:57	0.48	0.16
05:57:38	0.58	0.45	22:19:19	0.59	-0.39
05:57:44	0.59	0.39	22:20:48	0.37	-0.34
05:58:20	0.88	0.61	22:21:21	0.31	-0.29
05:59:25	0.77	0.56	22:24:03	0.55	-0.02
06:01:27	0.26	0.03	22:29:24	0.11	-0.05
07:30:10	0.02	-0.02	22:30:21	0.37	0.10
07:32:08	0.52	-0.13	22:31:29	0.57	0.28
07:44:07	0.59	-0.22	22:38:12	0.54	0.20
07:44:20	0.33	-0.26	22:40:01	0.69	0.02
07:45:45	0.51	-0.05	23:16:42	0.31	0.11

The CIT technique has been evaluated under quiet and disturbed conditions. To further demonstrate the importance and application of ionospheric tomography in understanding ionospheric phenomenon, six days (07-12 September, 2011) of GPS data are processed using the model settings listed in Table 6.1, where time series of the maximum electron density and TEC are computed using the reconstructed electron density, and an analysis of their behavior is conducted.

Variations in the maximum electron density and TEC over 47.5°N and 270° E for the period 07 – 12 September, 2011 are shown in Figure 6.17. The diurnal variation of the maximum electron density $\mathrm{N}_{\mathrm{e}_{\max}}$ and TEC is evident in the figure, where the lowest and highest values are expected during nighttime and 14:00 LT (20:00 UT along meridian 270° E), respectively. However, an unexpected sudden increase and gradual decrease in these values can be clearly seen on 9 September. Such behavior may indicate that ionospheric activity, such as ionospheric storm, is in progress.

Ionospheric storm resembles the magnetic storm. The storm effects are observed at high and middle latitude (Hargreaves, 1995). It is characterized by variations in $\mathrm{N}_{\mathrm{e}_{\max}}$ and TEC. There are three phases in the ionospheric storm: positive phase, main phase, and recovery phase. The positive phase, lasting a few hours, is characterized by an initial growth in the electron density and the total electron content. As the electron density distribution reaches values greater than normal, the main (negative) phase starts where a decrease in the electron density below normal values is evident. The electron density gradually returns to normal levels in the recovery phase, which might last for a period of one or more days.

Ionospheric storms occur in conjunction with geomagnetic storms. Therefore, a confirmation of the occurrence of a geomagnetic storm is necessary and the behavior of the maximum electron density is studied according to the definition of ionospheric storm where the positive and negative phases are identified. Different observations and indicators are used to confirm the signature associated with the geomagnetic storm. These include geomagnetic field observations, Disturbed Storm Time (Dst) index, Interplanetary Magnetic Field (IMF), and solar wind velocity.

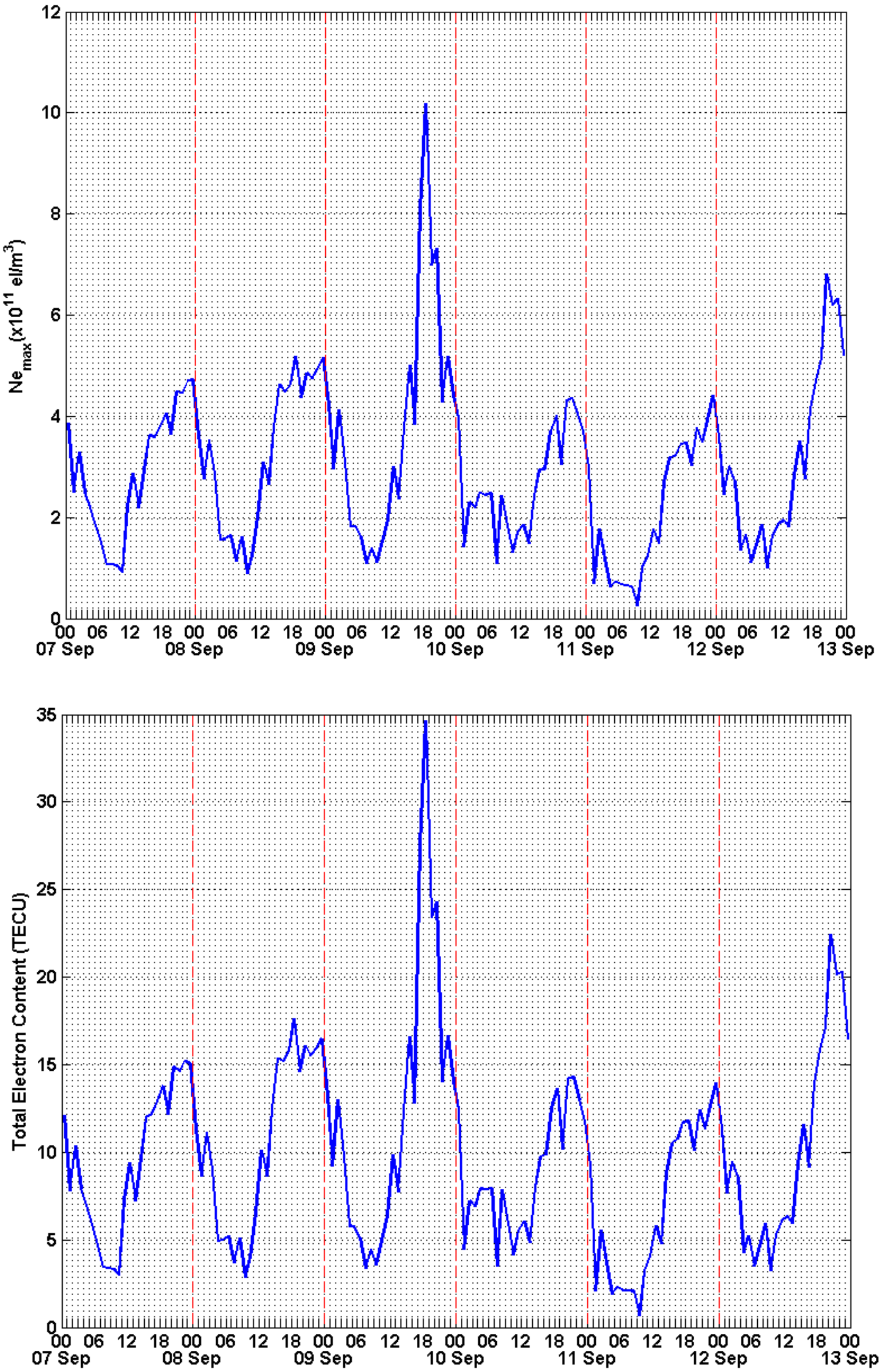

Figure 6.17: Vertical TEC (top) and Ne$_{max}$ (bottom) over 47.5°N and 270° E for September 2011

The Disturbed Storm Time (Dst) index is a measure of the magnetic storm level. It is computed from horizontal variations of the geomagnetic field measured at four low-latitude stations distributed globally in longitude (Koskinen, 2011). Negative Dst values between -50 nT and -100 nT indicate an intense magnetic storm. Figure 6.18 shows the Dst index for 9-10 September, 2011. The Dst index changed from 48 nT at 14:00 UT to -69 nT at 18:00 UT.

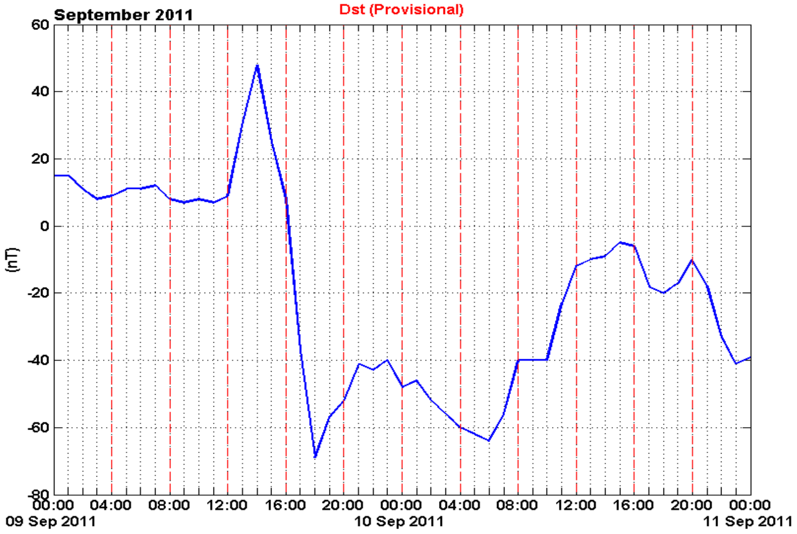

Figure 6.18: Dst index for 09-10 September, 2011 (data courtesy of World Data Center for Geomagnetism, Kyoto)

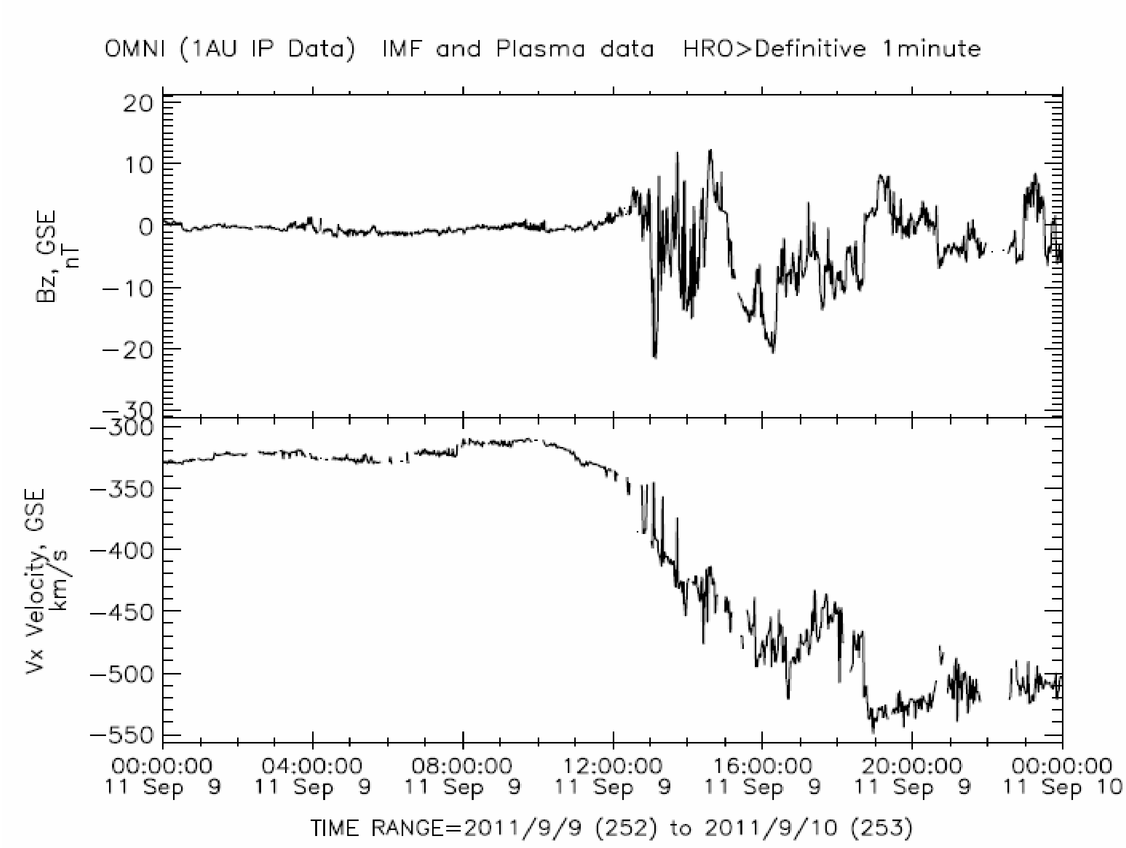

Figure 6.19: Interplanetary magnetic field (top) and the solar wind velocity, X component (bottom) for 09 September, 2011. (http://cdaweb.gsfc.nasa.gov; April 2013)

The solar wind speed and IMF data are useful to determine the occurrence of geomagnetic activity. Higher solar wind speed and southward IMF (more negative) indicates a potentially higher level of geomagnetic activity. The X component of the solar wind velocity and the IMF for 9 September 2011 are shown in Figure 6.19. Major changes in solar wind speed moving from 300 km/s to 550 km/s are observed at approximately 11:00 UT on September 9. This is accompanied by fluctuation of IMF starting at 12:00 UT on 9 September 2011 and lasting for more than one day. During that period, the IMF turned southward compared to the Earth's magnetic field and maintained this orientation between approximately 12:00 UT and 20:00 UT on 09 September 2011, which is in agreement with the recorded geomagnetic observations (larger fluctuations in local geomagnetic field) at several Canadian observatories (Figure 6.14).

All the above space weather parameters clearly confirm signatures of a geomagnetic storm on 9-10 September, 2011. Referring to Figure 6.17, the sudden increase of TEC and $\mathrm{N}_{\mathrm{e}_{\mathrm{max}}}$ values are consistent with the geomagnetic storm signatures. The positive and main storm phases can be identified in the figure. During the positive phase, the maximum electron density reached a value of ~ 10 $\times 10^{11}$el/m^3 on 09 September at 18:30 UT, which is twice the value of the previous days (~5. $\times 10^{11}$el/m^3). The main phase followed the positive values, where the maximum electron density values decrease gradually and return to normal levels after one day. The values of TEC behave similarly.

6.6 Chapter Summary

The CIT technique has been tested and validated under quiet and disturbed ionospheric conditions using GPS real data. An additional constraint is introduced as a suggested approach to overcome the effect of bad data geometry and undetected errors on the inversion problem. Results based on this method are presented. The estimated vertical TEC maps show the expected diurnal variation with realistic (no negative) TEC values. The relatively good comparison between the CIT-estimated electron density profiles and the RO derived profiles, combined with the relatively stable IFB and small differences between JPL and CIT-estimated relative IFB proves the validity of the technique and the correct implementation of the algorithm. A study of an ionospheric storm using CIT has been conducted. The phases of the ionospheric storm were identified based on the TEC and maximum electron density estimated using CIT. The study demonstrates that GPS tomography has become regarded as a useful tool in monitoring the ionosphere and providing a better understanding of the physical processes occurring in the Canadian polar region.

Chapter Seven: Conclusions and Recommendations

Ionospheric imaging over the Canadian polar region using GPS observations has been investigated in this thesis. The following sections summarize the conclusions and recommendations for future work.

7.1 Conclusions

A new three-dimensional Computerized Ionospheric Tomographic (CIT) technique using GPS measurements has been developed. The technique uses a combination of Spherical Cap Harmonics (SCH) and Empirical Orthogonal Functions (EOF) to describe the electron density distribution. The spherical cap harmonics describe the electron distribution horizontally and the empirical orthogonal functions describe and constrain the electron density distribution vertically. The vertical constraint is necessary in the case of using only ground-based GPS measurements so that a certain range of possible realistic solutions is allowed.

The algorithm has been implemented in a MATLAB software package. The software package takes in GPS data and applies the technique over a region bounded by latitude, longitude and altitude. Different settings can be set in the program. Some of these parameters are the cutoff angle, GPS data sampling interval, number of EOF (Q) and order of spherical cap harmonics (K_{max}), spherical cap half-angle (θ_o), and many others.

The feasibility of the new technique has been demonstrated using simulated data. The International Reference Ionosphere (IRI) model is used to simulate the electron density distribution in the ionosphere. Different ionospheric conditions have been simulated to assess the performance of the model in recovering different ionospheric parameters such as the electron density and Total Electron Content (TEC). These conditions are chosen so that the technique can represent nominal and storm conditions. The purpose of these simulation are: 1) determine the most appropriate combination of K_{max} and Q for the Canadian polar region to be adopted for processing GPS real data, and 2) demonstrate and assess the performance of the new technique. A network of existing GPS stations and simulated ionospheric conditions using IRI-2007 are used to determine the most appropriate combination of K_{max} and Q for the Canadian polar region which is found to be 3 and 3, respectively. The model is successful in retrieving the electron density profiles under nominal conditions. However, the technique cannot replicate and reconstruct electron density profiles that meet the targeted performance metrics under challenging conditions, such as the Storm Enhanced Density (SED). To overcome this limitation, a new approach has been proposed where the solution of the CIT technique is used to constrain the ionospheric tomography in its original form (voxel-based model). The high computational load and memory requirement associated with this approach is still a major concern and imposes a limitation in applying the method especially if a higher resolution, i.e. higher number of voxels, is required.

GPS real data has been used to further validate the CIT technique under quiet and disturbed conditions. However, in addition to the bad geometry associated with sparse GPS network stations, GPS-derived STEC measurements are susceptible to cycle slips and highly affected by noise. Since the design matrix associated with tomographic inversion is singular and severely ill-conditioned, the solutions estimated in such cases are not accurate and might be physically unrealistic. Therefore, an additional constraint has been proposed and introduced to enforce the technique to produce physically realistic solutions. In addition to this constraint, a reference (pseudo TEC measurement) has been introduced to estimate the receiver and satellite Inter-

Frequency Biases (IFB). The results are validated using: 1) Radio Occultation (RO) products; and 2) testing the stability of the IFB. Results shows expected diurnal variation of TEC values. The electron density profiles are relatively comparable to the RO derived profiles product within the reported accuracy of the product. The CIT-estimated IFB are found to be stable over the day and close to the values reported by Jet Propulsion Laboratory (JPL), indicating the validity and correct implementation of the technique. A study of an ionospheric storm has been conducted to demonstrate the importance of GPS tomography in identifying such events and providing a cost effective tool to remotely sense the Earth's ionosphere - which helps to better understand the physical processes in the ionosphere.

7.2 Recommendations

Ionospheric imaging using tomography is an ill-posed ill-conditioned inverse problem. This problem is mixed-determined: that is there are regions where the measurements over-determine some of the components in the solution, but under-determine other components. This is due to the sparsity and lack of data in certain regions. For example, there are no receivers in oceans and seas. This makes the ionosphere difficult to monitor by the data alone. Also, as explained in Chapter 4, the data geometry involved in ionospheric tomography using only ground-based GPS measurements is not ideal. Observations over all possible angles are not possible. There are insufficient measurements (line of sights) perpendicular to altitude; therefore the vertical resolution is not as good as the horizontal resolution. These issues impose certain limitations in the resolution and accuracy of the ionospheric tomography solution. A possible solution to these limitations is the use of some *a priori* information. The approach adopted in the thesis work utilizes empirical orthogonal functions to incorporate some a priori information on the vertical distribution of the electron density. However, combining different data sources that provide horizontal information can improve the vertical resolution. Satellite-based observations such as those from COSMIC provide additional observations which have good altitude information that help increase the coverage of the topside ionosphere data (that is so important for vertical resolution in the images). Thus, the limitations of sparsity of data and lack of vertical resolution in 3-D ionospheric tomographic imaging can be addressed through the ongoing development and availability of new and additional data sources. The new European satellite navigation system, Galileo, and the restored Russian system, GLONASS, are examples of other constellations that can double the quantity of TEC data, increasing the data coverage for such imaging.

The focus of the thesis is to develop an optimal tomographic model for the Canadian polar region to estimate ionospheric parameters that help in understanding the ionosphere better at such high latitudes. The technique shows promising results. Further investigations should be conducted for different wide area GPS networks at different latitudes with higher reference station density; investigations should include feasibility of the technique and the effect of different parameters on the model accuracy (such as cuttoff angle and site spacing). Studies should include K_{max} and Q as a function of network size, density of receivers, voxel size, polar cap parameters, and latitude and ionospheric activity.

Although the main product of the model is electron density, TEC maps can be computed and ionospheric corrections for navigation applications can be generated. The quality of the maps, hence the ionospheric corrections, are expected to be better than the conventional TEC maps generated from two-dimensional modelling. Further investigation of the quality of CIT derived ionospheric corrections for wide area GPS networks is recommended.

References

Afraimovich, E.L., Pirog, O.M. and Terekhov, A.I. (1992), “Diagnostics of large-scale structures of the high-latitude ionosphere based on tomographic treatment of navigation-satellite signals and of data from ionospheric stations”, *Journal of Atmospheric and Terrestrial Physics*, Vol. 54 No. 10, pp. 1265–1273.

AIAA. (1999), *AIAA Guide to Reference and Standard Ionosphere Models*, AIAA (American Institute of Aeronautics and Astronautics).

Araujo-Pradere, E.A., Fuller-Rowell, T.J., Codrescu, M.V. and Bilitza, D. (2005), “Characteristics of the ionospheric variability as a function of season, latitude, local time, and geomagnetic activity”, *Radio Science*, Vol. 40 No. 5, p. RS5009.

Arikan, O., Arikan, F. and Erol, C.B. (2007), “Computerized ionospheric tomography with the IRI model”, *Advances in Space Research*, Vol. 39 No. 5, pp. 859–866.

Aster, R.C., Borchers, B. and Thurber, C.H. (2012), *Parameter Estimation and Inverse Problems*, Academic Press.

Austen, J.R., Franke, S.J. and Liu, C.H. (1988), “Ionospheric imaging using computerized tomography”, *Radio Science*, Vol. 23 No. 3, pp. 299–307.

Austen, J.R., Franke, S.J., Liu, C.H. and Yeh, K.C. (1986), “Application of computerized tomography techniques to ionospheric research”, Presented at the International Beacon Satellite Symposium on Radio Beacon Contribution to the Study of Ionization and Dynamics of the Ionosphere and to Corrections to Geodesy and Technical Workshop, pp. 25–35.

Bhuyan, K., Singh, S.B. and Bhuyan, P.K. (2002), “Tomographic reconstruction of the ionosphere using generalized singular value decomposition”, *Current Science*, Vol. 83 No. 9, pp. 1117–1120.

Bhuyan, K., Singh, S.B. and Bhuyan, P.K. (2004), “Application of generalized singular value decomposition to ionospheric tomography”, *Ann. Geophys.*, Vol. 22 No. 10, pp. 3437–3444.

Bilitza, D. and Reinisch, B.W. (2008), “International Reference Ionosphere 2007: Improvements and new parameters”, *Advances in Space Research*, Vol. 42, pp. 599–609.

Bjõrck, A. (1996), *Numerical Methods for Least Squares Problems*, SIAM.

Brunini, C.A. (1998), *Global ionospheric model from GPS measurements* (Ph.D. thesis, Facultad de Ciencias Astronomicas y Geofisicas, La Plata, Argentina), Facultad de Ciencias Astronomicas y Geofisicas, La Plata, Argentina.

Bust, G.S., Garner, T.W. and Gaussiran II, T.L. (2004), “Ionospheric Data Assimilation Three-Dimensional (IDA3D): A global, multisensor, electron density specification algorithm”, *Journal of Geophysical Research*, Vol. 109 No. A11, p. A11312.

Bust, G.S. and Mitchell, C.N. (2008), “History, current state, and future directions of ionospheric imaging”, *Reviews of Geophysics*, Vol. 46 No. 1, p. RG1003.

Ciraolo, L., Azpilicueta, F., Brunini, C., Meza, A. and Radicella, S.M. (2007), “Calibration errors on experimental slant total electron content (TEC) determined with GPS”, *Journal of Geodesy*, Vol. 81, pp. 111–120.

Colombo, O.L., Hernandez-Pajares, M., Juan, J.M. and Sanz, J. (2000), “Ionospheric tomography helps resolve GPS ambiguities on the fly at distances of hundreds of kilometers during increased geomagnetic activity”, *Position Location and Navigation*

Symposium, IEEE 2000, Presented at the Position Location and Navigation Symposium, IEEE 2000, pp. 15–21.

"COSMIC Program Office Website". (2013), . Retrieved from http://cdaac-www.cosmic.ucar.edu/cdaac/products.html

Coster, A. and Skone, S. (2009), "Monitoring storm-enhanced density using IGS reference station data", *Journal of Geodesy*, Vol. 83 No. 3-4, pp. 345 – 351.

Coster, A.J., Colerico, M.J., Foster, J.C., Rideout, W. and Rich, F. (2007), "Longitude sector comparisons of storm enhanced density", *Geophysical Research Letters*, Vol. 34 No. 18, p. L18105.

Daniell, R.E., Brown, L.D., Anderson, D.N., Fox, M.W., Doherty, P.H., Decker, D.T., Sojka, J.J., et al. (1995), "Parameterized ionospheric model: A global ionospheric parameterization based on first principles models", *Radio Science*, Vol. 30 No. 5, pp. 1499–1510.

Erturk, O., Arikan, O. and Arikan, F. (2009), "Tomographic reconstruction of the ionospheric electron density as a function of space and time", *Advances in Space Research*, Vol. 43 No. 11, pp. 1702–1710.

ESA. (2013,April), "European Space Agency", ***http://www.egnos-pro.esa.int/index.html***.

FAA. (2013,April), "Federal Aviation Administration (FAA)", ***http://www.faa.gov***.

Foster, J.C. (1993), "Storm time plasma transport at middle and high latitudes", *Journal of Geophysical Research*, Vol. 98 No. A2, pp. 1675–1689.

Foster, J.C. (2000), "Quantitative Investigation of Ionospheric Density Gradients at Mid Latitudes", Presented at the Proceedings of the 2000 National Technical Meeting of The Institute of Navigation, Anaheim, CA, pp. 447–453.

Fremouw, E.J., Secan, J.A. and Howe, B.M. (1992), "Application of stochastic inverse theory to ionospheric tomography", *Radio Science*, Vol. 27 No. 5, pp. 721–732.

Gonzalez, W.D., Joselyn, J.A., Kamide, Y., Kroehl, H.W., Rostoker, G., Tsurutani, B.T. and Vasyliunas, V.M. (1994), "What is a geomagnetic storm?", *Journal of Geophysical Research: Space Physics*, Vol. 99 No. A4, pp. 5771–5792.

"GPS Official Website". (2013), . Retrieved from http://www.gps.gov/

Haines, G.V. (1985), "Spherical cap harmonic analysis of geomagnetic secular variation over Canada 1960–1983", *Journal of Geophysical Research: Solid Earth*, Vol. 90 No. B14, pp. 12563–12574.

Hargreaves, J.K. (1995), *The Solar-Terrestrial Environment: An Introduction to Geospace - the Science of the Terrestrial Upper Atmosphere, Ionosphere, and Magnetosphere*, Cambridge University Press.

Hernández-Pajares, M., Juan, J.M., Sanz, J. and Colombo, O.L. (2000), "Application of ionospheric tomography to real-time GPS carrier-phase ambiguities Resolution, at scales of 400-1000 km and with high geomagnetic activity", *Geophysical Research Letters*, Vol. 27, pp. 2009–2012.

Hofmann-Wellenhof, B., Lichtenegger, H. and Wasle, E. (2007), *GNSS - Global Navigation Satellite Systems: GPS, GLONASS, Galileo, and more*, Springer, 8thed.

Hofman-Wellenhof, B., Lichtenegger, H. and Collins, J. (2001), *Global Positioning System: Theory and Practice*, Springer Wien, 5thed.

"Interface Specification, IS-GPS-200F". (2011), . Retrieved from http://www.gps.gov/technical/icwg/ISGPS-200F.pdf

Jakowski, N., Tsybulyal, K., Radicella, S.M., Cueto, M. and Herraiz, M. (2005), "Comparison of Electron Density Profiles from CHAMP Data with NeQuick Model", in Reigber, P.D.D.C., Lühr, P.D.H., Schwintzer, D.P. and Wickert, D.J. (Eds.),*Earth Observation with CHAMP*, Springer Berlin Heidelberg, pp. 483–488.

Jayachandran, P.T., Langley, R.B., MacDougall, J.W., Mushini, S.C., Pokhotelov, D., Hamza, A.M., Mann, I.R., et al. (2009), "Canadian High Arctic Ionospheric Network (CHAIN)", *Radio Science*, Vol. 44 No. 1, p. RS0A03.

Kaplan, E.D. (2005), *Understanding GPS: Principles and Applications*, (Kaplan, E.D. and Hegarty, C.,Eds.), Artech House, 2nded.

Kelley, M.C. (2009), *The Earth's Ionosphere: Plasma Physics & Electrodynamics*, Academic Press.

Kleusberg, A. and Teunissen, P.J.G. (1998), *GPS for geodesy*, Springer.

Komjathy, A. (1997,September), *Global ionospheric total electron content mapping using the global positioning system*, Department of Geodesy and Geomatics Engineering, University of New Brunswick.

Koskinen, H. (2011), *Physics of Space Storms: From the Surface of the Sun to the Earth*, Springer.

Liu, J., Chen, R., Kuusniemi, H., Wang, Z., Zhang, H. and Yang, J. (2009), "Mapping the regional ionospheric TEC using a spherical cap harmonic model and IGS products in high latitudes and the arctic region", *Proceedings of IAIN 2009 World Congress*, Stockholm, Sweden.

Liu, Z. and Gao, Y. (2004), "Development and Evaluation of a New 3-D Ionospheric Modeling Method", *Navigation*, Vol. 51 No. 4, pp. 311–329.

Materassi, M. and Mitchell, C.N. (2005), “A simulation study into constructing of the sample space for ionospheric imaging”, *Journal of atmospheric and solar-terrestrial physics*, Vol. 67 No. 12, pp. 1085–1091.

Mead, J.L. (2007), “Parameter estimation: A new approach to weighting a priori information”, *J. Inv. Ill-Posed Problems*, Vol. 15, pp. 1–21.

Meggs, R.W. and Mitchell, C.N. (2006), “A study into the errors in vertical total electron content mapping using GPS data”, *Radio Science*, Vol. 41 No. 1, p. RS1008.

Meggs, R.W., Mitchell, C.N. and Spencer, P.S.J. (2004), “A comparison of techniques for mapping total electron content over Europe using GPS signals”, *Radio Science*, Vol. 39 No. 1, p. RS1S10.

Misra, P. and Enge, P. (2006), *Global positioning system: signals, measurements, and performance*, Ganga-Jamuna Press.

Mitchell, C.N. and Spencer, P.S.J. (2003), “A three-dimensional time-dependent algorithm for ionospheric imaging using GPS”, *Annals of Geophysics*. Retrieved from http://www.earth-prints.org/handle/2122/977

Parkinson, B.W. and Spilker, J.J. (Eds.). (1996), *Global Positioning System: Theory & Applications (Volume One)*, American Institute of Aeronautics and Astronautics, 1sted.

Pryse, S.E. and Kersley, L. (1992), “A preliminary experimental test of ionospheric tomography”, *Journal of Atmospheric and Terrestrial Physics*, Vol. 54 No. 7–8, pp. 1007–1012.

Rao, G.S. (2010), *Global Navigation Satellite Systems*, Tata McGraw-Hill Education.

Raymund, T.D., Pryse, S.E., Kersley, L. and Heaton, J. a. T. (1993), “Tomographic reconstruction of ionospheric electron density with European incoherent scatter radar verification”, *Radio Science*, Vol. 28 No. 5, pp. 811–817.

Rius, A., Ruffini, G. and Cucurull, L. (1997), “Improving the vertical resolution of ionospheric tomography with GPS Occultations”, *Geophysical Research Letters*, Vol. 24 No. 18, pp. 2291–2294.

Rogers, N.C., Mitchell, C.N., Heaton, J. a. T., Cannon, P.S. and Kersley, L. (2001), “Application of radio tomographic imaging to HF oblique incidence ray tracing”, *Radio Science*, Vol. 36 No. 6, pp. 1591–1598.

De Santis, A. (1991), “Translated origin spherical cap harmonic analysis”, *Geophysical Journal International*, Vol. 106 No. 1, pp. 253–263.

Sardón, E. and Zarraoa, N. (1997), “Estimation of total electron content using GPS data: How stable are the differential satellite and receiver instrumental biases?”, *Radio Science*, Vol. 32 No. 5, pp. 1899–1910.

Schaer, S. (1999), *Mapping and predicting the earth’s ionosphere using the global positioning system*, University of Bern, Bern, Switzerland.

Schmidt, M. (2007), “Wavelet modelling in support of IRI”, *Advances in Space Research*, Vol. 39 No. 5, pp. 932–940.

Seeber, G.N. (2003), *Satellite Geodesy: Foundations, Methods, and Applications*, Walter de Gruyter.

Sharma, S., Dashora, N., Galav, P. and Pandey, R. (2011), “Cycle slip detection, correction and phase leveling of RINEX formatted GPS observables”, *Current Science*, Vol. 100 No. 2, pp. 205–212.

Skone, S. and Coster, A. (2009), “Studies of storm-enhanced density impact on DGPS using IGS reference station data”, *Journal of Geodesy,* Vol. 83 No. 3-4, pp. 235–240.

Skone, S., Hoyle, V., Lee, S. and Poon, S. (2002), “Variations in Point Positioning Accuracies for Single Frequency GPS Users during Solar Maximum”, *Geomatica,* Vol. 56 No. 2, pp. 131–140.

“The United States Naval Observatory”. (2013), . Retrieved from http://www.usno.navy.mil/USNO/time/gps/current-gps-constellation

Wen, D. and Liu, S. (2010), “A new ionospheric tomographic algorithm — constrained multiplicative algebraic reconstruction technique (CMART)”, *Journal of Earth System Science,* Vol. 119 No. 4, pp. 489–496.

Yue, X., Schreiner, W.S., Kuo, Y.-H., Wu, Q., Deng, Y. and Wang, W. (2013), “GNSS radio occultation (RO) derived electron density quality in high latitude and polar region: NCAR-TIEGCM simulation and real data evaluation”, *Journal of Atmospheric and Solar-Terrestrial Physics*.